Title
On Compton Imaging

Author
Mattafirri, Sara

Publication Date
2010

On Compton Imaging

by

Sara Mattafirri

A dissertation submitted in partial satisfaction of the

requirements for the degree of

Doctor of Philosophy

In

Engineering-Nuclear Engineering

in the

Graduate Division

of the

University of California, Berkeley

Committee in charge:

Professor Stanley G. Prussin, Co-Chair
Professor Kai Vetter, Co-Chair
Professor Jasmina Vujic
Professor Steven Conolly

Fall 2010

Abstract

On Compton Imaging

by

Sara Mattafirri

Doctor of Philosophy in Engineering-Nuclear Engineering

University of California, Berkeley

Professor Stanley G. Prussin, Co-Chair
Professor Kai Vetter, Co-Chair
Professor Jasmina Vujic
Professor Steven Conolly

The feasibility of producing an image of radioactivity distribution within a patient or confined region of space using information carried by the gamma-rays emitted from the source is investigated. The imaging approach makes use of parameters related to the gamma-rays which undergo Compton scattering within a detection system, it does not involve the use of pin-holes, and it employs gamma-rays of energy ranging from a few hundreds of keVs to MeVs. Energy range of the photons and absence of pin-holes aim to provide larger pool of radioisotopes and larger efficiency than other emission imaging modalities, such as single photon emission computed tomography and positron emission tomography, making it possible to investigate larger pool of functions and smaller radioactivity doses.

The observables available to produce the image are the gamma-ray position of interaction and energy deposition during Compton scattering within the detection systems. Image reconstruction methodologies such as backprojection and list-mode maximum likelihood expectation maximization algorithm are characterized and applied to produce images of simulated and experimental sources on the basis of the observed parameters.

Given the observables and image reconstruction methodologies, imaging systems based on minimizing the variation of the impulse response with position within the field of view are developed. The approach allows imaging of three-dimensional sources when an imaging system which provides full 4π view of the object is used and imaging of two-dimensional sources when a single block-type detector which provides one view of the object is used.

Geometrical resolution of few millimeters is obtained at few centimeters from the detection system if employing gamma-rays of energy in the order of few hundreds of keVs and current state of the art semi-conductor detectors; At this level of resolution, detection efficiency is in the order of 10^{-3} at few centimeters from the detector when a single block detector few centimeters in size is used. The resolution significantly improves with increasing energy of the photons and it degrades roughly linearly with increasing distance from the detector; Larger detection efficiency can be obtained at the expenses of resolution or via targeted configurations of the detector. Results pave the way for image reconstruction of practical gamma-ray emitting sources.

TABLE OF CONTENT

INTRODUCTION

Imaging gamma-rays is an objective in many applications involving radioactive elements, such as biomedical imaging, astrophysics, nuclear non-proliferation, and nuclear material monitoring. The predominance of the Compton scattering for photons of energy ranging from a few hundred keV up to a few MeV makes this process preferable for many imaging applications. Many elements in the periodic table have a gamma-ray emitting isotope in this energy range, and can be used for image formation, although, depending on the application, only isotopes which have half lives greater or smaller than a certain value can practically be imaged. A characteristic of Compton imaging is the capability of discerning the energy of the photon allowing for imaging of more than one isotope at the same time.

When interested in mapping the distribution of a radioisotope in space, the number of gamma-rays emitted per unit volume is proportional to the concentration of the radioisotope. In biomedical emission imaging the distribution of a particular radioisotope is indicative of particular pathologies and biological functions and is used to infer information concerning the status of the pathology or biological function itself. When compared to single photon emission computed tomography and other collimator-based imaging technologies, Compton imaging offers an intrinsic sensitivity advantage, in terms of the fraction of photons that can be recorded by the detection system per unit time, thus it has the potential to decrease the patient dose. Moreover Compton imaging, allowing imaging of gamma-rays within a relatively large energy range, makes it possible to use a larger pool of radiotracers, paving the way for innovative biomedical investigations.

The aim of this study is to explore and characterize image reconstruction of distributed sources. The precision and accuracy, quality obtained in the image is a result of the precision and accuracy of the observed parameters and of fundamental criteria adopted for the imaging system and imaging methodology. Current instruments employable to detect gamma-rays provide relatively accurate and precise measurements that can be used to determine the locus of emission of the gamma-rays in simple backprojection. A brief description of the imaging detector, observables, and the image formation concept are described in Chapter 1. Chapter 2 treats the methodology adopted to evaluate the errors affecting the observables and their effect on image resolution. Approaches to image reconstruction via backprojection and a list-mode maximum expectation algorithm is presented and discussed in Chapter 3. Images of simulated point-like sources and of distributed experimental and simulated sources are presented and discussed in Chapter 4.

ACKNOWLEDGEMENTS

To all human beings, including each-self; I thank any person's presence, physical and emotional, during the time I have been a Ph.D. student at the University of California in Berkeley.
I thank the University for making it possible to travel, meeting and sharing with groupages of realities, which develop the thinking human, vision and pragmatism, and make a person call any place home and retain his own personality, identity, and preferences.

CHAPTER I

IMAGING SYSTEM

1.1 INTRODUCTION

Instruments that allow emission imaging through the Compton process are generally referred to as Compton cameras [1], [2]. These instruments can measure the position of interaction of the gamma-ray with an orbital electron in the detector and the kinetic energy transferred to it. The energy transferred by the gamma-ray during scattering is processed to obtain the scattering angle. The direction between the first and a following electron-photon interaction of the scattered gamma-ray identifies the reference direction for the scattering angle. The scattering angle and reference direction allow the establishment of a region of space from which the incident gamma-ray could have been emitted from without the use of mechanical pin-holes.

1.2 CONCEPT OF THE DETECTION SYSTEM

A schematic representation of the detection system is shown in Figure 1. The radioactive object is placed next to the detection element with no mechanical collimator. The object emits gamma-rays at energy E_0, with spatial distribution $f(\boldsymbol{r})$ assumed proportional to the radioactive atom distribution $N(\boldsymbol{r})$ for each radioisotope species emitting photons at E_0. The detection elements consist of practical block-type devices capable of measuring the position of interaction and energy deposition of each gamma-ray interacting in the system.

The Compton scattering angle, θ, of the incident gamma-ray is determined, under the assumption that the orbital electron is free and at rest before the impact, according to the Compton formula:

$$\cos(\theta) = 1 - \frac{m_e c^2 T_e'}{E_0 (E_0 - T_e')} \tag{1.1}$$

where, E_0 is the energy of the incident gamma-ray, T_e' is the kinetic energy transferred to the orbital electron, and m_ec^2 is the rest mass energy of the electron. E_0 is assumed to be known and proper of the radioisotope used for image formation; T_e' is measured.

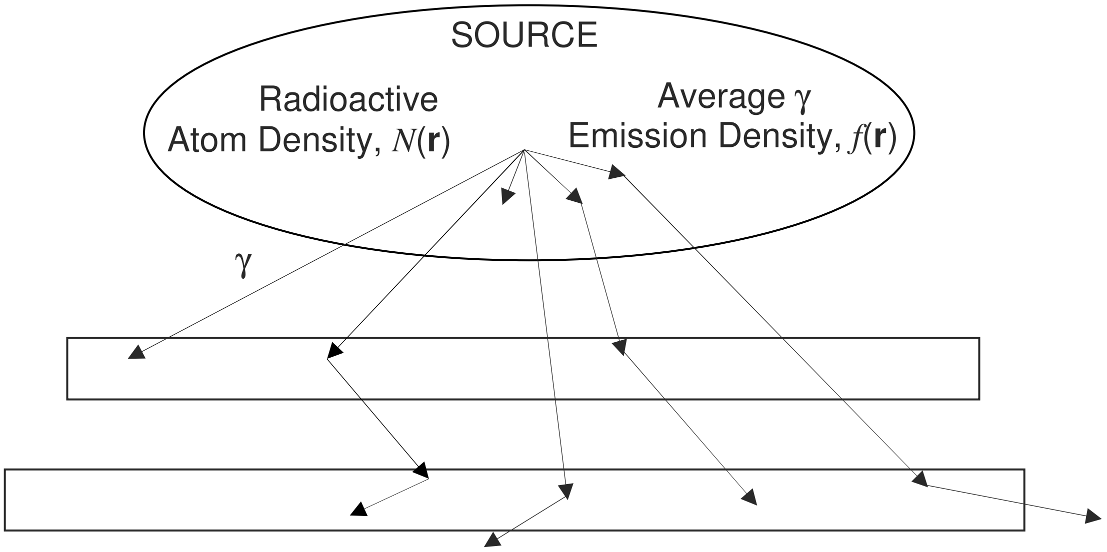

Fig. 1. Schematic concept of Compton imaging system. The gamma-ray emitting source and two block-type detection elements are shown.

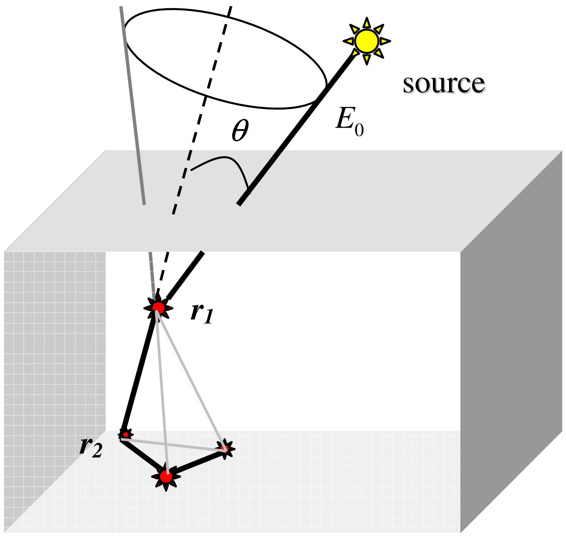

Fig. 2. Schematic representation of a gamma-ray interaction sequence in a detection system and determination of gamma-ray emission region.

Under the assumption that the detection system is not capable of measuring the direction of the electron after the impact, the direction of the gamma-ray before the impact is not uniquely identified, but it could lay anywhere along any generatrix of a cone of aperture θ. The axis of the cone is determined by the first and second position of interaction of the gamma-ray within the detector. Each cone describes the region of space from which the gamma-ray could have been emitted. Each gamma-ray interaction sequence is referred to as an event for the reminder of this chapter.

1.3 DETECTION SYSTEM LAYOUT AND IMAGING CASE

Criteria used to choose a particular detection system configuration are generally based on: the scope of the investigation, in biomedical imaging this might imply usage of a particular gamma-ray emitting radioisotope, and thus the gamma-ray energy; dose limits to the patient; image resolution; the image reconstruction methodology, imaging problem and characteristics of the reconstruction algorithm.

The scope of the analysis to be presented here is not to design the optimum detection system pertaining a particular imaging case, but rather to study the feasibility of using the block-type detection elements described in paragraph 1.4 to obtain an image of radioactivity distribution in an object of the size comparable to a laboratory rat or human breast. It is assumed that the goal is to detect here radioactivity concentrated in a location that corresponds to a tumor, for example, with respect to background radioactivity. Other imaging cases might require identification of confined and pre-defined radioactive shapes in the absence of background noise radioactivity. This is for example the case of mapping the dose distribution delivered by heavy-ion or proton beams in cancer therapy [3], [4]. In this case, prompt gammas are emitted with energy of few MeV at the location of the proton interaction. Three-dimensional imaging is included as a goal of this analysis. Three dimensional imaging of the object is in principle possible in Compton imaging using block type detectors employing only one view of the object. This is possible because of the information carried by the observed gamma-ray interaction sequences in the detector.

A variety of radioactive isotopes can be used in Compton imaging with emission photon energy ranging from hundreds of keV to several MeV, thus the suitable radiotracer can be chosen depending on the particular biomedical function to be investigated. The block-type detection element described in paragraph 1.4 was conceived for gamma-rays of energy below 1 MeV. However imaging of more energetic photons is still possible even with this system. As discussed in chapter 2. The energy of the gamma-ray affects image resolution, with resolution improving at increasing energy. Estimates of image resolution are given in chapter 3 as a function of photon energy. Energy of the gamma-ray also affects detection efficiency [5]. Estimates of detection efficiency are given at 392 keV because this is the energy of the photons used to gather experimental data discussed in Chapter 4.

Generally, for image formation, it is preferred to employ gamma-rays that deposit full energy in the detection system. These gamma-rays do not undergo scattering outside of the detection system and can be selected in order to prevent artifacts in the image due to erroneous event or cone reconstruction. Also, by selecting full-energy deposition events, imaging more than one radioisotope at the same time is possible. Full-energy deposition within the detection system might thus be desirable, and methods to increase probability that the gamma-ray deposits full energy in the detectors are usually used in Compton cameras. Full-energy deposition is generally achieved by making the detection elements as thick as possible and larger atomic number materials are also preferred. These two features also increase the scattering probability, thus detection efficiency. Semiconductor materials are used in the active volume of the detector to generate the electrical signal and detect the gamma-ray interaction. Manufacturing techniques and breakdown voltage associated to these materials pose an upper limit for the thickness [6]. Because only multiple interaction sequences can be used for image formation, using one thick block is not preferred. Hence there would be successive interactions separated by relatively small distances and the error on the cone axis direction would increase, as discussed in Chapter 2. Thus, two detectors are generally used, the first of which is employed as a scatter, the second as an absorber. This allows creating multiple interaction sequences with sufficient distance between the first and second interaction to obtain relatively small errors on cone axis direction. The thicker the absorber, the larger is the fraction of detected photons. Also, to increase efficiency the absorber is made out of germanium, Z=32, and the scatterer detector is made out of silicon, Z=14. Silicon being a lighter material lowers the probability of having absorption versus scattering and more than one interaction in the first detector. Silicon also offers the advantage of reducing the error on cone aperture because of smaller orbital electron binding energy, as discussed in Chapter 2. Decreasing distance between first and second detector increases efficiency, however the error on cone axis increases. As shown in Chapter 2, the error on the cone axis is the dominant factor that limits image resolution at gamma-ray energies above few hundreds of keVs. Efficiency is nevertheless important, particularly when the system is used to obtain an image in a human-being because it determines the dose to the patient and minimizing the dose to the patient is highly desirable. Thus the distance between first and second detector should be chosen on the basis of dose limits to the patient and image resolution.

1.4 DETECTOR AND OBSERVABLES

The detection system used to acquire measurements for this analysis employs one high-purity germanium and one silicon lithium drift detector, both of them have block type geometry. The lighter atomic number silicon detector is used as the scatterer detector and the higher atomic number germanium detector is used as the absorber. The system requires liquid nitrogen cooling in order to minimize noise on the electrical signals due to charge carriers generated by thermal and spurious processes [6]. A picture of the germanium detector is shown in Figure 3.

When the gamma-ray collides with an orbital electron, it transfers energy to it, if the energy transfer is higher than the binding energy the bound electron reaches a free potential energy state and the electron kinetic energy is deposited along its path in the creation of electron-hole pairs [6]. The electron-hole pairs are charge carriers in their migration to the detector collecting cathode and anode and create a voltage signal that is proportional to the electron kinetic energy [6], [7]. At typical gamma-ray energies below 1 MeV, the recoil electron track in the semiconductor is on the order of the mm, thus in principle it is possible to obtain relatively accurate position of gamma-ray interaction through the use of cathodes and anodes having the shape of fine strips on each side of the detector. The strips on the two sides are orthogonal to each other, as shown in Figure 4.

The pitch size of the grid is 2 mm, and each strip is 1.5 mm wide. The third dimension is obtained by measuring the difference in charge carrier's collection time assuming a certain carrier's drift velocity [6], [7]. The energy deposited by the gamma-ray is obtained from the amplitude of the voltage signal. By analyzing the shape of the induced voltage signals in the electrodes adjacent to the collecting electrodes it is possible to improve the accuracy and precision on position of interaction, thus to achieve better resolution than that given by the geometry of the electrode grid [7]. Position and energy resolution for the current generation high purity Ge and Si(Li) detectors could be as low as: 0.5mm at 122 keV and 1.6 keV at 60 keV [9].

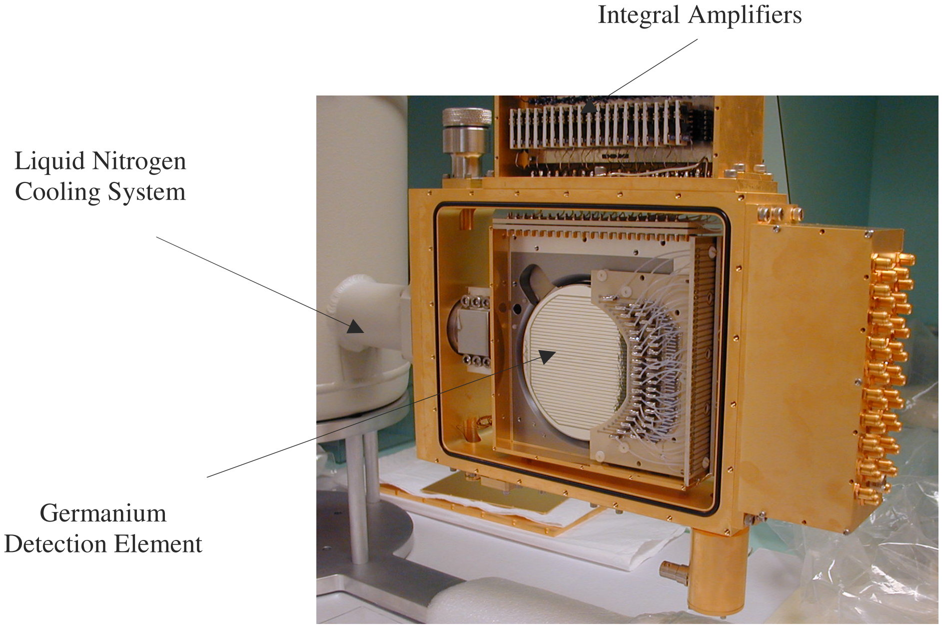

Fig. 3. Detection module. The detection element, liquid nitrogen cooling system, and integral amplifiers are shown.

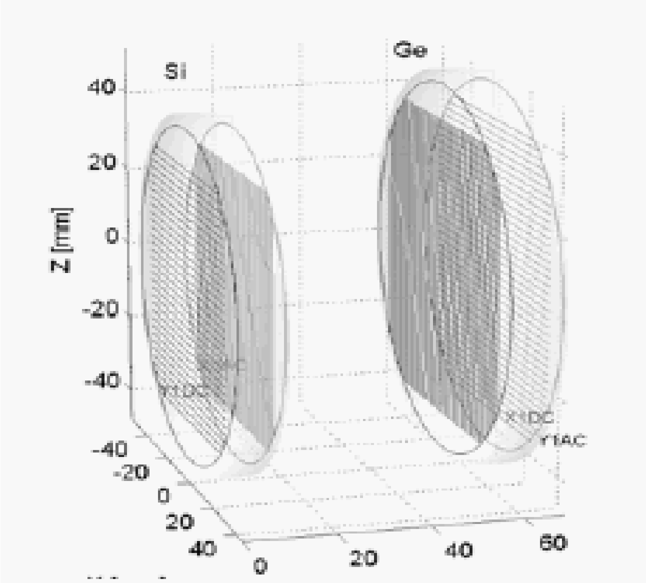

Fig. 4. Schematic representation of Germanium and Silicon detection modules. The electrodes have the shape of strips aligned along orthogonal directions on one side with respect to the other side.

Count rates are generally limited by the charge carriers drift velocities and depend on the location of the interaction along the detector depth, thus on gamma-ray energy. Typical count rates for detection elements on the order of one centimeter in thickness and a gamma-ray energy on the order of several hundreds of keV, are on the order of few kHz [8]. The time resolution in these instruments is about 5 nanoseconds [8]. Given the speed of the photon, the dimensions and configuration of the detection system, it is not at present possible to identify the chronology of interactions produced by the same incident gamma-ray. The interaction chronology needs thus to be inferred on the basis of Compton kinematics: all possible permutations of position of interactions are taken into consideration; the deviation between the scattering angle given by the geometry of the permutation and the Compton formula is computed; the permutation that minimizes the deviation is selected. Some two interaction sequences are ambiguous [10], and the chronology can not be determined; these interactions are discarded. The process of identifying the interaction sequences is generally referred to as gamma-ray tracking and the methodology is documented in [5] and [7]. Once the chronology is established, the scattering angle and the direction between first and second interaction are obtained. As discussed in chapter 3, this information allows imaging by backprojection and other modalities.

1.5 DETECTION EFFICIENCY

Detection efficiency is defined for this study as the fraction of photons observed by the detection system and used to form the image out of the total number of photons emitted by the source. As discussed in chapter 3, the events that are used to form the image are multiple collision sequences originated by a primary photon, because they allow image reconstruction via backprojection. Full-energy deposition of the primary photon in the detection system might be included as the additional selection criteria when it is proven that using gamma-rays that scattered outside the detection system results in significant artifacts in the image. Gamma-ray sequences of which the first impact occurs in the first detector and the second impact occurs in the second detector, might be selected; as shown in chapter two, this should result in an improved image resolution. Selection of full-energy deposition sequences and sequences that have the first and second interaction in different detection blocks comes at the expenses of detection efficiency, thus at the expenses of dose to the patient. Image quality should therefore be evaluated for specific imaging case with the scope of assessing if full energy deposition and sequences of which the first impact occurs in the first detector and the second impact occurs in the second detector should be selected.

Detection efficiency has been estimated via Monte Carlo simulations using the transport code Geant4 [11], [12], for the block type detectors described in paragraph 1.3. A point-like source, emitting gamma-rays at 392 keV, has been placed at several locations within the field of view. The field of view extends for about a 100 mm axial distance from detector and a 100 mm radial distance from detector. Photons have been generated isotropically in 4π about the source and transported in the surrounding air volume and detector. For each gamma-ray that is generated, the scattering location in the detector, the energy deposition and the chronology of the interactions is identified and stored for any type of interaction sequence: one interaction, multiple interactions, full-energy deposition and non-full energy deposition sequences. Estimates of detection efficiency given herein are representative of an ideal data acquisition system with an infinitesimally small dead time, or a photon flux that is low enough to allow no pile up of the electrical signals in the data acquisition system. Estimates of detection efficiency obtained via numerical simulation are assumed to be representative of an ideal detection system where the time, space and energy resolving capability are assumed to be perfect; in this case the process of identifying gamma-ray sequences from detector measurements has unitary efficiency. In practical instruments the measured signals are associated to gamma-ray interaction sequences with a certain level of confidence and some measurements need to be discarded; at present this process efficiency has been estimated in [13], [7], [10]. Estimates of detection efficiency presented herein are considered to be an upper limit of the practical system.

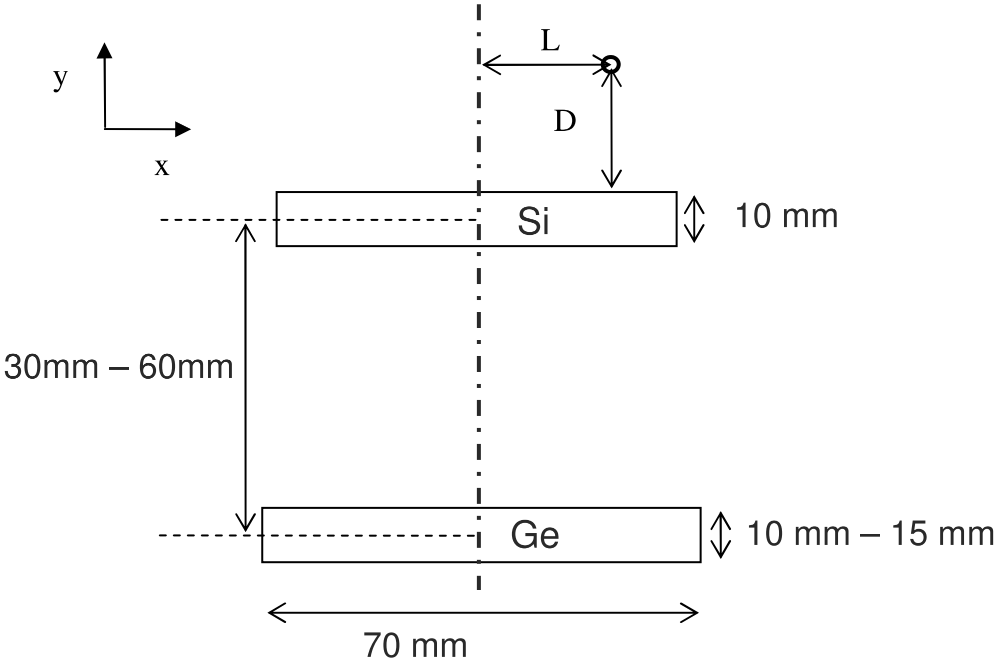

Fig. 5. Model adopted to estimate detection efficiency. A point like source emitting photons at 392 keV is used. The first detector has fixed thickness of 10 mm. The second detector has variable thickness (10 mm and 15 mm). The distance between the two detectors has been set to 60 mm and 30 mm.

For the detection system shown in Figure 5, and a 392 keV photon source at several locations in the field of view, about sixty to seventy percent of all sequences involve one interaction, and about ten percent of all sequences end in a photoelectric absorption. As mentioned and discussed in details in chapter 3, one interaction sequences are not used for image formation within this study. Out of the multiple interaction sequences, between thirty to forty percent end in a photoelectric absorption, and a little more than ten percent have first and second interactions in different detectors. The majority of the sequences have the first and second interaction occurring in the same detector. Although it penalizes efficiency, these sequences are generally not used for image formation, in an effort of obtaining image resolution as high as reasonably achievable.

Detection efficiency is shown in Figure 6 to Figure 8 for: all sequences made of multiple collisions; sequences made of multiple collisions of which the first collision occurs in the first detector and the second occurs in the second detector; sequences made of multiple collisions of which the first collision occurs in the first detector and the second occurs in the second detector, of which the last collision generates a photoelectric absorption.

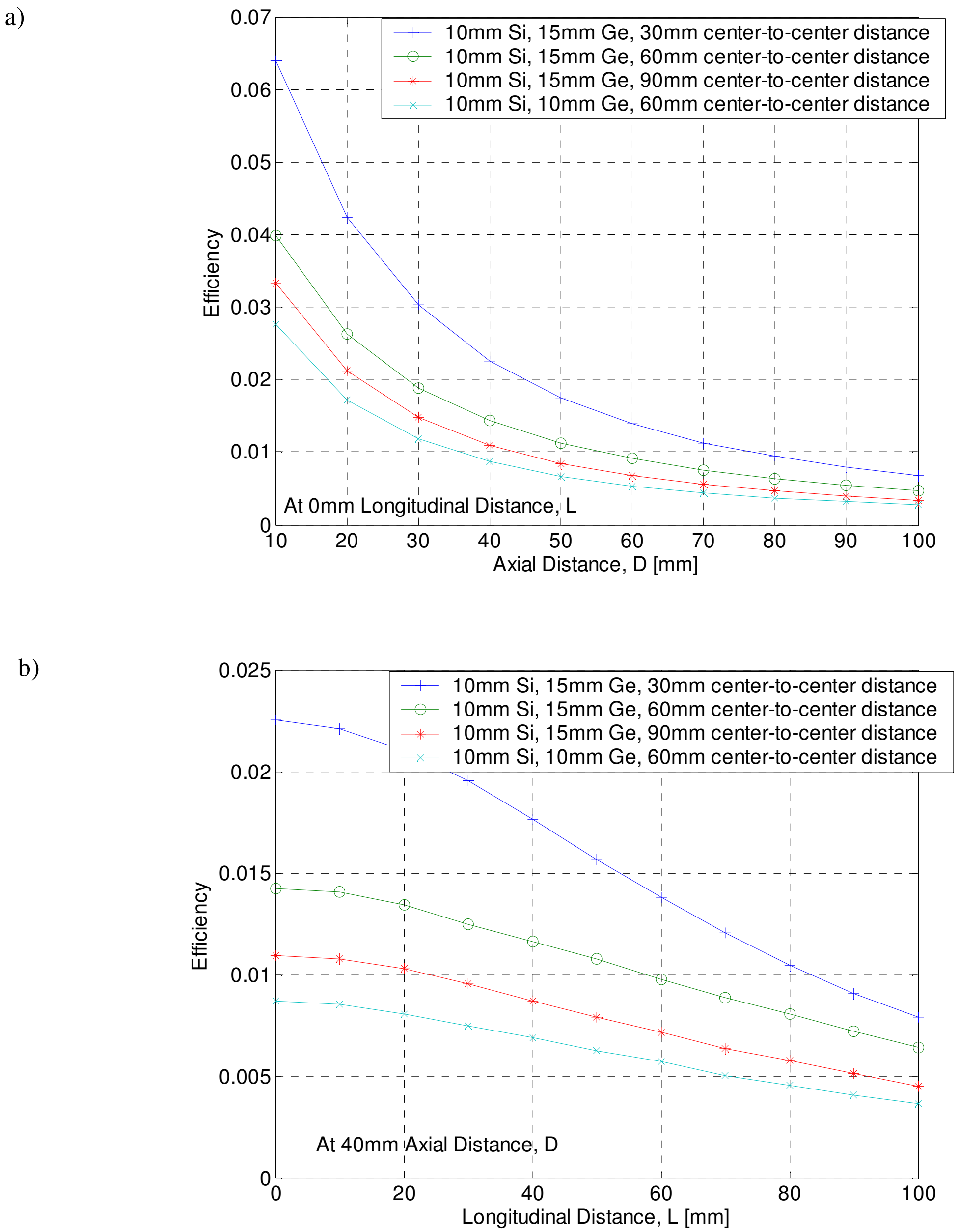

Fig. 6. Detection efficiency estimated via numerical simulation for gamma-rays at 392 keV. All Gamma-ray interaction sequences made of multiple collisions in the detection system are used to compute the efficiency. a) Axial profile; b) Longitudinal profile.

As shown, if all multiple interaction sequences are used for image formation, a detection efficiency on the order of a percent can be obtained up to distances of 60 mm to 80 mm from the detector. Requiring that the two interactions occur in separate detectors lowers the efficiency of by almost one order of magnitude; the additional requirement of full energy deposition determines a further decrease of detection efficiency by about a factor of two. As shown, detection efficiency can be improved by about a factor of two if the distance between first and second detector is decreased from 60 mm

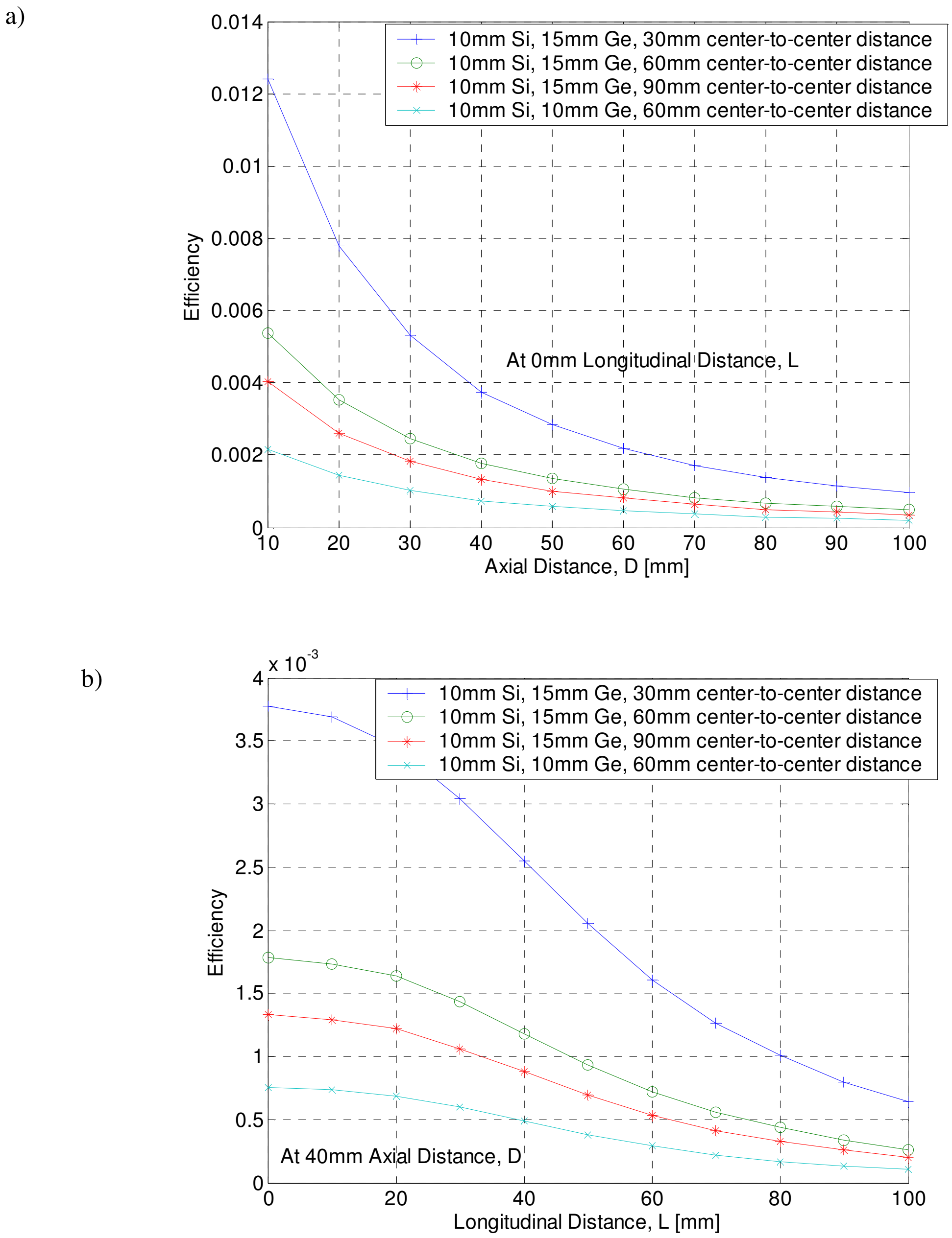

Fig. 7. Detection efficiency estimated via numerical simulation for gamma-rays at 392 keV. Gamma-ray sequences used to compute the efficiency are made of multiple collisions of which the first collision occurs in the first detector and the second collision occurs in the second detector. a) Axial profile; b) Longitudinal profile.

to 30 mm; some improvement is also obtained by increasing the thickness of the second detector. Detection efficiency variation across the direction parallel to the detector face is on the order of 20% to 30% for the fraction of field of view that lies below the detection element; moving outside of the detection element causes the detection efficiency to decrease more rapidly. Larger variations are experienced in the direction perpendicular to the detector face. The variation along this direction is in first approximation, and exact if the second detector had infinite surface area with respect to the first, due to the variation with distance of the solid angle subtended by the first

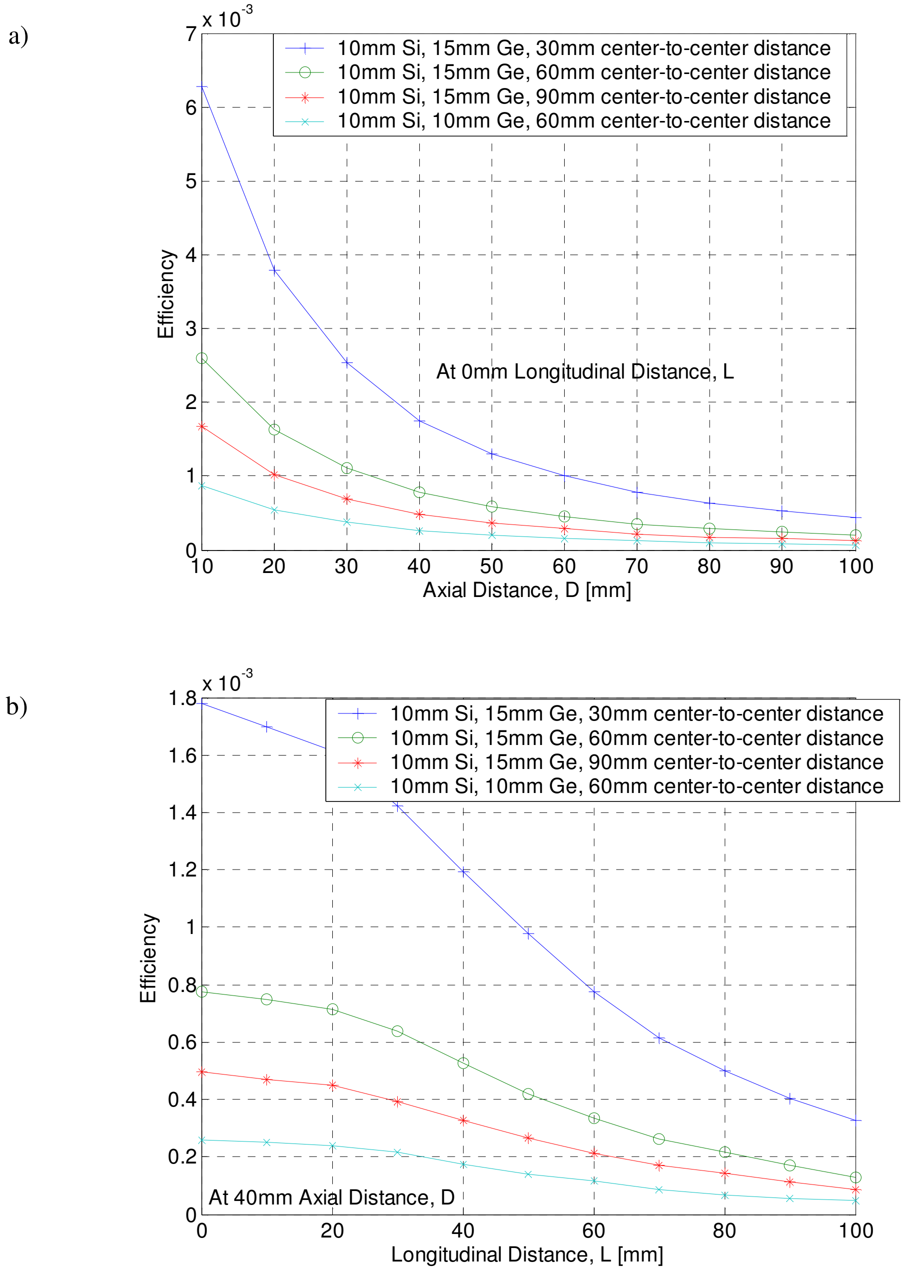

Fig. 8. Detection efficiency estimated via numerical simulation for gamma-rays at 392 keV. Gamma-ray interaction sequences made of multiple collisions of which the first collision occurs in the first detector and the second collision occurs in the second detector, and of which the last collision is a photoelectric absorption are used to compute the efficiency. a) Axial profile; b) Longitudinal profile.

detector to a location in field of view. The dependence of the solid angle on axial distance in far field approximation is proportional to the inverse of the square of the distance, while a more complex relationship exists for near field approximation; the dependence of the solid angle on longitudinal distance follows a cosine law [14], [15], [16], [17]. Correction of these variations, using analytical or numerical estimates, is employed when performing image reconstruction.

Bibliography

[1] V. Schonfelder, A Hirner, and K. Schneider, *A Telescope for soft gamma-ray astronomy*, Nucl. Inst. Meth. in Phys. Res, vol. 107, pp 385-394, 1973.
[2] R. W. Todd, et al., *A Proposed Gamma- Camera*, Nature 251, pp. 132-134, 1974.
[3] A. Knopf, K. Parodi, T. Bortfeld, H. A. Shih and H. Paganetti, *Systematic Analysis of Biological and Physical Limitations of Proton Beam Range Verification with Offline PET/CT Scans*, Physics in Medicine and Biology, vol. 54, pp. 4477-4495, 2009.
[4] C. Polf, S. Peterson, G. Ciangaru, M. Gillin and S. Beddar, *Prompt Gamma-ray Emission from Biological Tissues during Proton Irradiation: A Preliminary Study,* Physics in Medicine and Biology, vol. 54, pp. 731-743, 2009.
[5] L. Mihailescu et al., *Compact Compton Imager*, LLNL Technical Report, August 2005.
[6] G. Knoll, *Radiation Detection and Measurements*, J. Wiley and Sons, 2000.
[7] L. Mihailescu et al., *SPEIR: a Ge Compton Camera*, Nuclear Instruments and Methods in Physics Research A, 570, pp. 89-100, 2007.
[8] L. Mihailescu, Lawrence Berkeley National Laboratory, Berkeley, CA, USA, private communications.
[9] K. Vetter et al., *High-Sensitivity Compton Imaging with Position-Sensitive Si and Ge Detectors*, Nuclear Instruments and Methods in Physics Research Section A, vol. 579, pp. 363-366, 2006.
[10] N. J. Hammond, T. Duguet and C. J. Lister, *Ambiguity in Gamma-ray Tracking of Two Interaction Events*, Nuclear Instruments and Methods, vol. 547, pp. 535-540, 2005.
[11] J. Allison et al., *Geant4 Developments and Applications*, IEEE Transactions on Nuclear Science 53 No. 1 (2006) 270-278.
[12] S. Agostinelli et al., *Geant4 A Simulation Toolkit*, Nuclear Instruments and Methods A 506 (2003) 250-303
[13] L. Mihailescu et al., *Methods for Increasing the Efficiency of Compton Imagers*, IEEE Nuclear Science Symposium, 2005.
[14] W. H. Emerson, *Differing Angles on Angle*, Metrologia, vol. 42, L23-L26, 2005.
[15] S. Tryka, *Angular Distribution of the Solid Angle at a Point Subtended by a Circular Disk*, Optics Communications vol. 137, pp. 317-333, 1997.
[16] E. Galiano and C. Pagnutti, *An Analytical Solution for the Solid* Angle Subtended by a Circular Detector for a Symmetrically Positioned Linear Source, Applied Radiation and Isotopes, vol. 64-5, pp. 603-607, 2006.
[17] M. J. Prata, *Analytical Calculation of the Solid Angle Defined by a Cylindrical Detector and a Point Cosine Source with Parallel Axes*, Radiation Physics and Chemistry, vol. 69-4, pp. 273-279, 2004.

CHAPTER II

EVALUATION OF THE ERRORS AFFECTING IMAGING PARAMETERS

2.1 INTRODUCTION

When evaluating parameters used for image reconstruction through Compton scattering, some errors are produced. The errors concern both the accuracy and precision of the measurements and are determined by the capability of the detection system of observing the parameters or the quantities used to derive the imaging parameters. The quantities that at present can be measured by the detection system discussed in Chapter 1 and employable for Compton imaging are: the energy transferred to the orbital electron deposited during an incoherent scattering of the gamma-ray in the detection system, and location of the energy deposition. On the basis of these measured quantities, and analytical methods used to infer the photon interaction chronology, the following parameters are derived: the angle θ associated with an incoherent scattering of a photon in the detection system, and the first and second position of interaction of the gamma-ray, which identify the reference direction for the scattering angle. These parameters identify a cone of aperture θ which describes the region of space from where the gamma-ray could have been emitted.

In determining the scattering angle, it is assumed the energy of the incoming photon is known a-priori, the energy of the recoil electron is measured, and that the momentum vector of the orbital electron before the impact is unknown. Since the electron momentum before the impact is unknown, the scattering angle can not be identified following a model that takes into account the electron momentum before impact. The scattering angle is thus determined under the assumption that the electron is free and at rest according to the Compton formula. This assumption leads to a deviation between the actual scattering angle and the estimate of it. The deviation is estimated as a function of the binding energy of the electron and its momentum vector. The error on the scattering angle due to the error of the detector on the measurement of the energy transferred to the recoil electron during the impact is also estimated.

The cone axis is determined by the first and second position of interaction of the gamma-ray within the detector. The error on the direction of the cone axis due to the detector error on position of interaction is estimated. For what concern errors on the energy deposition and position of interaction only the errors due to a finite precision of the instrument are characterized and theoretically evaluated; detector accuracy errors are not theoretically characterized within this study. Also, errors due to the process of identifying interaction chronology are not theoretically characterized within this study. Their effect on the image is evaluated as the deviation of images produced using theoretically estimated errors and empirical errors.

2.2 ERROR ON SCATTERING ANGLE DUE TO THE MOMENTUM AND BINDING ENERGY OF THE ORBITAL ELECTRON

The deviation between the scattering angle of a photon colliding on a bound orbital electron and the estimate of it, which is obtained under the assumption that the orbital electron is free and at rest, is evaluated. The deviation is estimated assuming the orbital electron can occupy any of the orbital energy levels of typical detector materials, such as Si and Ge. It is assumed that the photon, of energy in the order of 392 keV to 662 keV, has an equal probability to collide with any of the electrons occupying any energy level. According to these assumptions, the systematic error on the scattering angle has an equal probability of assuming any of the values determined by the scattering of the photon with an orbital electron occupying any energy level. The largest angular deviation, as determined by an interaction with a K-shell electron, and the average angular deviation, computed over all of the energy levels, are employed herein as measures of the systematic error on the scattering angle.

2.2.1 INCOHERENT SCATTERING OF A PHOTON WITH A BOUND ELECTRON

For the treatment of the incoherent scattering between a photon and a bound electron, it is assumed that the orbital electron revolves about the nucleus in a well defined orbit. The Coulomb force of attraction of the nucleus is balanced by the centripetal force of the electron and the Coulomb force due to the other electrons is neglected. Under these assumptions, the balance between the centripetal force of the electron and the Coulomb force of attraction is expressed as:

$$\left|\frac{m_e v^2}{r}\right| = \left|\frac{1}{4\pi\varepsilon_0}\frac{Ze^2}{r^2}\right| \tag{2.1}$$

Here, m_e is the rest mass of the electron, v is the electron velocity, r is the electron orbit radius, Z is the atomic number, e is the charge of the electron, and ε_0 is the permittivity of free space. From this balance, assuming non relativistic energy, the expression for the kinetic energy of the electron is obtained:

$$\left|\frac{1}{2}m_e v^2\right| = \left|\frac{1}{8\pi\varepsilon_0}\frac{Ze^2}{r}\right| \tag{2.2}$$

Comparing equation 2.1 and equation 2.2, it is observed that the kinetic energy of the orbital electron is half of the potential energy:

$$\left|E_{e\,potential}\right| = 2\left|T_{e\,kinetic}\right| \tag{2.3}$$

The total orbital electron energy, indicated as the binding energy *B*, is:

$$\left|E_{e\,tot}\right| = \left|T_{e\,kinetic}\right| - \left|E_{e\,potential}\right| = -\left|B\right| \tag{2.4}$$

By comparing equation 2.3 and 2.4 the following expression for the electron binding energy is obtained in terms of the electron kinetic energy:

$$\left|T_{e\,kinetic}\right| = \left|B\right| \tag{2.5}$$

Equation 2.1 to equation 2.5 describe the simplest model of the atom, with respect to the orbital electron, adopted for evaluating the scattering angle of the photon with the bound electron. The schematic representation of the kinematics during scattering and the definition of parameters is illustrated in Figure 1. As shown in the figure, any momentum transfer to the atom during collision is neglected.

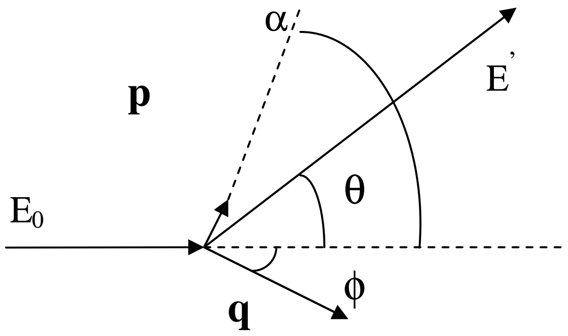

E_0: Photon energy before collision
E': Photon energy after collision
p: Electron momentum before collision
q: Electron momentum after collision
θ: Scattering Angle

Fig. 1. Incoherent scattering kinematics representation and symbol definition.

Under the assumption of negligible energy transfer to the atom, the momentum balance equation during scattering is expressed along the two dimensional coordinates as:

$$\begin{cases} \dfrac{E_0}{c} + p\cos(\alpha) = \dfrac{E'}{c}\cos(\theta) + q\cos(\phi) & (2.6) \\[2ex] p\sin(\alpha) = \dfrac{E'}{c}\sin(\theta) - q\sin(\phi) & (2.7) \end{cases}$$

Combining equation 2.6 and 2.7 to eliminate ϕ leads to equation (2.8):

$$2\left[\frac{E_0E'}{c^2q^2} + \frac{pE'\cos(\alpha)}{cq^2}\right]\cos(\theta) + 2\frac{E'p\sin(\alpha)}{cq^2}\sin(\theta) = \frac{E_0^{\;2}}{c^2q^2} + \frac{E'^2}{c^2q^2} + 2\frac{E_0\,p}{cq^2}\cos(\alpha) + \frac{p^2}{q^2} - 1$$

The energy balance equation during scattering is expressed as:

$$E_0 + T_{e\,kinetic} - E_{e\,potential} = E' + T_e'_{\,kinetic} - E_e'_{\,potential} \tag{2.9}$$

Here $T_{e\,kinetic}$ is the electron kinetic energy before impact, $T_e'_{kinetic}$ is the electron kinetic energy after impact, $E_{e\,potential}$ is the electron potential energy before impact and $E_e'_{potential}$ is the electron potential energy after impact.

If the energy transfer is sufficient to set the electron free (i.e. it brings the electron to a potential energy that is negligible), the energy balance equation is:

$$E_0 + T_{e\,kinetic} - E_{e\,potential} = E' + T_e'_{\,kinetic} \qquad E_0 - E' > B \tag{2.10}$$

Making use of equation 2.4, equation 2.10 assumes the following formalism:

$$E_0 - B = E' + T_e'_{\,kinetic} \tag{2.11}$$

Thus the energy lost by the gamma-ray during scattering is expressed as:

$$E_0 - E' = B + T_e'_{\,kinetic} \tag{2.12}$$

The momentum and energy balance equations, equation 2.8 and 2.12, are used to obtain an expression for the scattering angle, θ, as a function of the recoil electron kinetic energy, which is the measured quantity. For the reminder of this chapter, because of editing purposes, the symbol T_e' replaces the symbol $T_e'_{kinetic}$ and T_{e0} replaces the symbol $T_{e\,kinetic}$. The two-equations system is summarized for illustration purposes as:

$$\begin{cases} 2\left[\dfrac{E_0E'}{c^2q^2} + \dfrac{pE'\cos(\alpha)}{cq^2}\right]\cos(\theta) + 2\dfrac{E'p\sin(\alpha)}{cq^2}\sin(\theta) = \dfrac{E_0^{\,2}}{c^2q^2} + \dfrac{E'^2}{c^2q^2} + 2\dfrac{E_0\,p}{cq^2}\cos(\alpha) + \dfrac{p^2}{q^2} - 1 \\[2ex] E_0 - E' = B + Te' \qquad\qquad E_0 - E' > B \end{cases}$$

The momentum of the electron after collision is evaluated in terms of the electron kinetic energy, under relativistic conditions, as:

$$q^2c^2 = T_e'^2 + 2m_ec^2T_e' \tag{2.13}$$

and, according to our model, the momentum of the electron before collision under relativistic conditions is evaluated as:

$$p^2c^2 = B^2 + 2m_ec^2B \tag{2.14}$$

- When the electron is free and at rest, the energy and momentum balance equations are expressed as:

$$B = 0 \qquad \Rightarrow \qquad \begin{cases} 2\left[\dfrac{E_0E'}{c^2q^2}\right]\cos(\theta) = \dfrac{E_0{}^2}{c^2q^2} + \dfrac{E'^2}{c^2q^2} - 1 & (2.15) \\ \\ E' = E_0 - Te' & (2.16) \end{cases}$$

Solving the system given by equation 2.15 and 2.16 leads to the Compton formula, as expected:

$$\cos(\theta) = 1 - \frac{m_ec^2T_e'}{E_0(E_0 - T_e')} \tag{2.17}$$

- When the electron is not bound but is free and it has a momentum, *p*, along the direction of the incoming photon , the energy balance equation is:

$$E_0 + T_{e0} = E' + T_e' \tag{2.18}$$

Combining equation 2.19 with the momentum balance equation 2.12, the following expression is obtained:

$$\cos(\theta) = \frac{E_0{}^2 - T_e'E_0 - T_e'm_ec^2 - T_e'T_{e0} + T_{e0}E_0 + m_ec^2T_{e0} + T_{e0}{}^2 \pm E^0\sqrt{T_{e0}{}^2 + 2m_ec^2T_{e0}}}{E_0{}^2 - E_0T_e' + T_{e0}E_0 \pm \sqrt{T_{e0}{}^2 + 2m_ec^2T_{e0}}\,(E_0 - T_{e0} - T_e')} \tag{2.19}$$

where the positive sign refers to $\alpha = 0$ deg and the negative sign to $\alpha = 180$ deg. Note that setting *cos(θ)=1* gives an expression for the minimum kinetic energy of the electron after collision that is equal to the kinetic energy of the electron before the impact.

- When the electron is bound and its momentum, *p*, is along the direction of the incoming photon , from equation 2.8 and 2.12, the following expression for the scattering angle is obtained:

$$\cos(\theta) = \frac{E_0{}^2 - T_e'E_0 - T_e'm_ec^2 + T_e'B - BE_0 + m_ec^2B + B^2 \pm E^0\sqrt{B^2 + 2m_ec^2B}}{E_0{}^2 - E_0T_e' - BE_0 \pm \sqrt{B^2 + 2m_ec^2B}\,(E_0 - B - T_e')} \tag{2.20}$$

where the positive sign refers to $\alpha = 0$ deg, that is the case of the electron moving away from the photon, and the negative sign refers to $\alpha = 180$ deg, that is the case of the electron moving towards the photon.

Note that setting $cos(\theta)=1$ gives an expression for the minimum kinetic energy of the electron after collision. This quantity does not depend on the incoming photon energy, but it does depend on the electron energy before collision. For a K-shell electron of silicon, which has binding energy of 1.8 keV, the minimum kinetic energy after the impact, $T_e'_{min}$, is 1.5 keV when $\alpha = 180$ deg, and 2.1 keV, when $\alpha = 0$ deg. This result is obtained under the assumption that any momentum and energy transfer to the atom is negligible.

Literature references used to derive the model for computing the scattering angle for a bound electron are indicated in bibliography [1], [2], [3], [4], [5], [6], [7].

2.2.2 RESULTS

The scattering angle has been obtained for a bound electron making use of equation 2.18 for all of the orbital energy levels of silicon and germanium. The binding energy for each level is shown in Table 1.

The scattering angle, as obtained for the case of a bound electron moving towards the photon or away from the photon and for a free electron and at rest, as obtained with the Compton formula, are shown from Figure 2 to Figure 7 for the silicon and germanium atoms at different energies of the incoming photon.

	K	L1	L2	L3	M1	M2	M3	M4	M5	N1	N2	N3
Ge	11.10	1.414	1.247	1.216	0.180	0.127	0.120	0.028	0.028	0.005	0.002	0.002
Si	1.838	0.148	0.995	0.098	0.007	0.003	0.003					

Tab. 1. Binding energy in kev for silicon and germanium atomic electrons [1].

Since the orbital electron with which the gamma-ray undergoes collision is unknown, the error on the scattering angle can not be uniquely identified. Estimating the error as the largest possible deviation implies assuming that scattering occurs with the electron on the K shell. This error is the largest deviation not representative of the actual systematic error. Univocal estimate of the systematic error is not possible when the orbital shell where the recoil electron resides is unknown. To provide a less penalizing estimate of the systematic error, the average systematic error is evaluated by computing the average scattering angle over all orbital electrons. This is done by computing the average of equation 2.20 over all energy levels for electrons moving away and towards the photon. By expressing equation 2.20 according to the following formalism:

$$\cos(\theta) = f(E_0, T_e', B_{ij}) \tag{2.21}$$

where B_{ij} is the binding energy of the i^{th} shell, and j^{th} sub-shell, the average scattering angle is computed as:

$$\cos(\theta)_{average} = \sum_{i=K}^{I} \frac{\sum_{j=1}^{J} n_{ij} f(E_0, T_e', B_{ij})}{Z} \tag{2.22}$$

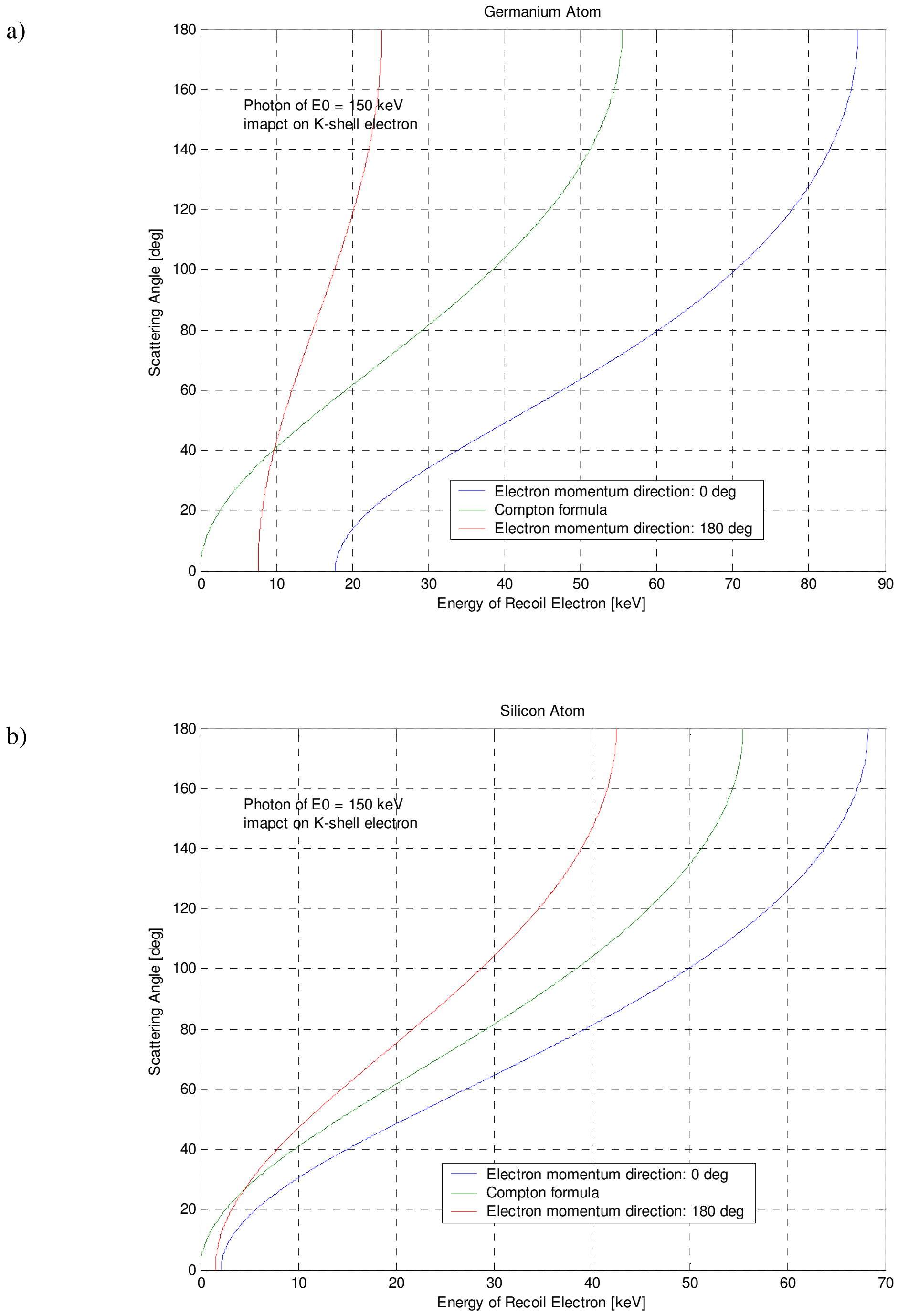

Fig. 2. Scattering angle versus energy of recoil electron for a 150 keV photon impact on a k-shell electron of : a). Germanium atoms; b) Silicon atoms.

a)

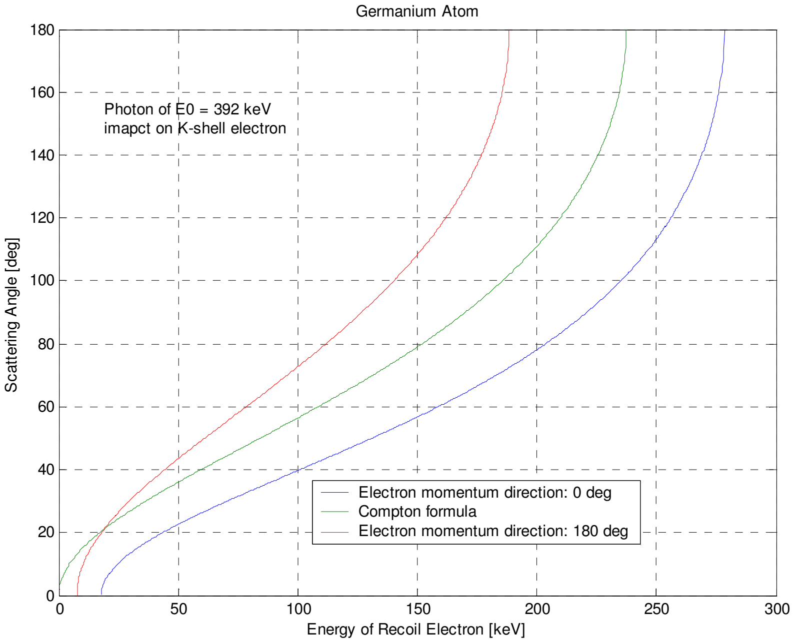

b)

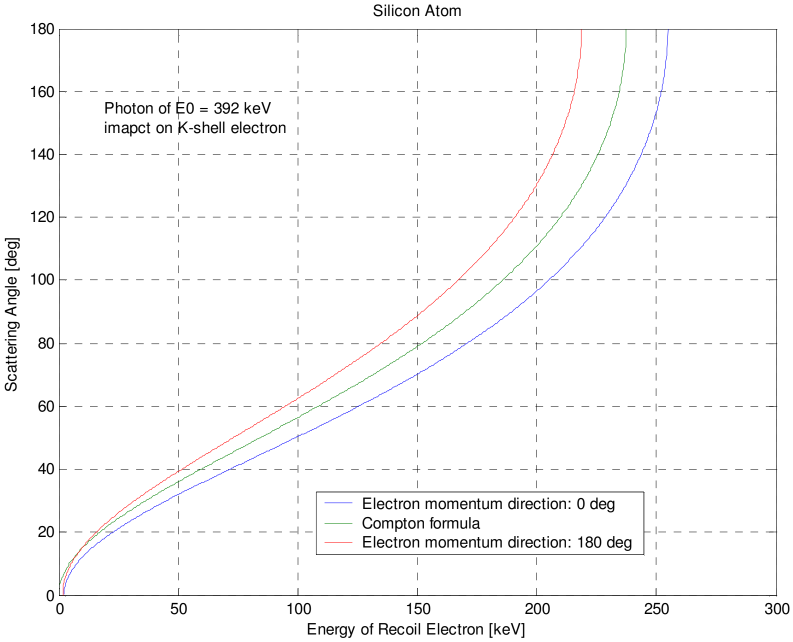

Fig. 3. Scattering angle versus energy of recoil electron for a 392 keV photon impact on a k-shell electron of: a) Germanium atoms; b) Silicon atoms.

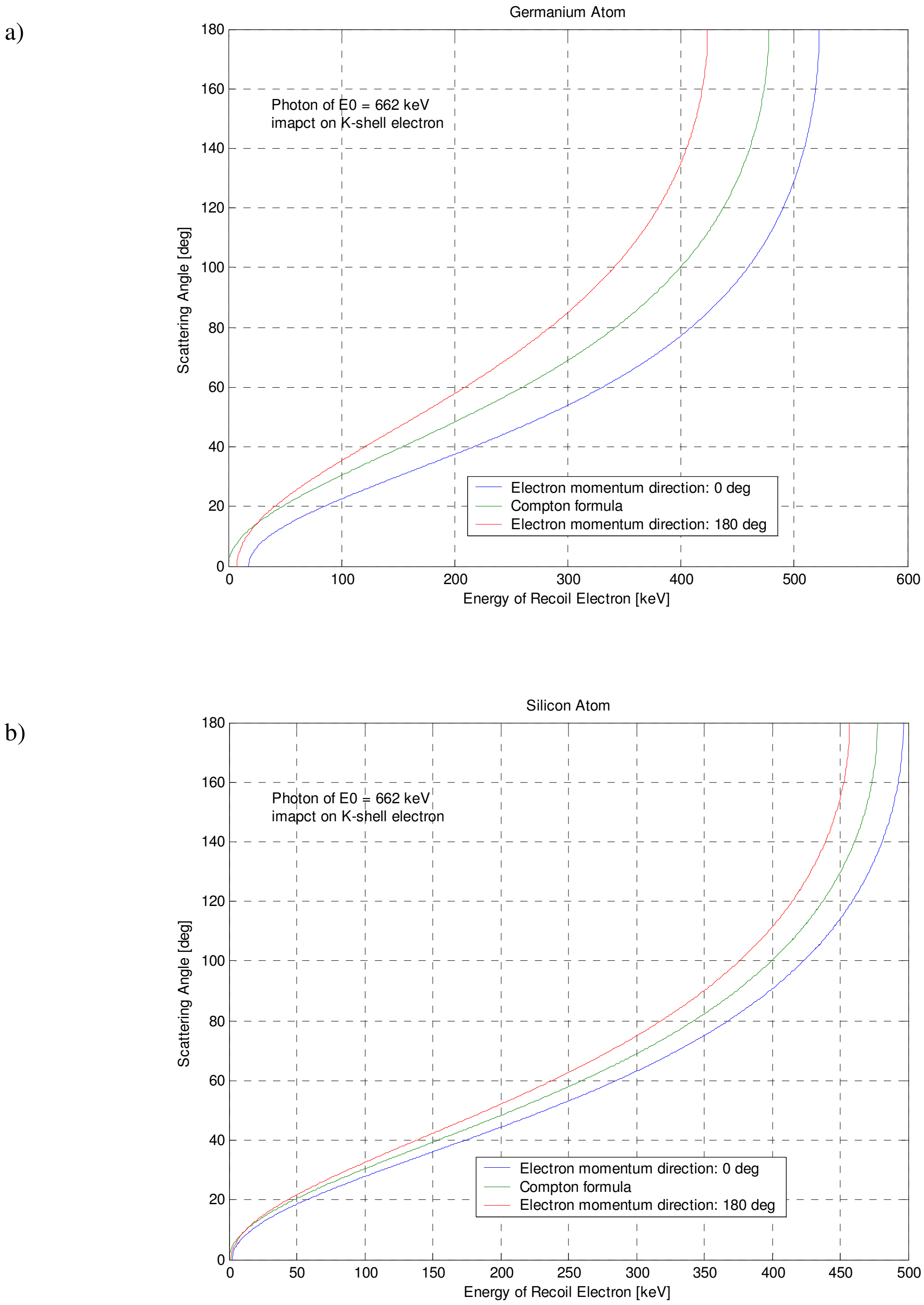

Fig. 4. Scattering angle versus energy of recoil electron for a 662 keV photon impact on a k-shell electron of: a). Germanium atoms; b) Silicon atoms.

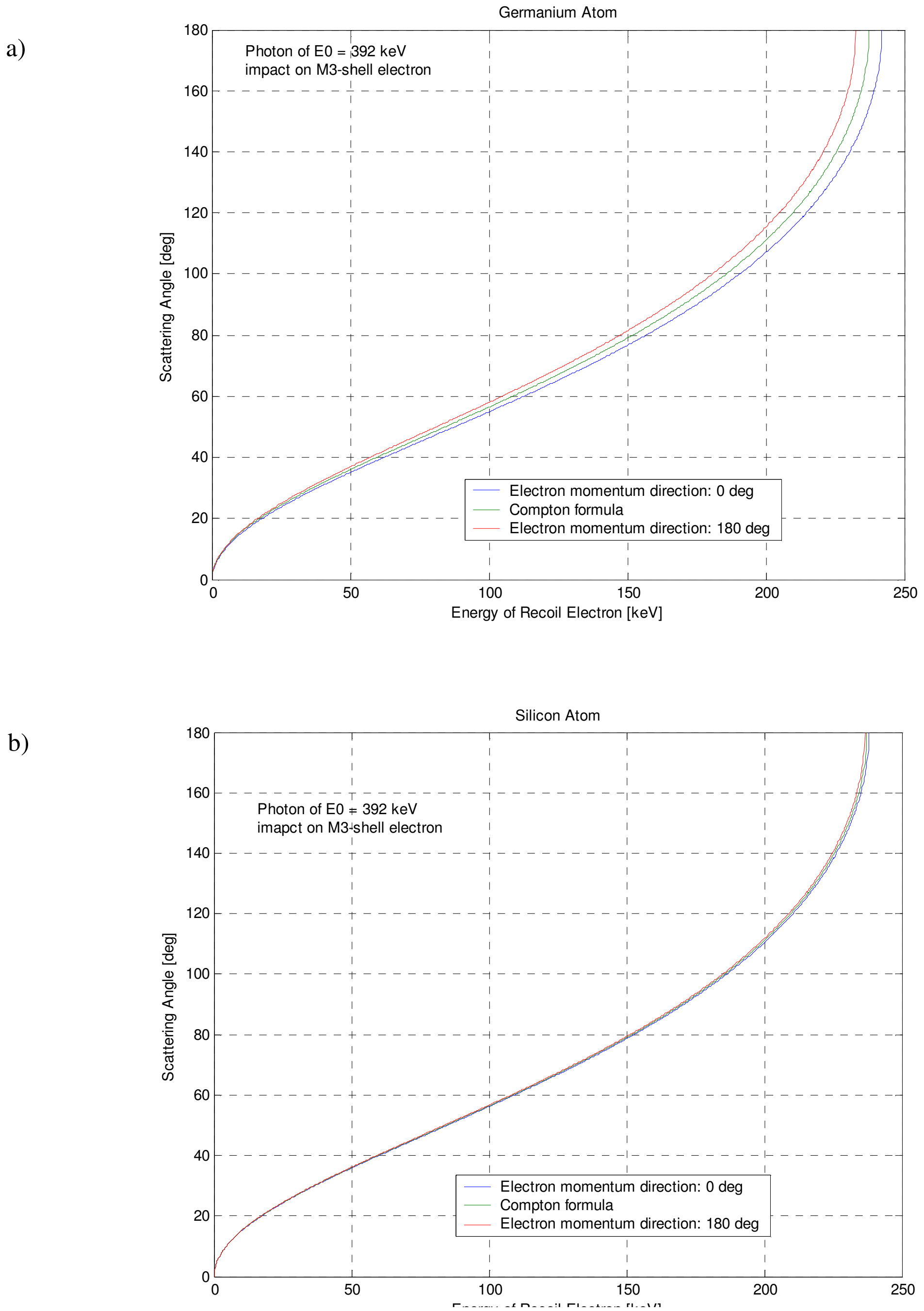

Fig. 5. Scattering angle versus energy of recoil electron for a 392 keV photon impact on a M3-shell electron of: a). Germanium atoms; b) Silicon atoms.

a)

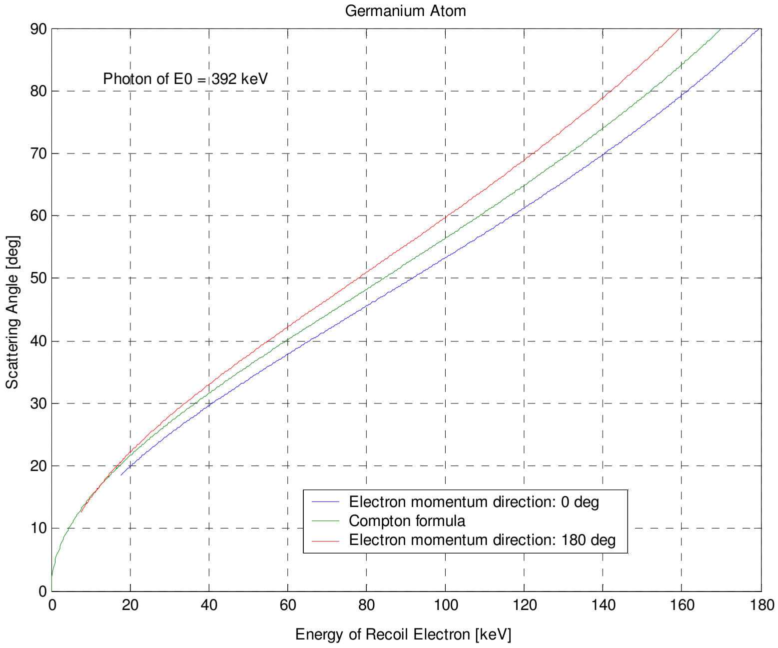

b)

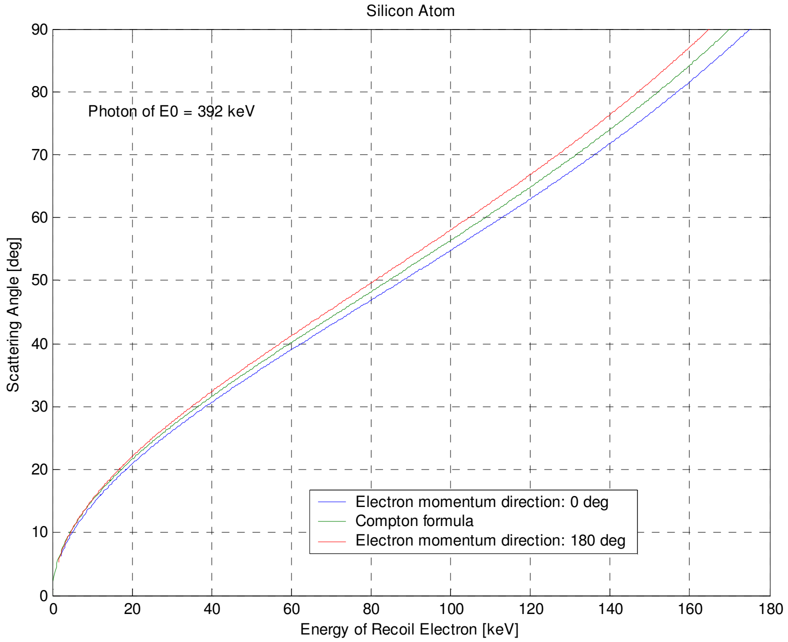

Fig. 6. Average scattering angle over all orbital electrons as a function of recoil electron energy for a 392 keV photon impact on: a). Germanium atoms; b) Silicon atoms.

a)

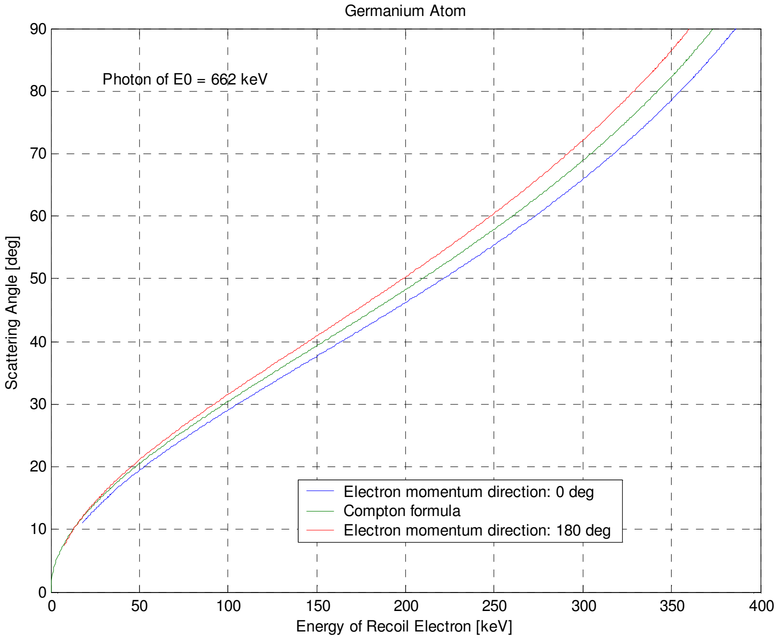

b)

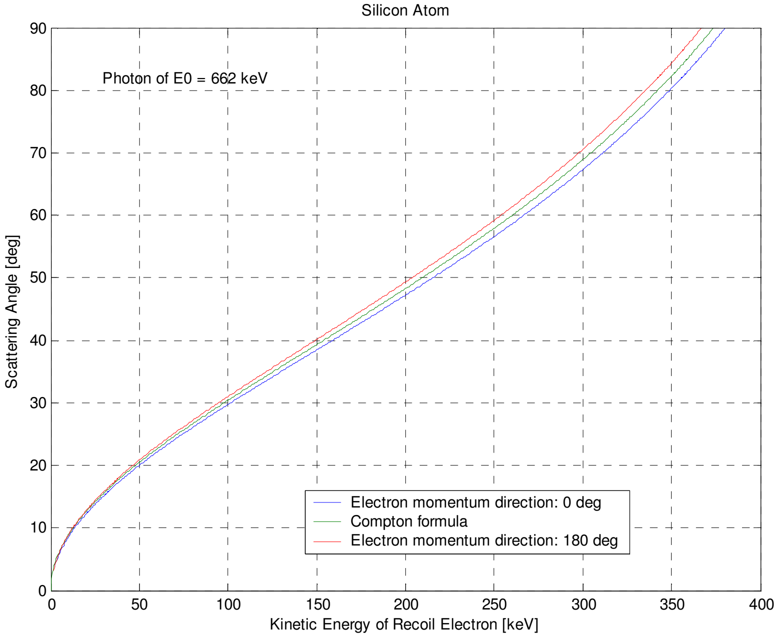

Fig. 7. Average scattering angle over all orbital electrons as a function of recoil electron energy for a 662 keV photon impact on: a). Germanium atoms; b) Silicon atoms.

where I is the outermost shell, J is the least energetic sub-shell, Z is the atomic number, and n_{ij} is the number of electrons in the i^{th} shell and j^{th} sub-shell. This computation of the average scattering angle implies assuming that the photon has equal probability of colliding with any electron occupying any energy level. The average scattering angle is shown in the following figures together with the scattering angle obtained using the Compton formula.

For a given incoming photon energy and scattering angle, the kinetic energy of the recoil electron after the impact depends on the binding energy of the electron before the impact. Thus the value of the maximum energy of the recoil electron, obtained at 180 degrees scattering angle, and the minimum energy of the recoil electron, obtained at 0 degrees scattering angle, depend on the binding energy of the electron. For energies of the recoil electron larger or smaller than a certain value, only scattering with an electron on a particular energy level is possible. The average scattering angle is computed for scattering that can occur with all of the electrons occupying any energy level. For a 0 degrees scattering angle, if the recoil electron energy is smaller than a certain value, scattering can not occur with the K shell electron, for example. Thus the average scattering angles is computed for recoil electron energies larger than a certain threshold. Similarly, for large scattering angles, there is a threshold on the upper value of the recoil electron energy, above which scattering can occur only with outermost electrons. This imposes a upper threshold on the recoil electron energy for computation of the average scattering angle, if this is done assuming scattering can occur with all orbital electrons. For these reasons the curves shown in Figure 6 and Figure 7, do not show values for small and large scattering angles. The curves could have been computed also for small and large values of the scattering angle but they would have presented discontinuities, because only a subset of the orbital electrons can be involved. In particle Compton imaging applications all scattering angles used for image formation are in between these upper and lower threshold. Hence there is a minimum energy of the recoil electron energy that the detector can observe; for the system discussed in paragraph 1.3 it is about 20 degrees. Moreover, only scattering angles smaller than 90 degrees are employed for image formation.

2.3 ERROR DUE TO MEASUREMENT UNCERTANTY

The measured imaging parameters are affected by errors due to both precision and accuracy. Accuracy errors in both energy deposition and position of interaction, given for example, by spurious processes and spurious signals of the detection system are not characterized within this study. Since no time resolution is available to define the sequence chronology, accuracy errors can also be due to the ambiguity in discerning interactions occurring so close to each other, that they produce signals on the same electrodes, and this might result in erroneous reconstruction of gamma-ray sequences. In the effort to achieve as high of an efficiency as reasonable, ambiguous sequences might be used for image reconstruction and some erroneous sequences might be used because un-practical to discern that they carry an error. These types of errors committed in discerning close interactions happening under no time resolution capability are not characterized within this study. For the reminder of this study, sequences carrying erroneous estimates on the average position of interaction, energy deposition, above the precision of the instrument, or carrying errors on the chronology of interaction, are regarded as of being responsible for the broadening of the impulse response of the empirical data with respect to the impulse response of the simulated data.

2.3.1 POSITION UNCERTANTY

The measurement of the position of interaction of the photon within the detection system is affected by an error due to the intrinsic resolution of the detection system. The linear error on the position of interaction results in an angular error affecting the direction between the first and second interaction. This results in an angular error on the cone axis direction, $\delta\phi$, applied at the middle point connecting the first and second interaction. If we assume the error affecting the position of interaction is the same along the three linear dimensions, the error on the direction between the first and second interaction, $\delta\phi$, is determined by geometric considerations as shown Figure 8. The model assumes the region of space having side equal to the error, with centroid located on the position of interaction, being equivalent to a spherical region of diameter equal to the error.

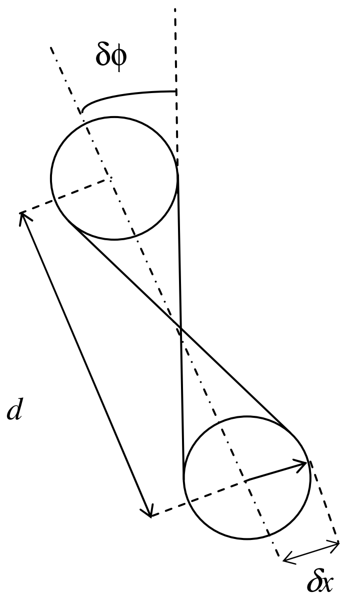

d: Distance between first and second gamma-ray interaction
dx: Position precision of detection system
δϕ: Error affecting cone axis direction

Fig. 8. Illustration of the methodology used for determination of the error affecting cone axis.

The angular error on the cone direction is:

$$\delta\phi = \tan^{-1}\left(\frac{2\delta x}{d}\right) \tag{2.23}$$

The angular error on the cone axis direction results in a linear error that depends on the distance of a location in field of view from the middle point between first and second gamma-ray location.

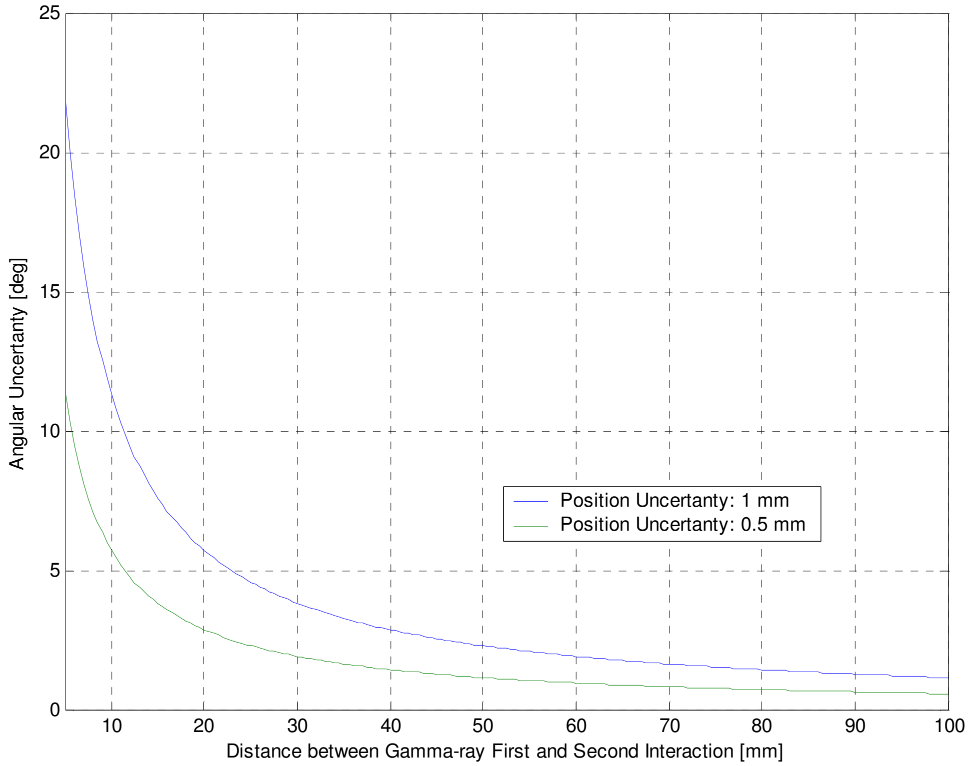

Fig. 9. Uncertainty affecting the cone axis direction due to the uncertainty in defining the location of a gamma-ray interaction. The error originates at the middle point between first and second interaction.

2.3.2 ENERGY UNCERTANTY

The measurement of the kinetic energy of the scattered electron following an incoherent interaction, T_e', is affected by an error due to the intrinsic resolution of the detection system. Energy resolution values of about 1.4 keV at 60 keV and 2.5 keV at 1332 keV are obtained for the detection instrument used to acquire the measurements and discussed in paragraph 1.3 [8]. The estimate of the energy uncertainty as a function of recoil electron energy is obtained in first approximation by linear interpolation of the two values for relatively small energy range, as done in [9] for the measured data, to be consistent with errors calculated for the experimental data.

The energy uncertainty in the measured kinetic energy of the recoil electron results in an error affecting the scattering angle θ. The scattering angle as a function of the kinetic energy of the recoil electron has been obtained in paragraph 2.2 for an electron occupying any atomic energy level and moving towards and away from the incoming photon. The average scattering angle, obtained assuming the photon has equal probability to interact with electrons in all atomic energy levels, is used to estimate the error on the scattering angle as a function of a measured kinetic energy of the recoil electron. The error in the observed recoil electron energy results in turn in an additional error on the scattering angle. The methodology used to estimate the total error on the scattering angle is shown in figure 10. Given the measured recoil electron enrgy, it is assumed the minimum possible value of the actual recoil electron energy is this observed value minus the measurement error, and the maximum possible value is the observed value plus the error. The scattering angles are then computed for both energy values using equation 2.20 and the largest deviations from the Compton formula are used as the total error on the scattering angle.

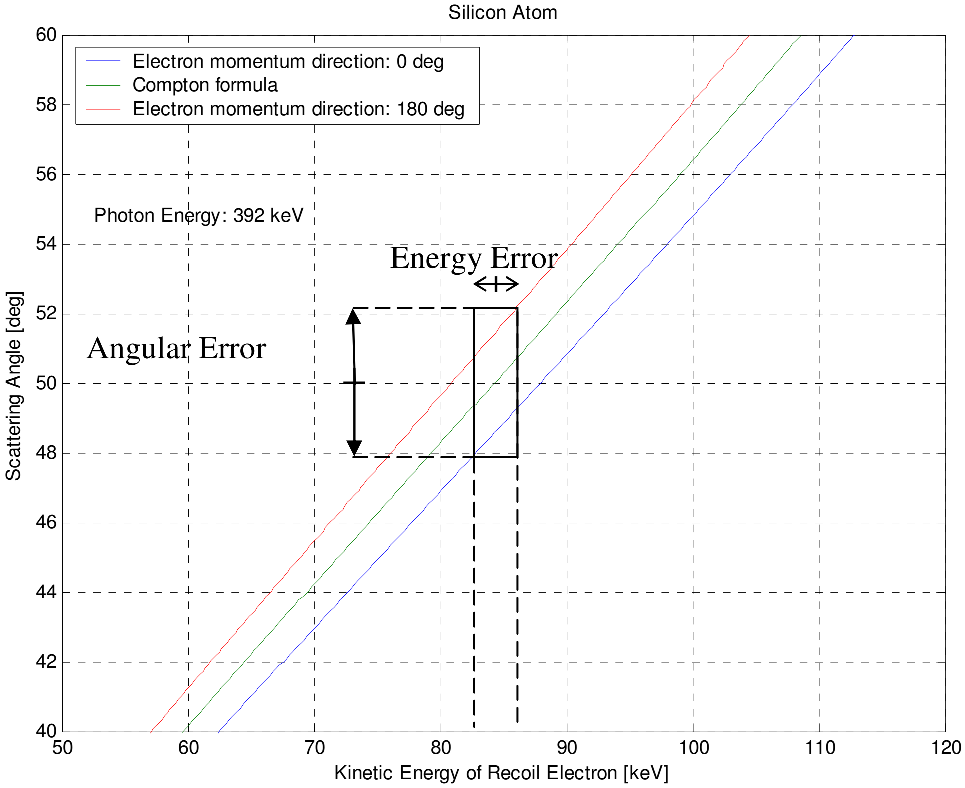

Fig. 10. Determination of Scattering Angle Uncertainty due to Electron Binding Effects and Detector Resolution of Energy Deposition. The average curves (over all energy levels of the orbital electron) of the scattering angle for an electron moving away and towards the photon are shown.

2.4 DISCUSSION

As discussed, the energy and position resolution of the detector result in an error on the scattering angle. The fact that scattering occurs with a bound electron and the momentum of the electron is unknown, results also in an error affecting scattering angle.

As summarized in Table 2, the estimate of the error on the scattering angle shows that relatively large deviations between the angle calculated using the Compton formula and the angle calculated assuming the electron is bound to the atom occur if the photon collides with a K-shell electron. The deviation decreases with energy of the photon and a significant reduction is obtained for a 392 keV photon with respect to a 140 keV photon. The estimate of the error, is more severe for germanium than silicon, due to the larger binding energy of innermost electrons. The fact that silicon is used as the material for the first detector and that the majority of the interaction sequences have first interaction in the first detector assist in obtaining smaller errors on the majority of cone apertures.

The error can not be uniquely determined because we can not establish which orbital electron underwent scattering with the photon. Assuming that the K-shell electron underwent scattering gives a conservative estimate of the error, and it overestimates the probability of collision between the photon and the K-shell electron. Electrons occupy 7 energy levels in Silicon and 12 in Germanium, as shown in Table 2, thus the photon has a significant probability to collide with the less tightly bound electrons. For the purpose of imaging, it is envisioned choosing to estimate the error as the average value obtained assuming the photon has equal probability to collide with any of the electrons occupying any energy level. Using atomic wave functions could improve collision probability estimates.

SILICON	Incoming Photon Energy: 150 keV			
Scattering Angle	30 deg	60 deg	90 deg	120 deg
K-shell Error	< 18	20	38	>60
Average Error	< 6	6.5	12	>20

SILICON	Incoming Photon Energy: 392 keV			
Scattering Angle	30 deg	60 deg	90 deg	120 deg
K-shell Error	4.5	7.5	12.0	> 25
Average Error	1.5	2.5	4.0	8.5

SILICON	Incoming Photon Energy: 662 keV			
Scattering Angle	30 deg	60 deg	90 deg	120 deg
K-shell Error	3.3	5.9	10	>20
Average Error	1.1	1.8	3.0	6.0

GERMANIUM	Incoming Photon Energy: 150 keV			
Scattering Angle	30 deg	60 deg	90 deg	120 deg
K-shell Error	> 40			
Average Error	> 10			

GERMANIUM	Incoming Photon Energy: 392 keV			
Scattering Angle	30 deg	60 deg	90 deg	120 deg
K-shell Error	12	20	>40	
Average Error	3.0	4.8	8.0	>10

GERMANIUM	Incoming Photon Energy: 662 keV			
Scattering Angle	30 deg	60 deg	90 deg	120 deg
K-shell Error	8.0	13.0	26	>30
Average Error	1.9	3.0	5.5	>8.0

Tab. 2. Uncertainty affecting the scattering angle due to electron binding effects and detector energy resolution, calculated at several photon energies, and for silicon and germanium, as a function of scattering angle.

An additional significant contribution to the uncertainty on the scattering angle is due to the detector resolution of position of interaction. According to the model discussed in paragraph 2.3.1, the error increases significantly with decreasing distance between the first and second gamma-ray interaction. Distances smaller than 10 mm, produce angular errors larger than 5 degrees for position resolutions of about 0.5 mm. Distances on the order of 50 mm to 60 mm, typical of the instrument used to acquire our measurements, determine an error lower than 1 degree for position resolutions of 0.5 mm and less than 2 degrees for position resolution of 1 mm. Thus, if one needs to limit the component of the error below 5 degrees, sequences having the first and second gamma-ray interaction taking place on the same detector must be discarded. The larger the distance between the first and second detector, the smaller is the fraction of multiple interaction sequences having first interaction in the first detector and second interaction in the second detector. Therefore an effort to minimize the error in the scattering angle by increasing the distance between the two detectors results in a loss of measurements that can be used for imaging. The effort of keeping the error on the scattering angle as low as reasonably achievable comes in this case at the expense of the maximum possible detection efficiency. When imaging radioactivity within a human being, detection efficiency is the determinant parameter that controls the dose to the patient, therefore there are limits below which detection efficiency can not be accepted. Given these limits, an analysis of the impact of the error on the image of empirical and simulated sources will guide, and eventually justify, the choice of discarding a significant fraction of the measurements for a superior image quality.

Bibliography

[1] *Table of Radioactive Isotopes*, E Browne, R. Firestone, Virginia Shirley Editor.

[2] S. Rosati, *Fisica Generale 1*, CEA, 1994.

[3] E. M. Hussein, *Handbook on Radiation Probing, Gauging and Imaging Analysis*, Springer, May 2003.

[4] K. S. Krane, *Introductory Nuclear Physics*, Wiley, October 1987.

[5] K. Bethge, G. Kraft, P. Kreisler, G. Walter, *Medical Applications of Nuclear Physics,* Springer 2004.

[6] W. R. Nelson, H. Hirayama and D.W.O. Rogers*, The EGS4 Code System*, SLAC-265, 1985, http://www.irs.inms.nrc.ca/EGS4/get_egs4.html.

[7] *Geant4 Code Manual*, CERN and KEK, 1993, http://geant4.web.cern.ch/geant4/

[8] K. Vetter et al., *Gamma-ray Imaging with Position Sensitive HPGe Detectors*, Nuclear Instruments and Methods in Physics Research A 5225 (2004) 322 – 327.

[9] L. Mihailescu et al., *SPEIR: a Ge Compton Camera*, Nuclear Instruments and Methods in Physics Research A, 570, pp. 89-100, 2007.

CHAPTER III

IMAGE RECONSTRUCTION METHODOLOGY

3.1 INTRODUCTION

Methodologies discussed in this chapter to estimate radioactive source distribution given the observed emissions from a source are simple backprojection and list-mode maximum likelihood expectation maximization algorithm. Both methodologies make use of observed gamma-ray interactions by the block-type detector system discussed in Chapter 1 using only one view of the source, and by a spherical detector enclosing the entire 4π field of view. The gamma-ray interaction sequences used for image reconstruction are multiple-interaction sequences because they allow for image reconstruction via backprojection and allow three-dimensional image reconstruction even when using only one view of the object because of the information carried on by the physical quantities that the detection system can observe.

3.2 SIMPLE BACKPROJECTION

Given gamma-ray emissions from the source, the attributes observed by the detection system are the gamma-ray interaction location and energy deposition. According to the physical principles discussed in detail in Chapter 1 and 2, these information allows the determination of the spatial locus of emission of the gamma-ray for each single gamma-ray emitted from the source: The energy deposited by the gamma-ray during the first interaction allows determination of the scattering angle; the position of first and second interaction, allow establishing a reference direction for the scattering angle. Under the assumption that the initial trajectory of the orbital electron after scattering is unknown, the locus of emission of the gamma-ray is identified with a cone of aperture equal to the scattering angle. Making use this information, image reconstruction via backprojection is adopted. Events that undergo scattering at least two times in the detector

are selected because they allow identification of the cone, while one interaction events do not allow restriction of the emission region except for the whole field of view.
Image reconstruction by simple backprojection is based on the criteria of assigning a weight to each voxel, *i*, for each cone, ***j***. What it is called weight, ω_{ij}, is used as an approximate estimate of the probability that the j^{th} gamma-ray was originated from a particular voxel *i*. The weights of each voxel *i*, each one of them determined by an event ***j***, are then summed over all events ***j*** to obtain an estimate of the intensity of the distribution of the gamma-ray emitting nuclide (i.e. the image):

$$f(i)_{est} \propto \sum_{\mathbf{j}} \omega_{ij} \tag{3.1}$$

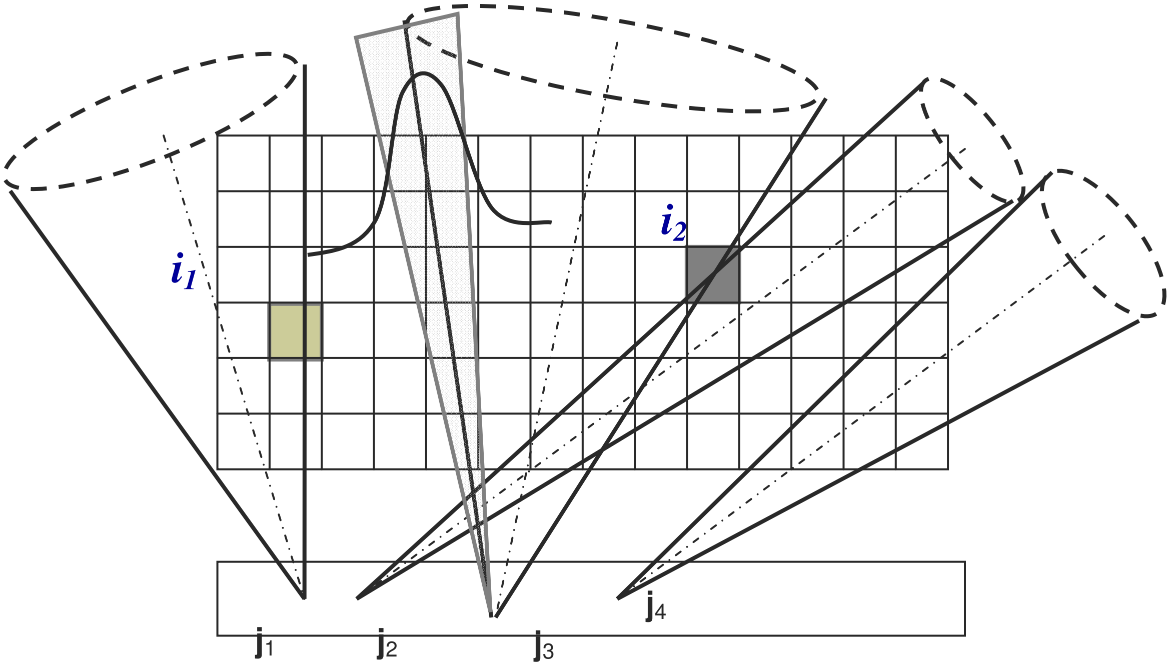

Fig. 1. Schematic representation of image reconstruction via simple backprojection. Voxels in field of view are identified with the symbol *i*, cones are identified with the symbol ***j***.

The estimate of the weight assigned to a voxel *i* for an event ***j*** is obtained by integrating a probability density function around the cone surface over the voxel volume v_i:

$$\omega_{ij} = \int_{vi} pdf(\mathbf{r}, \mathbf{j})\ d\mathbf{r} \tag{3.2}$$

If the cone parameters were not affected by errors, the probability density function associated with the location of emission of the gamma-ray could be described by a delta function of the type $\delta(\boldsymbol{r}\text{-}\boldsymbol{r_0})$, where $\mathbf{r_0}$ is the coordinate of a point on the cone surface. The error on the cone angular aperture and cone axis direction determines a deviation of the probability density function from a delta function. Given the angular nature of the error affecting cone aperture, a Lorentz distribution which is function of the angular distance of a point in space from the cone surface is adopted:

$$pdf(\theta, \theta_{oj}, \delta\theta_j) = (1/\pi)\frac{\delta\theta_j}{(\theta - \theta_{oj})^2 + \delta\theta_j^2} \tag{3.3}$$

where θ_{j0} is the aperture of the j$^{\text{th}}$ cone, θ-θ_{j0} is the minimum angular distance of a point in field of view from the j^{th} cone, and $\delta\theta_j$ is the error associated with the j^{th} cone aperture. The weight, ω_{ij}, is then calculated by integrating the probability density function over the voxel volume.

$$\begin{cases} \omega_{ij} = \displaystyle\int_{\theta_{\mathrm{ij}}\text{-asin}(R/L_i)}^{\theta_{ij}+\mathrm{a}\sin(R/L_i)} pdf(\theta, \theta_{0\mathrm{j}}, \delta\theta_{\mathrm{j}})\ S_{ij}(R, L_{ij}\ , \theta_{ij}, \theta\ )\, d\theta & \theta_{ij} - \theta_{0j} + \mathrm{asin}(R/L_i) \le n \cdot \delta\theta_j \\ \omega_{ij} = \displaystyle\int_{\theta_{\mathrm{ij}}\text{-asin}(R/L_i)}^{\theta_{0j}+n\cdot\delta\theta_j} pdf(\theta, \theta_{0\mathrm{j}}, \delta\theta_{\mathrm{j}})\ S_{ij}(R\ , L_{ij}\ , \theta_{ij}, \theta\ )\, d\theta & \theta_{ij} - \theta_{0j} + \mathrm{a}\sin(R/L_i) > n \cdot \delta\theta_j; \\ & \theta_{ij} - \theta_{0j} - \mathrm{a}\sin(R/L_i) < n \cdot \delta\theta_j \\ \omega_{ij} = 0 & \theta_{ij} - \theta_{0j} - \mathrm{a}\sin(R/L_i) \ge n \cdot \delta\theta_j \end{cases}$$

Fig. 2. Schematic representation of ω_{ij} determination.

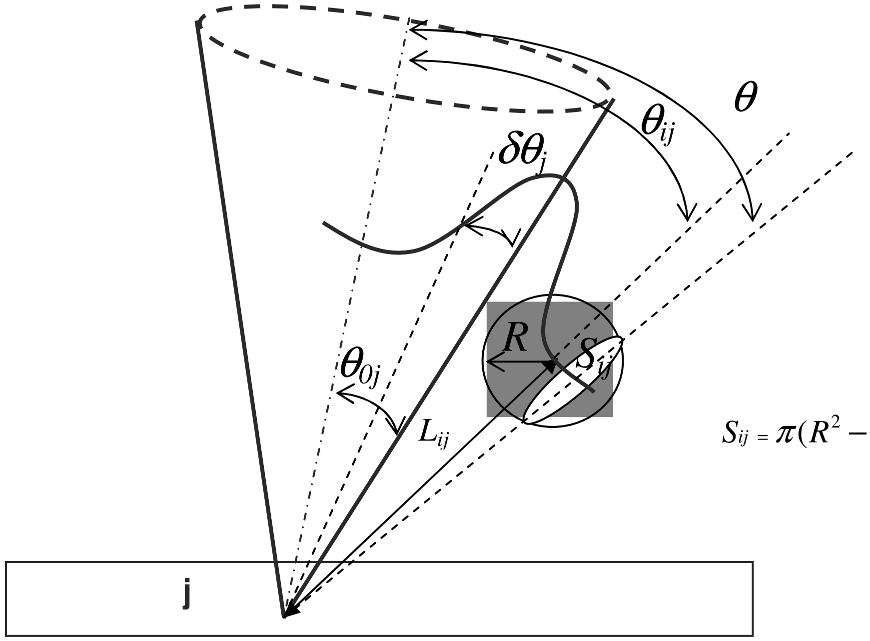

$$S_{ij} = \pi(R^2 - L_{ij}^{\ 2}\sin^2(\theta_{ij} - \theta))$$

Fig.3. Schematic representation of the determination of voxel weight.

The voxel is modeled as a sphere of equivalent radius *R*, according to volume conservation. The term S_{ij} is a surface integral that originates from the assumption that the radius of curvature of the cone at any location within the field of view is much larger than the voxel radius. L_{ij} is the distance between the cone vertex and the i^{th} voxel centroid; n is a value that describes the upper limit of integration (i.e. the integration is carried on up to a certain angular distance of a point in space from the cone surface). The integration limit is introduced because of eventual limitations of the computing platform used to evaluate image formation algorithms for any event $\boldsymbol{j}$ and voxel i. A minimum storage capability of the computing platform that is equivalent to the size of the number of voxels is needed. Images presented in this study have been produced by integrating up to a unitary multiple of the angular error.

3.3 MAXIMUM LIKELIHOOD EXPECTATION MAXIMIZATION ALGORITHM

Formulations and derivations of the maximum likelihood estimates from incomplete data sets via the expectation maximization algorithm are presented at different levels of generalities in [1]. The application of the expectation maximization algorithm to image reconstruction of a distributed radioactive source is discussed in [2]. When the observable attributes of emission photons from the source are binned into a set of discretized values (as an example of an attribute one can think to the position of interaction of the gamma-ray into a particular bin $\boldsymbol{j}$ of the detection system), the iterative expectation maximization algorithm assumes the following formalism:

$$f^{*}(l)^{k+1} = \frac{1}{P(l)} \sum_{\mathbf{j}} \frac{n(\mathbf{j})_{meas} f^{*}(l)^{k}\, p(l,\mathbf{j})}{\sum_{i} f^{*}(i)^{k}\, p(i,\mathbf{j})} \tag{3.4}$$

where $f^{*}(l)^{k+1}$ is the expected value of the intensity of voxel l at iteration step $k+1$; $P(l)$ is the probability of observing an emission from voxel l; $p(l,\boldsymbol{j})$ is the probability that an emission from voxel l is observed into bin $\boldsymbol{j}$ (i.e. probability that an emission from voxel l leads to an observed event with attributes $\boldsymbol{j}$); $n(\boldsymbol{j})_{meas}$ is the total number of observed events into bin $\boldsymbol{j}$.

By multiplying left and right sides of the equation by the detection probability of voxel l, the following expression is obtained:

$$n^{*}(l)^{k+1} = \sum_{\mathbf{j}} \frac{n(\mathbf{j})_{meas}}{n(\mathbf{j})^{k}_{est}} n(l,\mathbf{j})^{k}_{est} \tag{3.5}$$

Here $n(l)^{*k+1}$ is the expected value of the total number of observed events from voxel l at iteration step $k+1$; $n(\boldsymbol{j})_{est}$ is the estimate of the total number of observed events in bin $\boldsymbol{j}$, produced by the estimate of the total source, $n(l, \boldsymbol{j})_{est}$ is the estimate of the number of observed events in bin $\boldsymbol{j}$ produced by the estimate of the intensity of source voxel l, $f(l)^k$. The likelihood function is based on the physical principle that the emissions from source voxel l observed in detector element $\boldsymbol{j}$, $n(l,\boldsymbol{j})$, are independent Poisson's variables. If the observable attributes are not binned, the expectation maximization algorithm is derived from a different likelihood function, discussed in [3] and in [4]. The algorithm proposed by Parra assumes the following formalism:

$$f^{*}(l)^{k+1} = \sum_{\mathbf{j}} \frac{f^{*}(l)^{k}\, p'(l,\mathbf{j})}{\sum_{i} f^{*}(i)^{k}\, p'(i,\mathbf{j}) P(i)} \tag{3.6}$$

where, here, $p'(l,\mathbf{j})$, is proportional to the number of observable events with attribute $\boldsymbol{j}$ from voxel l, divided the total number of observable events from voxel l. In the binned measurements formalism the term $p(l,\boldsymbol{j})$ is proportional to the total number of observable events of type $\boldsymbol{j}$ from voxel l, divided the total number of emitted events from voxel l, therefore:

$$p(l,\mathbf{j}) = p'(l,\mathbf{j})P(l) \tag{3.7}$$

and the two algorithms, the one pertaining to binned observable attribute case and the other pertaining a list mode case, assume the same formalism and physical phenomenology with the particularity that $n(\mathbf{j})_{meas}$ in a list mode case is equal to one for most practical cases.

➢ *On The Implementation Of The List-Mode EM Algorithm For Compton Imaging*

In order to apply the list-mode EM algorithm to obtain the source estimate, knowledge of the probability that an emission from voxel l leads to an observable event of attribute $\boldsymbol{j}$, out of all possible observable events from l, is needed. This probability, computed for all voxels and all possible combinations of the observable attributes, describes what it is generally referred to as transformation matrix; this definition is used herein. In principle, several attributes of the observable events emitted from the source could be used to estimate source intensity. The criteria used for choosing the attributes are based on convergence of the algorithm. It has been shown that convergence is obtained if the transformation matrix is of full rank and there are more voxels than events [5]. This condition is generally not obtained in Compton imaging if one uses only one view of the object and the position of first gamma-ray interaction as the only attribute. Hence there is symmetry on the solid angle subtended by each detector element with respect to voxels at symmetric locations around the detector axis, and there is generally symmetry on the solid angle subtended by the source to detector elements at symmetric locations around detector axis, as shown in the figure below. The effect is to produce an equal estimate of the source intensity for voxels at symmetric locations around the detector axis, as illustrated in Fig. 3.

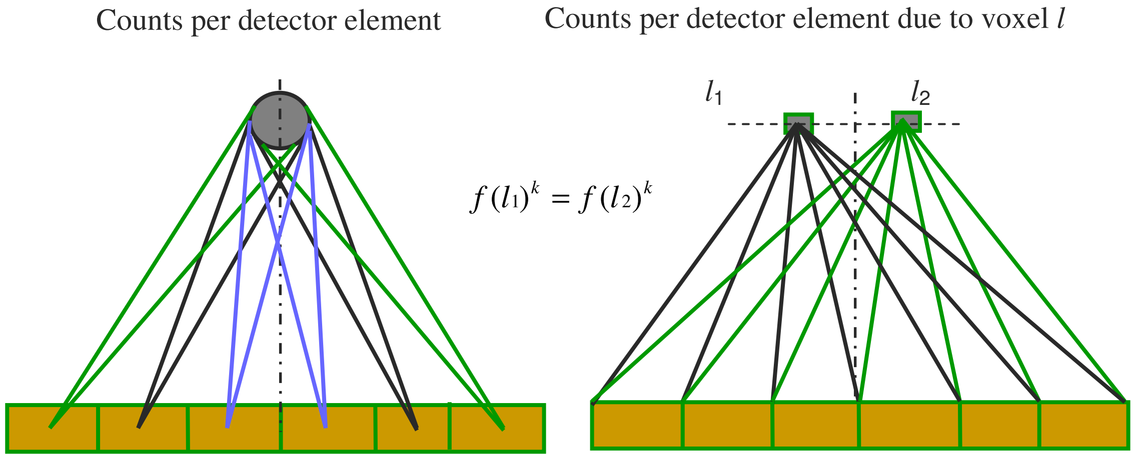

Fig.3. Schematic representation of symmetry between voxels in fov when using only one view and the position of interaction as only attribute.

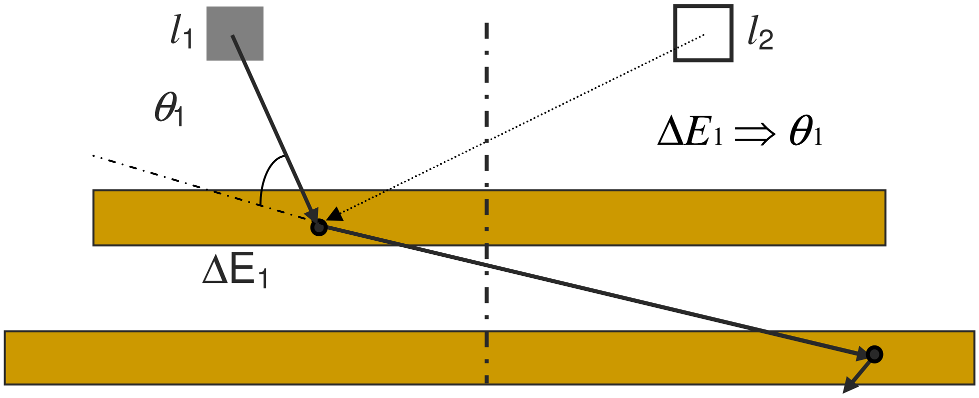

Fig. 4. Schematic representation of symmetry break when using multiple attributes, such as position of interaction and energy deposition.

The observable event attributes used for this analysis are the parameters that in backprojection allow identifying the cone: the position of first and second gamma-ray interaction and the energy deposition. The ensemble of these observable attributes identifies the useful information carried by the event for estimating source intensity. Event and attributes are often used with the same meaning for the reminder of this chapter, and the vector notation is dropped. The number of attributes that define an event, or the cone, are: the three coordinates of the vertex, the three coordinates of the second interaction, that together with the vertex coordinates identify the cone axis direction, and the cone aperture, a total of 7 attributes. Because the precision of the attributes given by the detection system is smaller than the smallest precision, or bin size, that can be processed, using the available computing tools, for computing the transformation matrix with relatively good statistics in an array of **N** x 7, where **N** is the array of the range of values that each attribute can assume divided precision of the attribute, it is chosen to use a list-mode approach. In the list mode approach each observable, detected event is treated as practically unique observed event of attributes ***j***; the attribute space is continuous, therefore the total number of observable events that each voxel can generate tends to infinity, and the number of event of type ***j*** that a voxel can generate, is either 0 if voxel *l* can not generate the event, or different from zero if the voxel *l* can generate it. The probability that, given a measurement from voxel *l*, this is of type ***j***, $p'(l,\boldsymbol{j})$, can be expressed as:

$$p'(l,j) = \frac{n(\mathbf{j},l)_{observable}}{n(l)_{observable}} \tag{3.8}$$

where $n(\boldsymbol{j},l)_{observable}$ is the number of observable events of type ***j*** from voxel *l*, $n(l)_{observable}$ is the totality of observable event from voxel *l*; in list-mode approach:

$$\lim_{n(l)observable\to\infty} p'(l,\mathbf{j}) = 0 \tag{3.9}$$

An attempt to use the list-mode maximum likelihood algorithm for Compton imaging is made by using the following expression for $p'(l,\boldsymbol{j})$:

$$p'(l,\mathbf{j}) \propto \omega_{lj} \tag{3.10}$$

where $\omega_{lj,}$ is the estimate of the likelihood that voxel *l* can generate an event of type ***j***, obtained as simple backprojection of the event, as discussed in paragraph 3.2:

$$\omega_{lj} \propto \int_{vl} pdf(\mathbf{r},\mathbf{j})\ d\mathbf{r} \tag{3.11}$$

This estimate does not exhaustively describe the likelihood; it describes weather or not a certain voxel can generate a certain event ***j*** and the probability that the voxel can generate the possible events is modeled as uniform. In reality a voxel generates the possible events with a probability that is not uniform; more accurate estimates of the probability through an analytical model are given in [6], [7]. By making use of the uniform approximation for the forward probability *p*'(*l*,***j***), the list-mode EM algorithm assumes the following formalism:

$$f(l)*^{k+1} = \sum_{j\cap l} \frac{\omega_{lj} f(l)^k}{\sum_{i\cap j} p(i)\omega_{ij} f(i)^k} \tag{3.12}$$

A similar approach is used in [4], although in this case the estimate of *p*'(*l*,***j***) is derived for a two dimensional positron emission tomography physics.
Therefore, in so doing, at each iteration step the estimate of the number of measurements coming from voxel *l,* is evaluated as:

$$n(l)*^{k+1} = \sum_{j\cap l} \frac{p(l) f(l)^k \omega_{lj}}{\sum_{i\cap j} p(i) f(i)^k \omega_{ij}} \tag{3.13}$$

and the physical meaning of the parameters in the algorithm is modified, because of the approximation made for the forward probability *p*'(*l*,***j***), with respect to the parameters exhaustively describing physical phenomena. This algorithm has been shown to produce relatively good results in two dimensional images produced using positron emission tomography with time of flight information [4]. In this case there is almost a one-to-one correspondence between a voxel and a measurements, (i.e in absence of measurement errors ω_{lj} is equal to one for a particular location in field of view and equal to zero for all other locations). In Compton imaging the number of voxels from which an event could be generated is larger than and it is also variable depending on the intersection between the cone surface and field of view.
Improved estimate of the forward probability *p*'(*l*,***j***), either via numerical simulation or analytical models, could lead to improved results in the image [8]. Analytical models have been proposed [6], [7], and could be used to evaluate improvements in the images.

Bibliography

[1] A. P. Dumpster et al., *Maximum Likelihood from Incomplete Data via the EM Algorithm*, Journal of the Royal Statistical Society, vol 39, pp. 1-38, 1977.

[2] L.A. Shepp and Y. Vardi, *Maximum Likelihood Reconstruction for Emission Tomography*, IEEE Transactions on Medical Imaging, vol. MI-1, No 2, Oct. 1982.

[3] H. H. Barrett et al., *List-mode Likelihood*, Journal of the American Optical Society, vol. 14, n. 11, Nov. 1997.

[4] L. Parra et el., *List-mode Likelihood: EM Algorithm and Image Quality Estimation Demonstrated on 2-D PET*, IEEE Transactions on Medical Imaging, vol. 17, n.2, Apr. 1998.

[5] K. Lange and R. Carson, *EM Reconstruction Algorithm for Emission and Transmission Tomography*, Journal of Computer Assisted Tomography, vol. 8, n. 2, pp. 306 – 316, 1984.

[6] L. Caucci, L. R. Furenlid, and H. H. Barrett, *Maximum Likelihood Event Estimation and List-mode Image Reconstruction on GPU Hardware*, Center for Gamma-Ray Imaging and College of Optical Sciences, University of Arizona, Tucson, Arizona, poster presentation.

[7] H. H. Barret, Center for Gamma-Ray Imaging and College of Optical Sciences, University of Arizona, Tucson, Arizona, private communications.

[8] M. Defrise, Vrije Universiteit Brussel, private communications.

CHAPTER IV

IMAGE RECONSTRUCTION RESULTS

4.1 INTRODUCTION

Estimates of radioactive source distributions produced by back-projection and list-mode maximum likelihood expectation maximization algorithms are presented in this chapter.

Two imaging systems are used: the first is the compact block type detector discussed in paragraph 1.3, which uses only one view of the object; the second is a spherical detector enclosing the complete field of view. As discussed, three-dimensional imaging is still possible in Compton imaging even when using a block type detector employing one view of the object. As shown in this chapter, image reconstruction along the direction perpendicular to the block type detector presents some complexity, due to geometrical considerations and some artifacts might appear along the dimension perpendicular to the detector face if not properly corrected. Hence, the impulse response is non-shift invariant under conditions provided by the block type imaging system if using one view of the object. This type of artifact is mitigated by the use of a spherical detector which has full 4 π view of the object. Images produced in two dimensions with the block type detector and in three dimensions with the spherical detector are presented.

Experimental and simulated gamma-ray interactions in the detection system are used for image formation and a comparison between images of simulated and experimental sources is made. The simulated interactions are representative of observables obtained with a detection system that has infinitely small accuracy and precision uncertainty. To the cones reconstructed from simulated interactions, errors are applied. These errors are estimates intended to represent the precision errors associated with a real imaging detector and errors due to the fact that the momentum of the orbital electron which undergoes scattering is unknown. No accuracy errors on the measured position of interaction and energy deposition, nor errors due to time resolution are applied to the simulated data. Differences between simulated and experimental images are thus intended to be due to accuracy errors, time resolution, any spurious detector and data acquisition process or background signal resulting in apparent interaction sequences. Images of simulated and experimental spherical sources are compared.

Resolution estimates are given as a function of angular error. Errors on scattering angle ranging from one degree to three degrees are applied to the cones. Errors of two and three degrees are estimated if the photons emitted by the source have energies in the order of 392 keV and 662 keV, and if gamma-ray interaction sequences are separated by a distance in the order of few centimeters or larger. The error decreases with increasing photon energy, and one degree is estimated for photons at energies in the order of 1 MeV when interaction sequences separated by a distance in the order of few centimeters are selected. Images of simulated line sources are presented in two-dimensions for the block type detector and in three dimensions for the spherical imaging system at a distance of few centimeters from the detector.

4.2 SIMULATED AND EXPERIMENTAL IMAGING SYSTEMS

4.2.1 EMISSION SOURCES AND OBSERVABLES

Experimental and simulated emission sources and imaging systems have been used to generate the observables needed for image reconstruction of the source. The simulated photon emission sources and photon interactions within the detection system have been generated by means of the Monte Carlo method and using the transport code Geant4 [1]. Routine for random creation of emission sites within defined source volumes has been created. An algorithm for isotropic emission of gamma-rays in 4 π has been developed and implemented into Geant4. Detector geometry and materials have been created in Geant4. The detector volume is not discretized, pixilated or binned, but continuous and can provide continuous position of interaction and energy deposition. The environment within which detectors and sources are contained is full of standard condition air. The gamma-rays have been transported within the experimental hall using the low-energy cross section library of Geant4 [2]. Energy deposition and position of interaction within the continuous detector volume have been recorded for each emitted gamma-ray. Routines for extraction and selection of interaction sequences according to desiderate parameters have been created. The selected outcome of the simulation is a list of continuous values associated with selected gamma-ray interaction sequences. The list is a sequence of position of interaction and energy deposition associated with each gamma-ray interaction sequence; the values follow a chronological order going from first to last interaction produced by the same emitted gamma-ray. A similar outcome is obtained for the parameters observed by the real detector system; also in this case position of interaction and energy deposition are estimated as continuous values, by applying analytical models to the voltage signals produced in the detector as discussed in paragraph 1.3. For the real detection system the chronology of the interactions produced by the same original gamma-ray is unknown because time resolution of the instrument does not allow discrimination. Chronology of interaction is inferred following the procedure discussed in paragraph 1.3. For the simulated interactions, the accuracy of the energy deposition, position and time of interaction is regarded as exact with no uncertainty. For the measurements all values are estimates and can be affected by errors due to precision and accuracy of the detection system and evaluation methodology, as discussed in paragraph 1.3. Errors due to precision of the detection system are characterized and applied to the simulated imaging parameters, as they are applied to the measured imaging parameters, following the procedures discussed in Chapter 2. Also, the error due to the uncertainty on the momentum of the orbital electron which collides with the gamma-ray is applied to the simulated data. Errors due to the accuracy of position of interaction, accuracy of energy deposition, and time resolution are not characterized nor quantified, and are not applied to the simulated imaging parameters. Thus the effects of accuracy of position of interaction, accuracy of energy deposition, and time resolution define the differences between the images of experimental and simulated data, along with any spurious detector and data acquisition process or background signal resulting in apparent interaction sequences.

The scattering angle has been computed both for simulated and measured gamma-ray interactions according to the Compton formula, by using energy deposition during the first interaction and photon energy before impact. The cone axis direction has been determined on the basis of the first and second position of interaction. The error on the scattering angle and cone axis direction has been computed by assuming the precision of the detection system discussed in paragraph 1.3.

4.2.2 SPHERICAL AND BLOCK TYPE IMAGING SYSTEM

Two detector models are used to produce the simulated gamma-ray sequences: one is the compact block type detector discussed in paragraph 1.3, also used to acquire the experimental data, the other is a spherical detector. A schematic lay-out is shown in Figure 1. For both detection systems, the first detector is made of silicon, the second is made of germanium. In the compact block type detector, the silicon detector has a rectangular cross section; the germanium detector has a regular octagonal cross section.

The spectrum of the cone aperture and angular error is presented for both the block type detector and the spherical detector in Figure 2 and Figure 3 respectively. The cones are reconstructed on the basis of simulated photon interactions. The simulation source is point like, emits photons at 392 keV, and it is located at 40mm from the detector, and aligned with the detector axis, for the block type detector, and it is located at the center of field of view for the spherical detector.

The cone angular aperture spectrum is shown in Figure 2. The spectrum is a result of the Klein-Nishina probability of a photon of given energy to undergo scattering at a certain angle, combined with effects produced by the geometry of the imaging system and event selection criteria. Event selection criteria might be used to select cones with relatively small error. For example, the spectrum shown in Figure 2 a), related to the block type detector, does not contain cones larger than a certain threshold because only events having a first interaction in the silicon detector and the second interaction in the germanium detector are selected. Thus upper threshold for the cone aperture is determined by the geometry of the imaging system and interaction sequence selection criteria. The spectrum shown in Figure 2. b) is produced using all interaction sequences, thus also events that have first and second interaction in the same detection element are used. In this case cones with aperture up to 180 degrees are produced. Also the spectrum produced by the spherical detector contains cone aperture up to 180 degrees. In this case events having a first interaction in the silicon detector and the second interaction in the germanium detector are selected.

Out of the cone aperture spectrum shown in Figure 2, cones with aperture larger than a certain threshold are selected for image reconstruction. The threshold is based on the minimum energy deposition applied to the data acquisition trigger; the threshold is used to avoid triggering on spurious events. The value corresponds to a cone aperture of about 20 degrees.

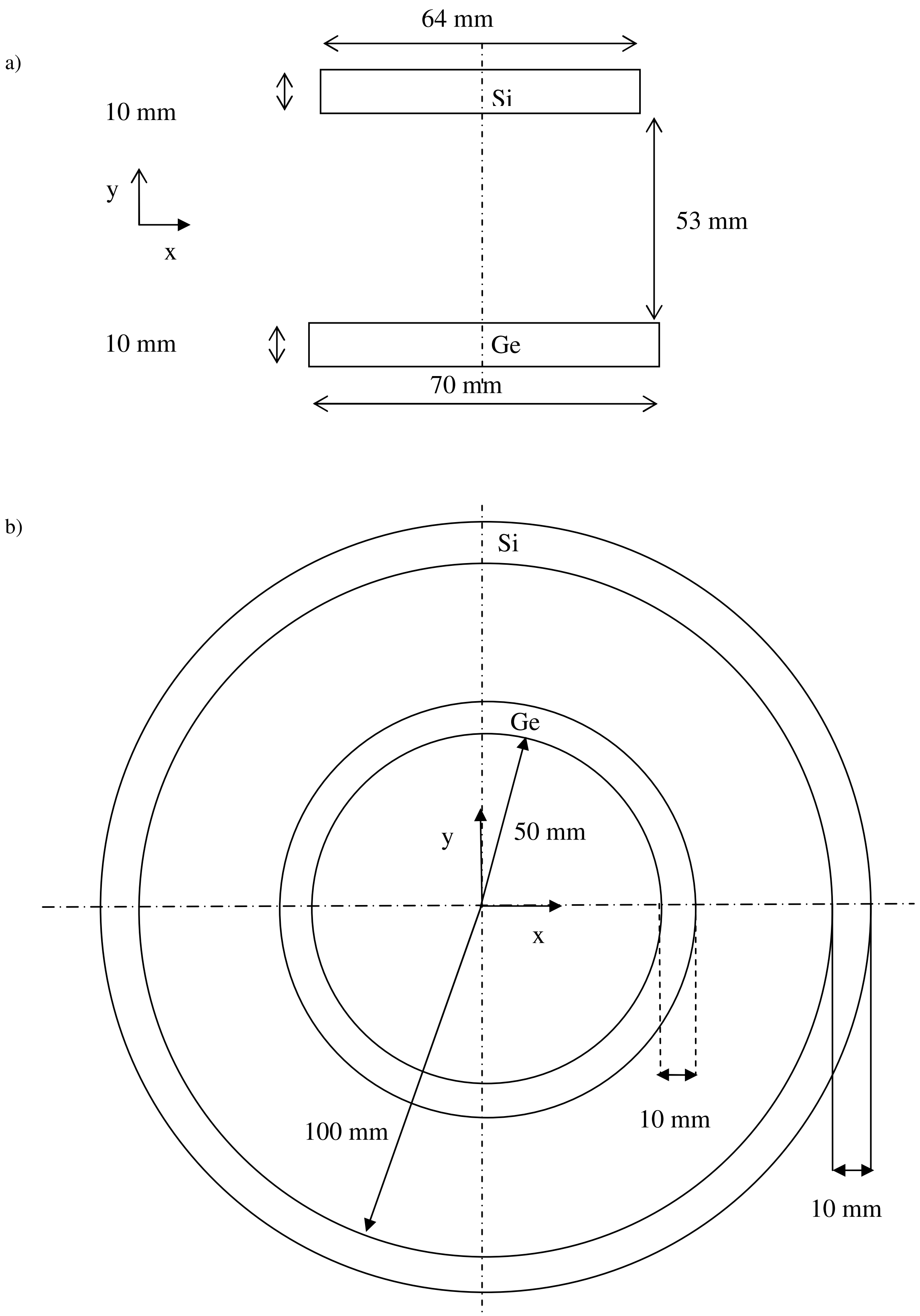

Fig. 1. Detector models; cross section of: a) compact block type detector; b) spherical detector.

The angular error associated with each cone has been computed according to the methodology discussed in Chapter 2. As mentioned, the error is representative of precision errors on the energy deposition and position of interaction of the photon in the detection system, and it is representative of the systematic errors due to the fact that it is not possible to establish the momentum of the orbital electron that undergoes collision. The error histogram is shown in Figure 3 for cones produced by the block type imaging system and the spherical imaging system.

a)

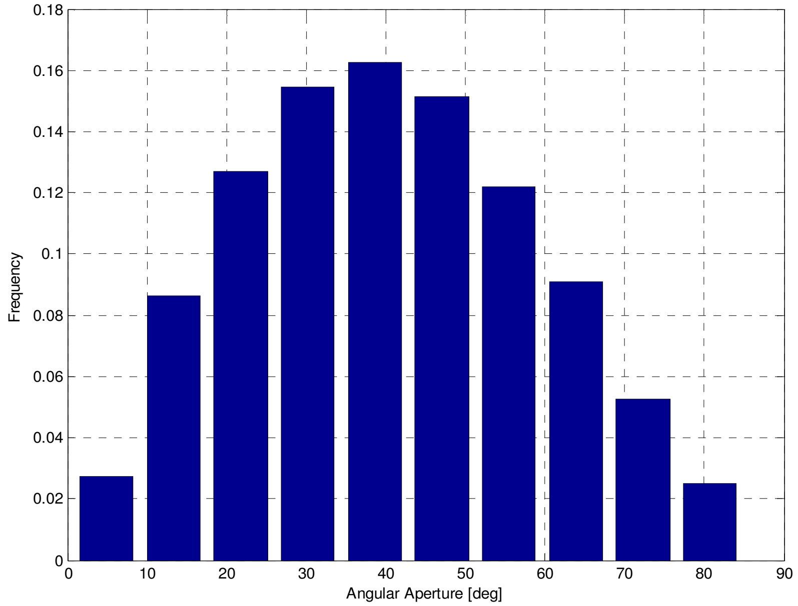

b)

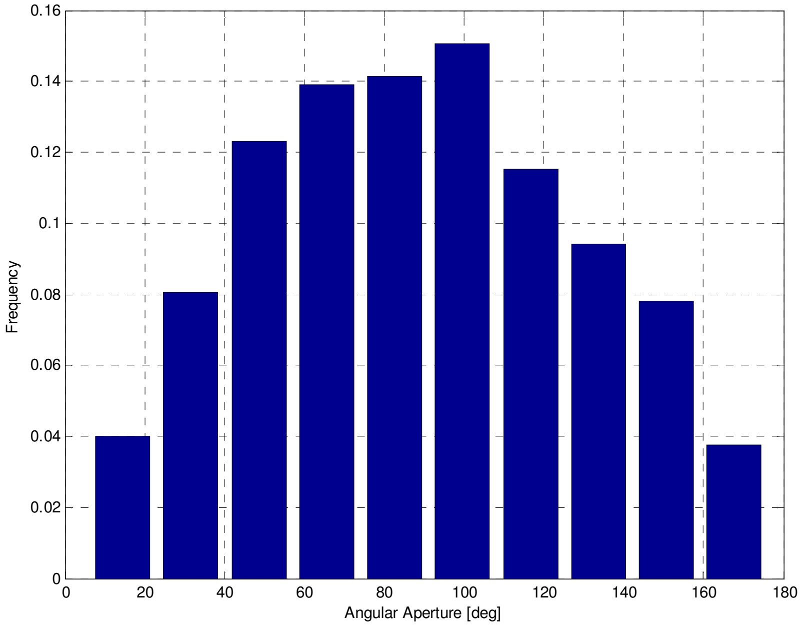

c)

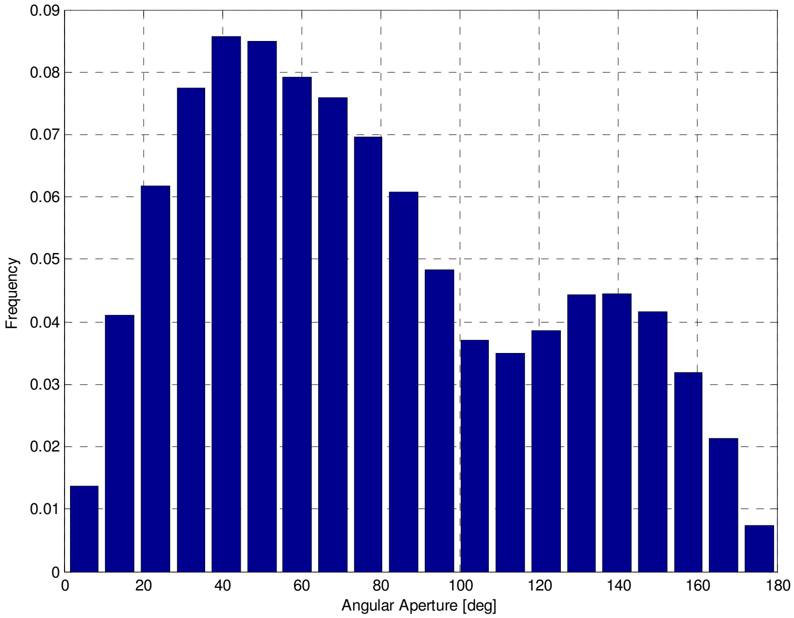

Fig. 2. Histogram of angular aperture of cones produced by a 392 keV point-like source for: a) the block type detector and source located at 40 mm from the detector and aligned with the detector axis, when using events having first interaction in first detector and second interaction in second detector; b) the block type detector and source located at 40 mm from the detector and aligned with the detector axis, when using all multiple interaction sequences; c) the spherical detector and source located at the center, when using events having first interaction in first detector and second interaction in second detector. Gamma-ray interaction sequences that deposit all photon energy in the detector are used to produce the cones in all cases.

a)

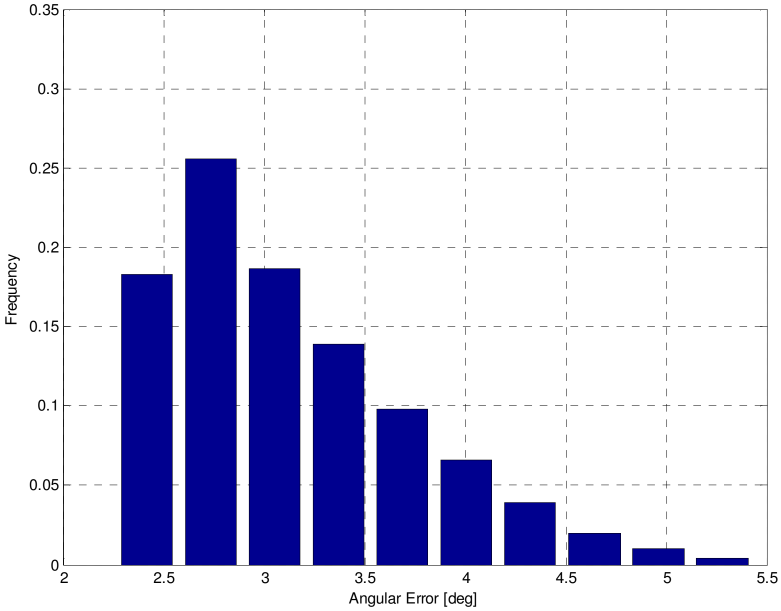

b)

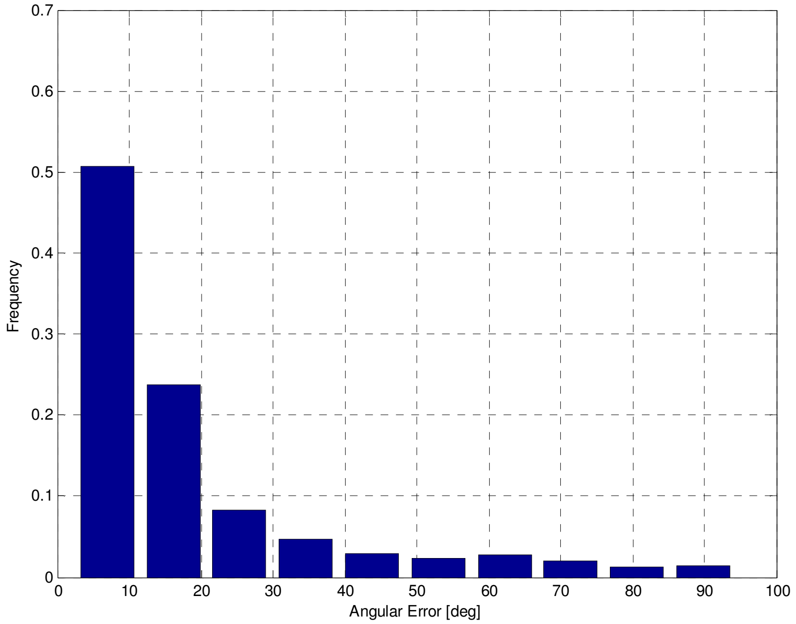
0.7
0.6
0.5
0.4
0.3
0.2
0.1
0
Frequency
0
10
20
30
40
50
60
70
80
90
100
Angular Error [deg]

c)

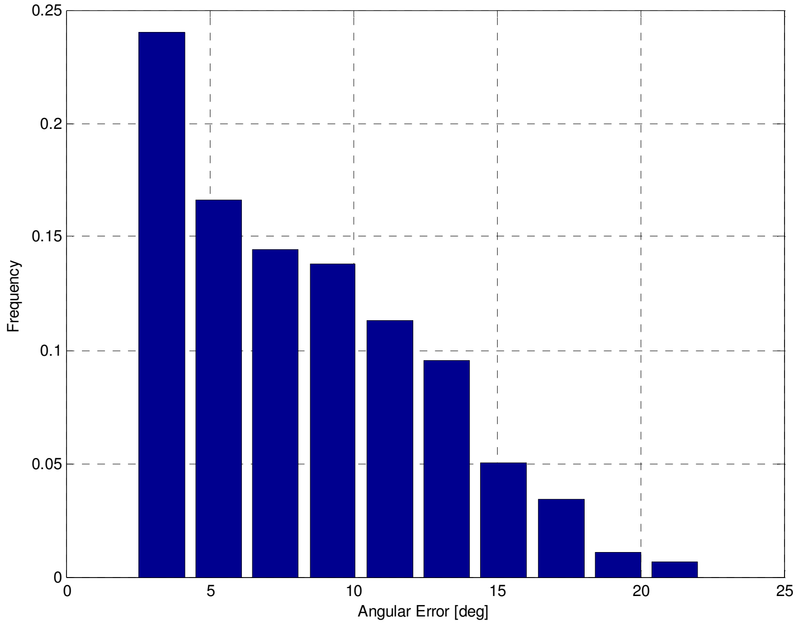
0.25
0.2
0.15
0.1
0.05
0
Frequency
0
5
10
15
20
25
Angular Error [deg]

d)

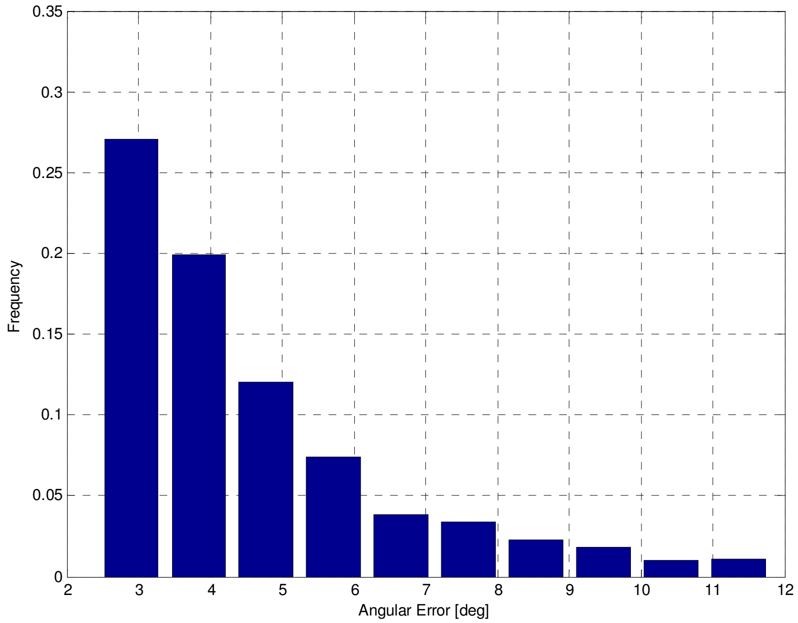

Fig. 3. Histogram of uncertainty on angular aperture of cones produced by a 392 keV point-like source for: a) the block type detector and source located at 40 mm from the detector and aligned with the detector axis, when using events having first interaction in first detector and second interaction in second detector; b) the block type detector and source located at 40 mm from the detector and aligned with the detector axis when using all multiple interaction sequences; c) the block type detector and source located at 40 mm from the detector and aligned with the detector axis, when using all events which have first and second interaction separated by distances larger than 5 mm; d) the spherical detector and source located at the center, when using events having first interaction in first detector and second interaction in second detector. Gamma-ray interaction sequences that deposit all photon energy in the detector are used to produce the cones in all cases. Only errors associated to cones with aperture larger than 20 degrees are presented in all cases.

As shown in Figure 3.a), cones produced using the block type detector when only events that have first and second interaction in separate detectors are used, have relatively small errors, with a mean value around 3 degrees at a distance of 40 mm from the detector. Also variation among errors is relatively small, going from about 2 degrees to 5 degrees. As shown in Figure 3. b), when all multiple interaction sequences are used, including these having first and second interaction occurring in the same detection element, the error becomes larger, with variations from a few degrees to 90 degrees. However, about 50% of the sequences, in this case, result in errors below 10 degrees. Selecting events that have first and second interaction separated by a distance larger than 5 mm produces the error spectrum shown in Figure 3. c). In this case the maximum error is about 20 degrees.

The error histogram for the spherical imaging system in shown in Figure 3. d), when using events that have first and second interaction in separate detector. In this case larger errors are obtained than in the corresponding case using the block type detector, because cones of larger aperture are produced, and the error due to the fact that it is not possible to establish the momentum of the orbital electron is larger for larger scattering angles. About 50% of the cones have error smaller than 5 degrees.

On the basis of the error estimate shown in Figure 3, gamma-ray interaction sequences that have first and second interactions in separate detection elements, shall be preferred for image reconstruction because they carry smaller errors.

4.3 IMAGE RECONSTRUCTION OF SIMULATED POINT-LIKE SOURCES

In order to characterize the impulse response of the imaging system, image reconstruction of point-like sources at three different positions within the field of view has been performed by means of simple backprojection. The number of cones used for reconstruction is 5000 for each point-like-source. The intensity of each voxel with respect to each cone is estimated by integrating the probability density function that a photon is emitted from a certain position in space over the voxel volume, according to the methodology discussed in paragraph 3.2. Two distinct probability density functions are used: a Lorentz distribution which is a function of minimum angular distance from cone surface; a Lorentz distribution which is a function of the minimum linear distance from the cone surface. The probability density function that depends on angular distance is derived according to physical models describing the angular uncertainty affecting scattering angle. The reason for using a probability density function that depends on linear distance is only included to show differences in image reconstruction between the two approaches. Two different angular errors, $\delta\theta$, are used: 3 degrees and 10 degrees. The corresponding linear error, δL, is computed at a fixed distance, d, of 40 mm from the detector as:

$$\delta L = d\tan(\delta\theta) \tag{4.1}$$

For the block-type system the point sources are placed at three different locations, all at the same axial distance from the detector, one at the center, the other two at symmetric locations around the axis of the system. For the spherical system the three sources are placed at the center of the sphere, and at symmetric locations along a direction passing through the center of the imaging system. The field of view is discretized into cubical voxels with 1mm in side. Images of impulse response are shown from Figure 4 to Figure 8 for the block type imaging system and from Figure 9 to Figure 13 for the spherical imaging system.

4.3.1 RESULTS FOR THE BLOCK TYPE IMAGING SYSTEM

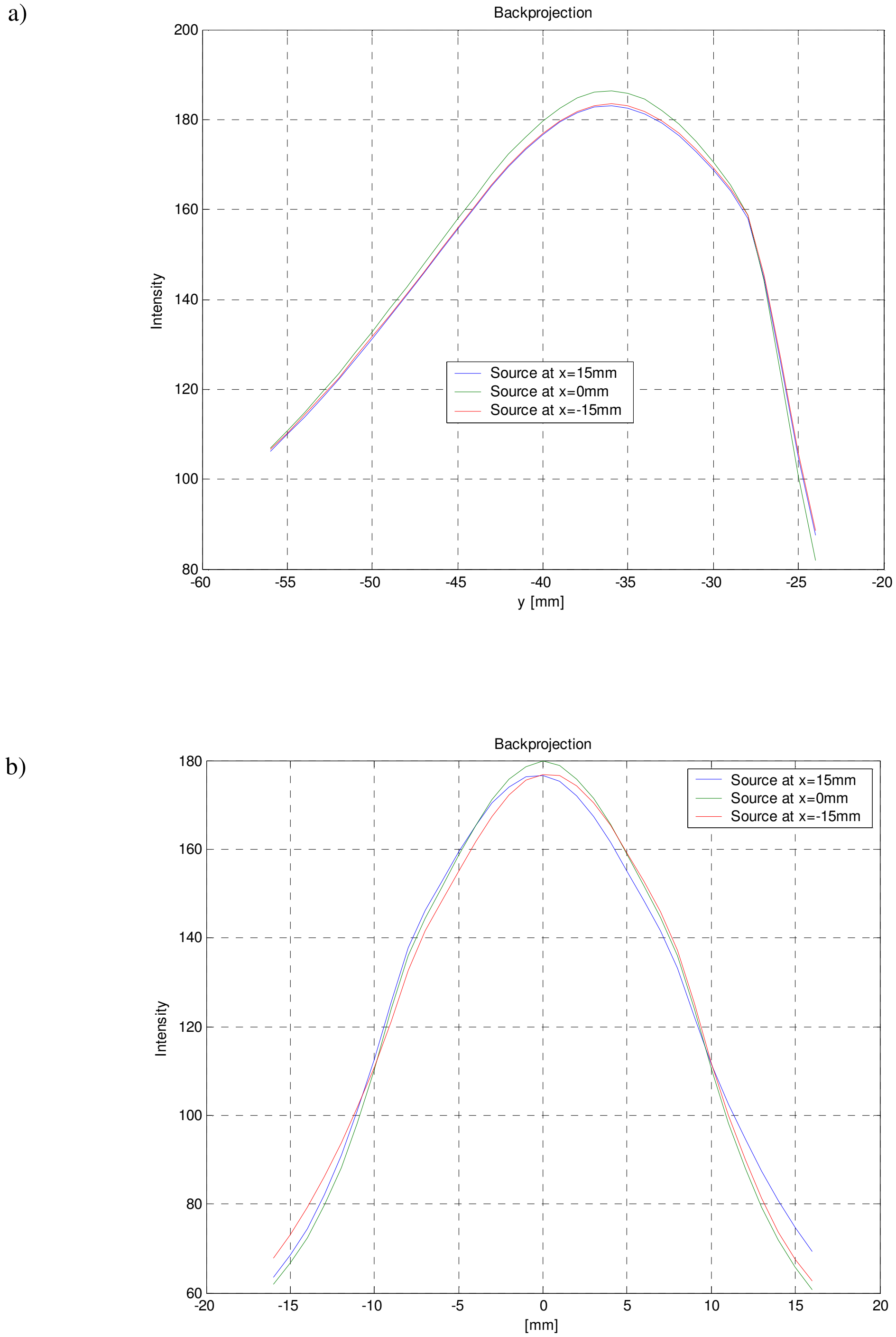

Fig. 4. Image of a point-like source located at a distance y=40 mm from the detector, and x=0 mm, x=15 mm, x=-15 mm. Error on scattering angle is 10 deg. The probability density function describing angular aperture error is based on angular distance from cone surface. a) Profile along y direction; b) Profile along x direction; The profile of the source object located at x=15 mm and x=-15 mm are translated of -15 mm and +15 mm along x axis respectively.

a)

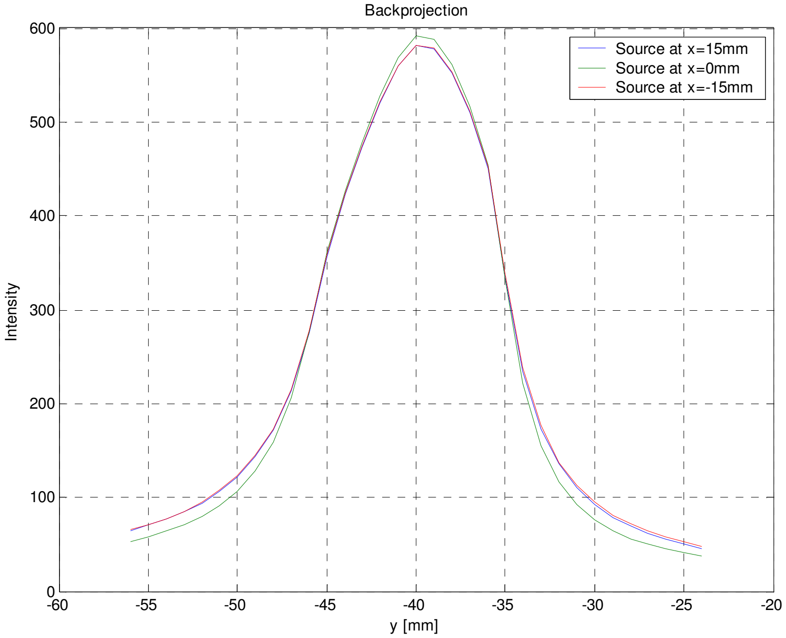

b)

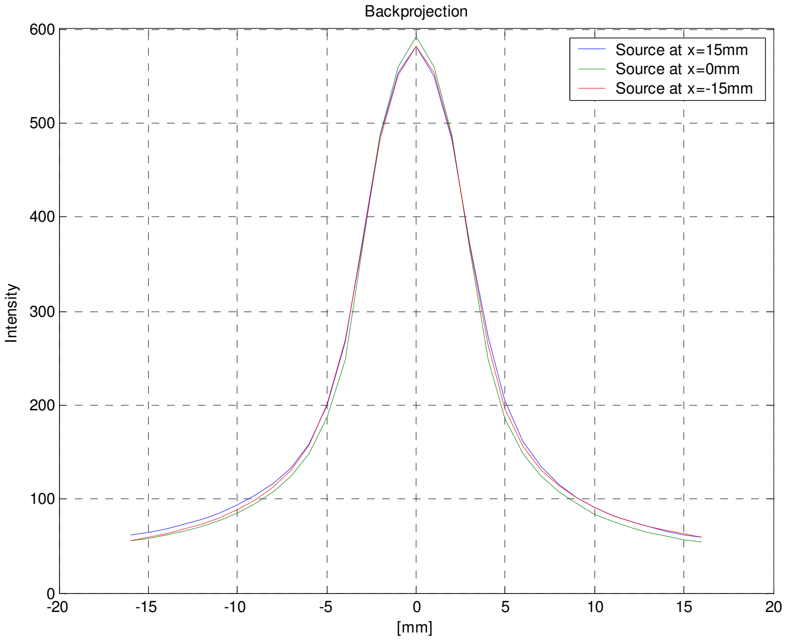

Fig. 5. Image of a point-like source located at a distance y=40 mm from the detector, and x=0 mm, x=15 mm, x=-15 mm. Error on scattering angle is 3 deg. The probability density function describing angular aperture error is based on angular distance from cone surface. a) Profile along y direction; b) Profile along x direction; The profile of the source object located at x=15 mm and x=-15 mm are translated of -15 mm and +15 mm along x axis respectively.

a)

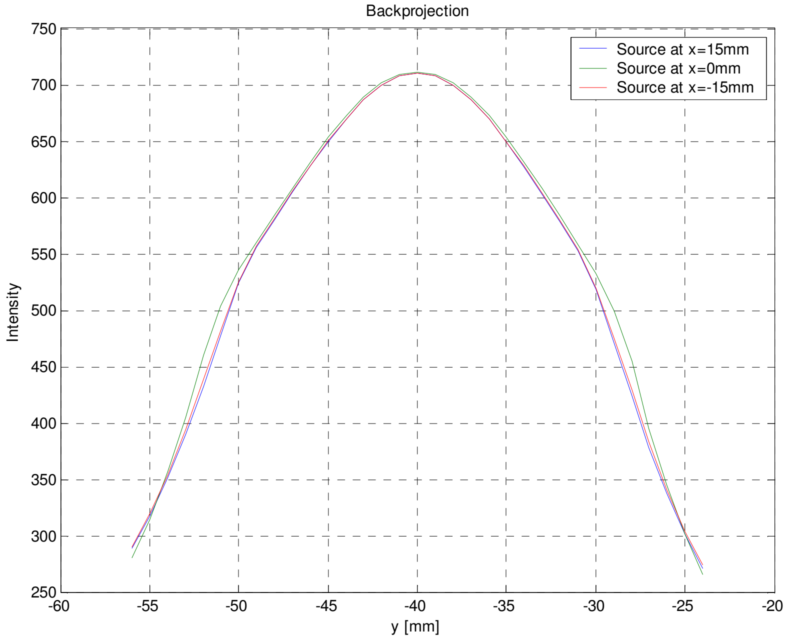

b)

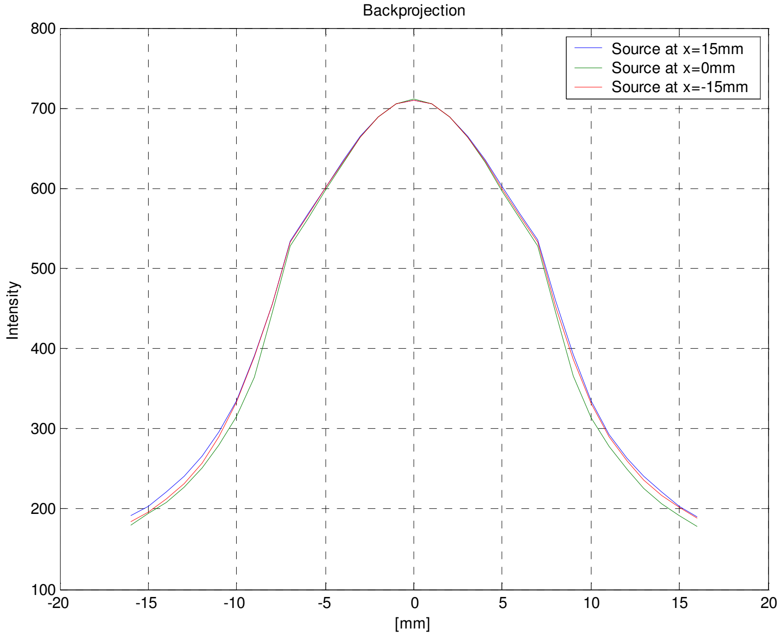

Fig. 6. Image of a point-like source located at a distance y=40 mm from the detector, and x=0 mm, x=15 mm, x=-15 mm. Error on scattering angle is 10 deg. The probability density function describing angular aperture error is based on linear distance from cone surface. a) Profile along y direction; b) Profile along x direction; The profile of the source object located at x=15 mm and x=-15 mm are translated of -15 mm and +15 mm along x axis respectively.

a)

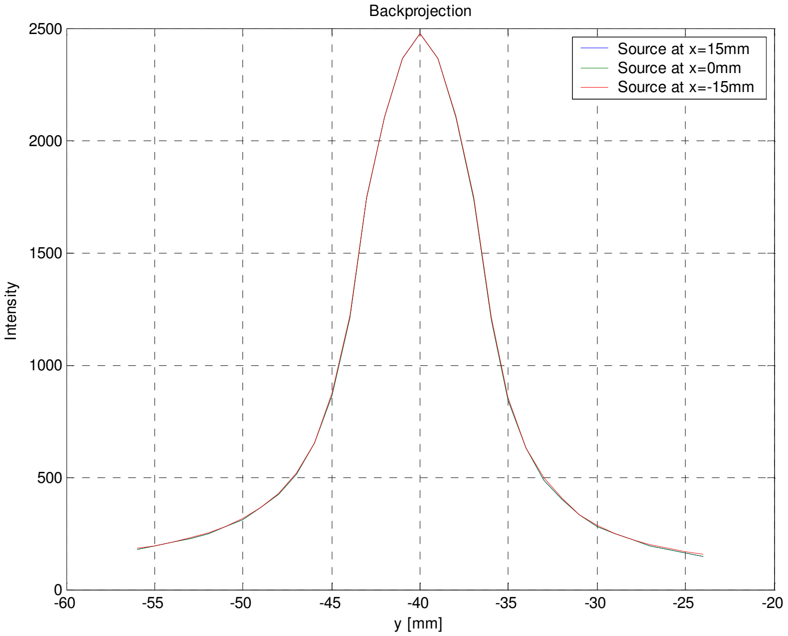

b)

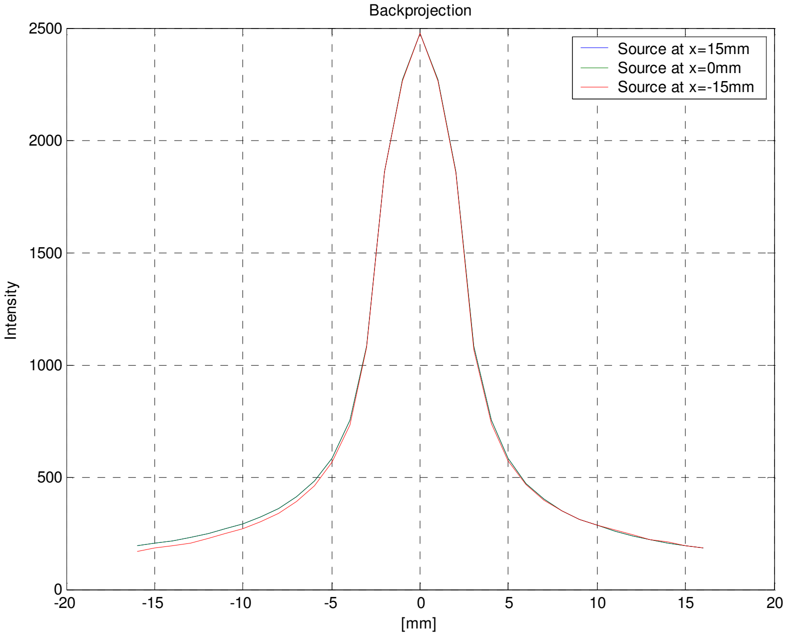

Fig. 7. Image of a point-like source located at a distance y=40 mm from the detector, and x=0 mm, x=15 mm, x=-15 mm. Error on scattering angle is 3 deg. The probability density function describing angular aperture error is based on linear distance from cone surface. a) Profile along y direction; b) Profile along x direction; The profile of the source object located at x=15 mm and x=-15 mm are translated of -15 mm and +15 mm along x axis respectively.

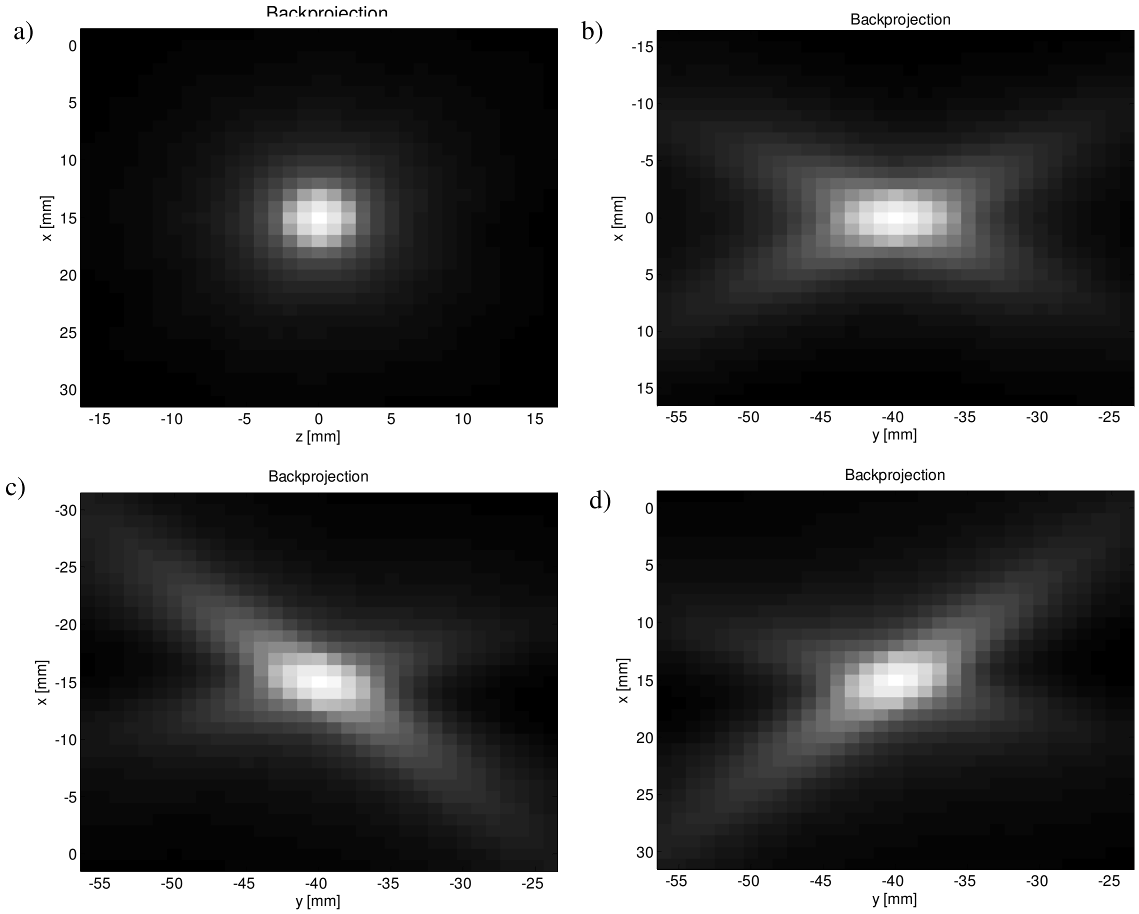

Fig. 8. Two-dimensional images of point-like source. Error on scattering angle is 3 deg. Probability density function describing angular aperture error is based on linear distance from cone surface. a) Image along x-z plane of point source located at x=15 mm from center; b) Image along x-y plane of point source located at the center; c) Image along x-y plane of point source located x=-15 mm from center; d) Image along x-y plane of point source located at x=15 mm from center.

4.3.2 RESULTS FOR THE SPHERICAL IMAGING SYSTEM

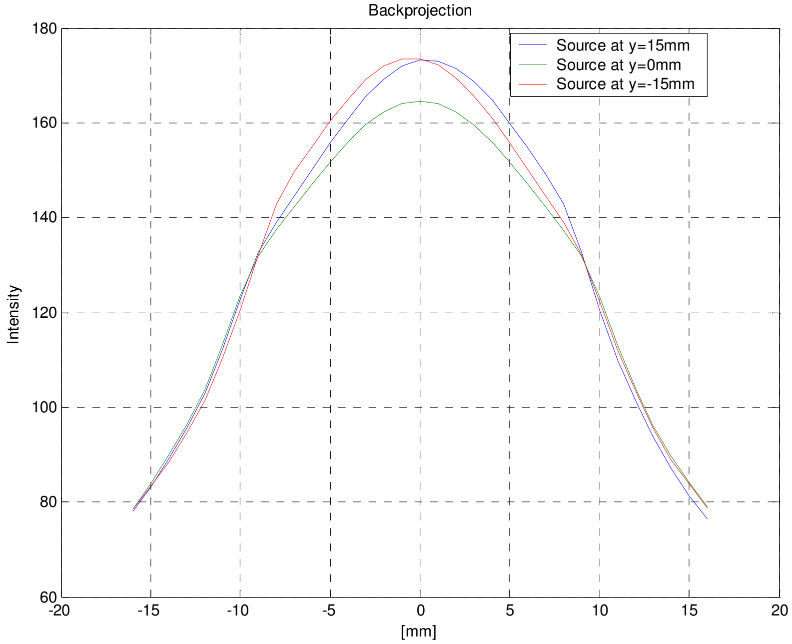

Fig. 9. Image of point-like source located at a distance of y=0 mm, y=15 mm, y=-15 mm from the center of the spherical imaging system. The curves of the source object located at y=15 mm and y=-15 mm are translated -15 mm and +15 mm along y axis respectively. Error on scattering angle is 10 deg. Probability density function describing angular aperture error is based on angular distance from cone surface.

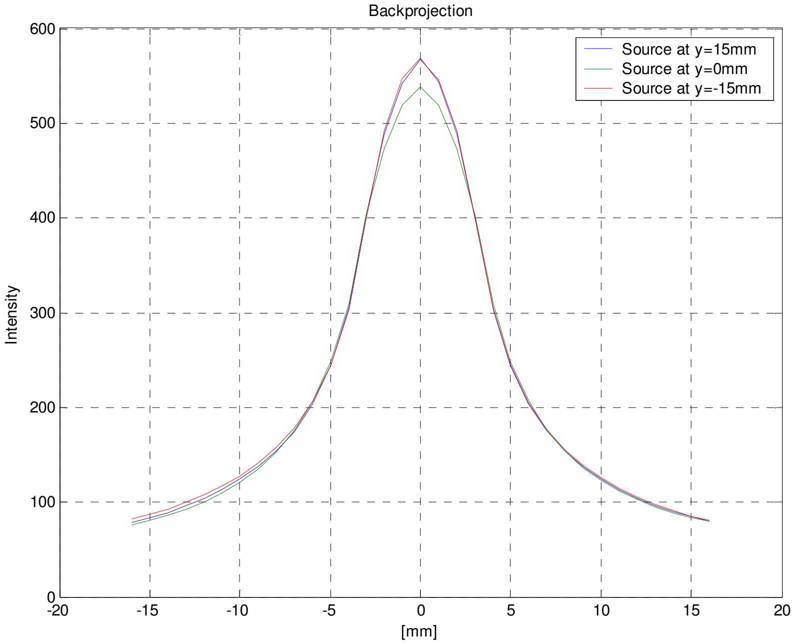

Fig. 10. Image of point-like source located at a distance of y=0 mm, y=15 mm, y=-15 mm from the center of the spherical imaging system. The curves of the source object located at y=15 mm and y=-15 mm are translated of -15 mm and +15 mm along y axis respectively. Error on scattering angle is: 3 deg. Probability density function describing angular aperture error is based on angular distance from cone surface.

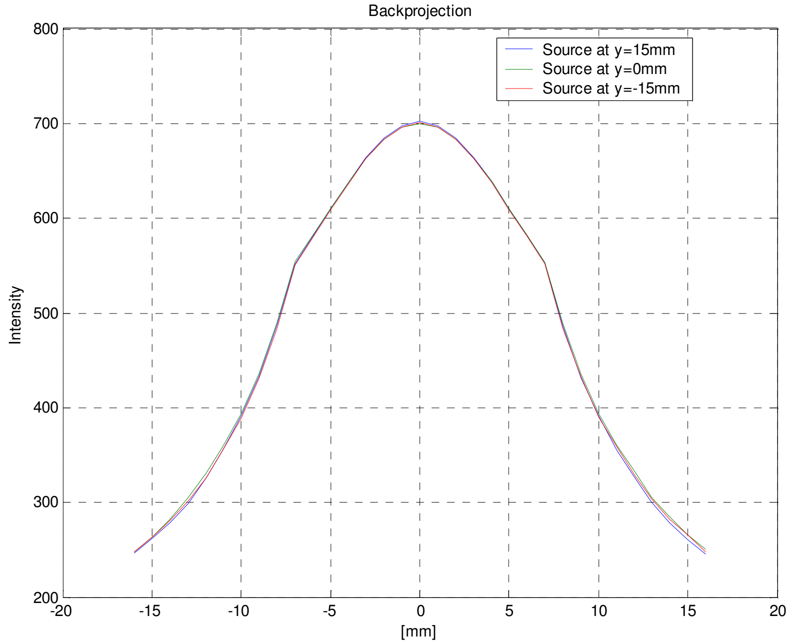

Fig. 11. Image of point-like source located at a distance of y=0 mm, y=15 mm, y=-15 mm from the center of the spherical imaging system. The curves of the source object located at y=15mm and y=-15mm are translated of -15 mm and +15 mm along y axis. Error on scattering angle is: 10 deg. Probability density function describing angular aperture error is based on linear distance from cone surface.

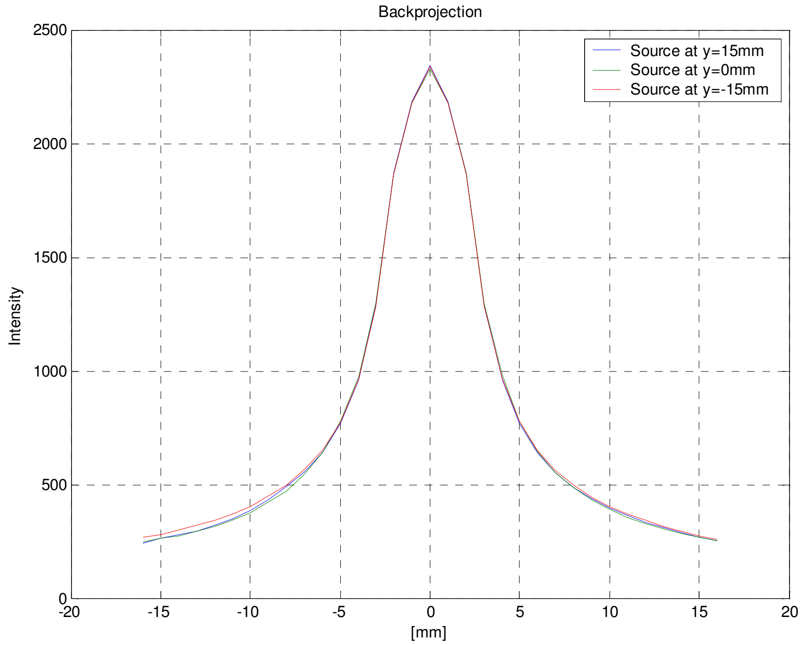

Fig. 12. Image of point-like source located at a distance of y=0 mm, y=15 mm, y=-15 mm from the center of the spherical imaging system. The curves of the source object located at y=15 mm and y=-15 mm are translated of -15 mm and +15 mm along y axis respectively. Error on scattering angle is: 3 deg. Probability density function describing angular aperture error is based on linear distance from cone surface.

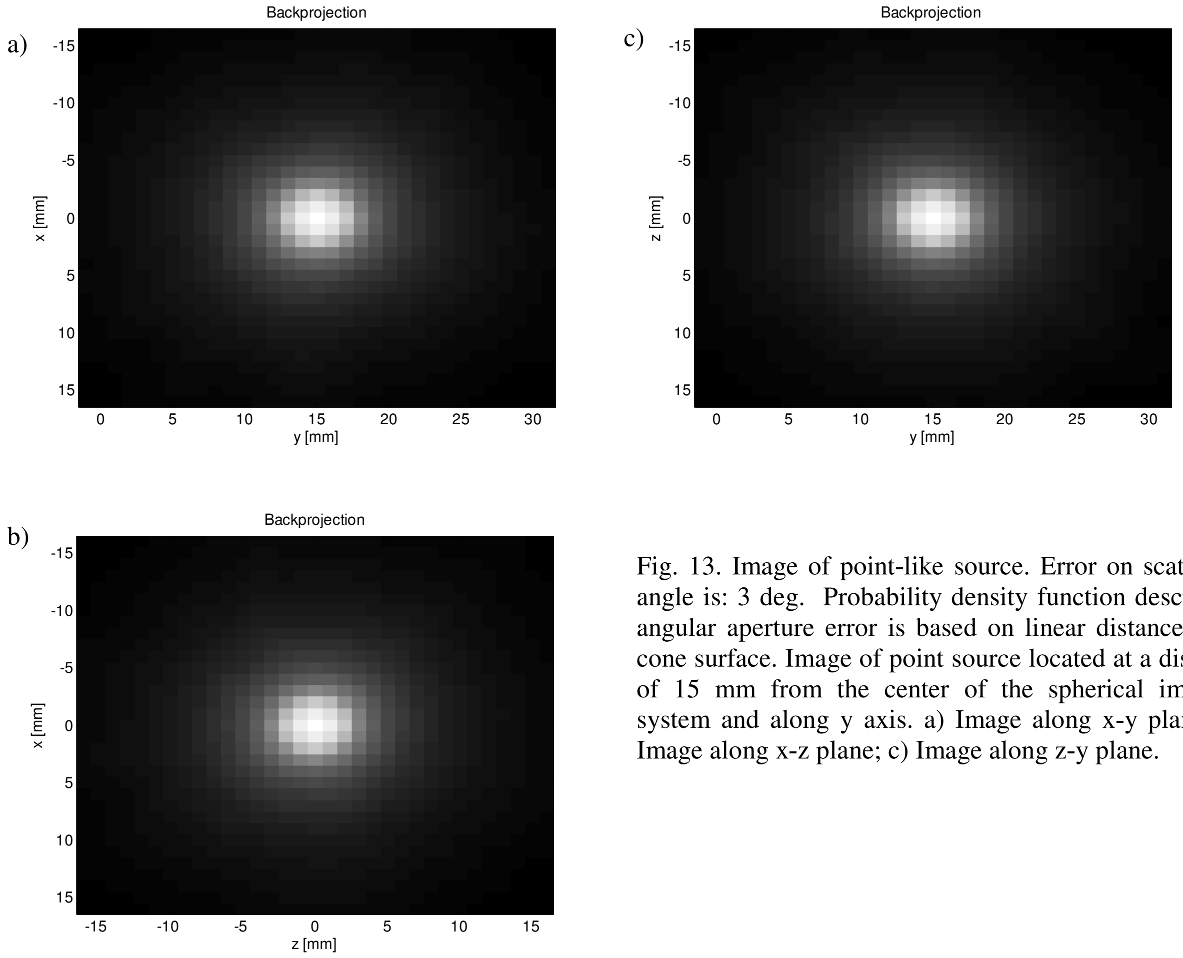

Fig. 13. Image of point-like source. Error on scattering angle is: 3 deg. Probability density function describing angular aperture error is based on linear distance from cone surface. Image of point source located at a distance of 15 mm from the center of the spherical imaging system and along y axis. a) Image along x-y plane; b) Image along x-z plane; c) Image along z-y plane.

4.3.3 DISCUSSION

The one-dimensional profiles of the impulse response of the block type detector are shown from Figure 4 to Figure 7, and from Figure 9 to Figure 12 for the spherical detection system, for sources at different locations on the field of view. For the block type system, both profiles, the one along the direction parallel to the detector face and the one perpendicular to it are shown. For the spherical system, the profile along the direction passing through the source and the detector center is shown.

As shown in Figure 4, Figure 5, Figure 9 and Figure 10, when using a probability density function that depends on angular distance, the impulse response is shifted or misplaced with respect to the object and the shape depends on object location, both for the block type detector imaging system and for the spherical detector system. Misplacement and absolute and relative differences of the point spread function profile increase with angular error. For the block type imaging system at an angular error of 3 degrees the misplacement is less than 1 mm along the y direction; for an angular error of 10 degrees, the misplacement along the y direction is about 4 mm. The fact that misplacement and differences of impulse response depend on position of point-like object and on angular error might cause artifacts, particularly when performing reconstruction of distributed objects. Non shift-invariance of the impulse response in Compton imaging might be generally caused by both the dependence of the histogram of cone axis direction and aperture on object location and by the angular nature of the error. As shown in Figure 6, Figure 7, Figure 11, and Figure 12, no misplacement seems to occur when using a probability density function that depends on linear distance. Use of a probability density function that depends on the angular distance of a point in field of view from the cone surface, is thus shown to be the major cause for object location misplacement. The object is misplaced more significantly for the block type system and along the direction perpendicular to the detector face, as shown in Figure 4.a) and Figure 5.a). Source misplacement however occurs also along the plane parallel to the block type detector face and along the radius of the spherical detector, although in a smaller amount. As shown in Figure 4.b), Figure 5.b), Figure 8, and Figure 9, it becomes noticeable for large angular errors. The object to the right is shifted to the left, and the object to the left is shifted to the right. No misplacement occurs if the object is placed at the center of field of view, except along the direction perpendicular to the block type detector face, both for the spherical detector and the block type detector. This is believed to be due to symmetry, around the detector axis, of the cone spectrum in terms of axis direction.

As mentioned, the misplacement is relatively not significant if using a probability density function that depends on linear distance, both for the spherical detector system and for the block type detector system. Also, dependence of the profile of the point spread function on location in field of view becomes almost negligible, except for the direction perpendicular to the block type detector. Two-dimensional profiles are shown in Figure 8 for the block type detector and in Figure 13 for the spherical detector. As shown in Figure 8 b), c), and d), the profile along the direction perpendicular to the block type detector depends on source position. This behavior might be caused by the dependence of the histogram of cone axis direction on object position.

As a general observation, differences in impulse response discussed herein, are geometrical and not related to the dependence of detection efficiency on source location. Detection efficiency is described by mathematical expressions related to physical phenomena, an exponential law for attenuation and a more complex expression for geometric efficiency. If the source misplacement was due to detection efficiency, misplacement would occur even when using a probability density function that depends on linear distance between a point and the cone. Since the misplacement and differences in impulse response are due purely to a geometric effect, eventual criterion employable for correcting these phenomena should be mathematical and geometrical. The observations discussed in this paragraph apply also if a line, or a sector of cone, could be identified, as opposed to a full cone.

Linearization of angular errors and use of a spherical imaging system are shown to significantly mitigate dependence of impulse response on object position, other than for causes due to detection efficiency variations across field of view. Linearization of angular errors when using the block type imaging system are shown to mitigate dependence of impulse response on object position along the plane parallel to the detector face, but not along other planes.

4.4 ON IMAGE RESOLUTION

Image reconstruction of point-like objects has been performed by means of simple back-projection and maximum likelihood expectation maximization algorithm with the purpose of estimating the resolution of the imaging system. Estimates are given using the block-type imaging system at a distance of 40 mm from the detector. Reconstruction has been performed using a fixed number of events, 10000 for each point-like source. Fixed angular errors have been applied to all cones with the intent of providing resolution estimates as a function of the angular error, and in turn gamma-ray energy, detector precision and distance between first and second interaction. The correspondence between angular error, gamma-ray energy, distance between first and second interaction and detector precision is shown in Chapter 2. The following angular errors are used: 1 degree, 2 degrees, 3 degrees. The intensity of each voxel with respect to a particular cone is determined by integrating the probability density function that depends on linear distance between a point and the cone surface, over the voxel volume. Two dimensional imaging has been performed by restricting the field of view to a unique slice 1mm thick encompassing the point-like object. The field of view is discretized into 1 mm side square pixels. The number of iterations used for image reconstruction via maximum likelihood has been chosen arbitrarily. It is generally accepted [3] that the number of iterations needed for convergence of the image depends often on several parameters. The educated guess used as criteria for this analysis is based on experience. Experience gathered on reconstruction of distributed sources suggests that the more iterations, the larger the deviations between the intensities of voxels containing the same activity becomes. It is not within the scope of this analysis to characterize image convergence through a systematic analysis. 30 iteration cycles are applied to all of the following images. Results are shown from Figure 14 to Figure 16 for two point like sources located at 2 mm and 4 mm distance and angular error of 1 degree, 2 degrees, and 3 degrees respectively, and in Figure 17 and 18 for 3 degrees error and the angular error spectrum shown in Figure 3 a) for two point like sources separated by 6 mm distance.

The images shown in the figures illustrate that when the two point-like objects are distinguishable using the backprojection image reconstruction methodology, they are also distinguishable when the maximum likelihood expectation maximization algorithm is used. When the objects are not distinguishable in backprojection, they can not be distinguished using the maximum likelihood expectation maximization algorithm.

It is not the scope of this analysis to derive a semi-empirical or theoretical relationship between the full width half maximum of the impulse response and the angular error affecting the cone aperture, however it seems that the full width at half maximum is proportional to the distance of the object from the detector multiplied by the tangent of the error. As shown in Figure 15, a 1 degree error allows distinguishing two point sources separated by 2 mm distance, and placed at 40 mm distance from the detector, while a 2degree error allows distinguishing two point sources separated by 4 mm distance. A 2 degrees error is the average error due to the lack of knowledge of the momentum of the orbital electron that undergoes collision with the photon at gamma-ray energy of 662 keV, and due to the precision of the detection system when interactions having first scattering in the first detector and second scattering in the second detector are used. Increasing the gamma-ray energy, the error decreases. As shown in Figure 17 and Figure 18, a typical error spectrum obtained for photons at 392 keV, shown in Figure 3.a), allows distinguishing two point sources separated by 6 mm and placed at 40 mm from the detector, but does not allow distinguishing two point sources separated by 4 mm.

It is also noted that when the two point sources, of activity in ratio of 1:1, are distinguishable, their intensity is reproduced with a ratio close to 1:1 after 30 iterations of the maximum likelihood expectation maximization algorithm.

a)

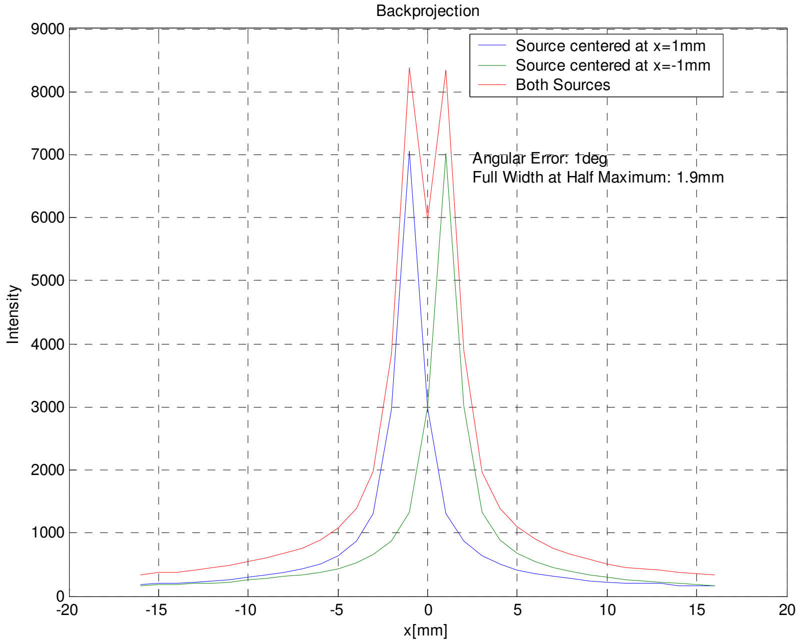

b)

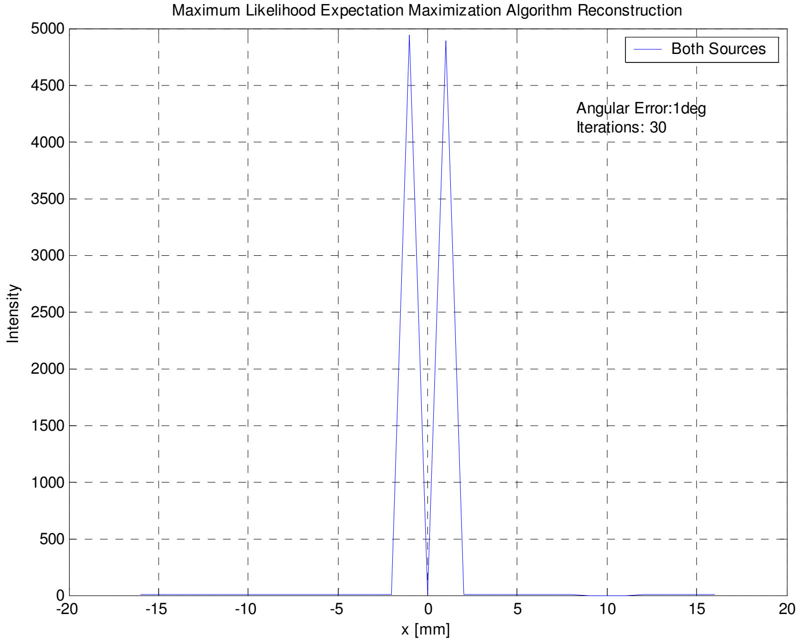

Fig. 14. Image reconstruction of simulated data of a point-like source at 40 mm from the detector and at a distance x=1 and x=-1 mm from detector center, along the direction parallel to the detector face. Error associated to scattering angle: 1 deg for all cones. a) Backprojection; b) Maximum likelihood expectation maximization algorithm reconstruction.

a)

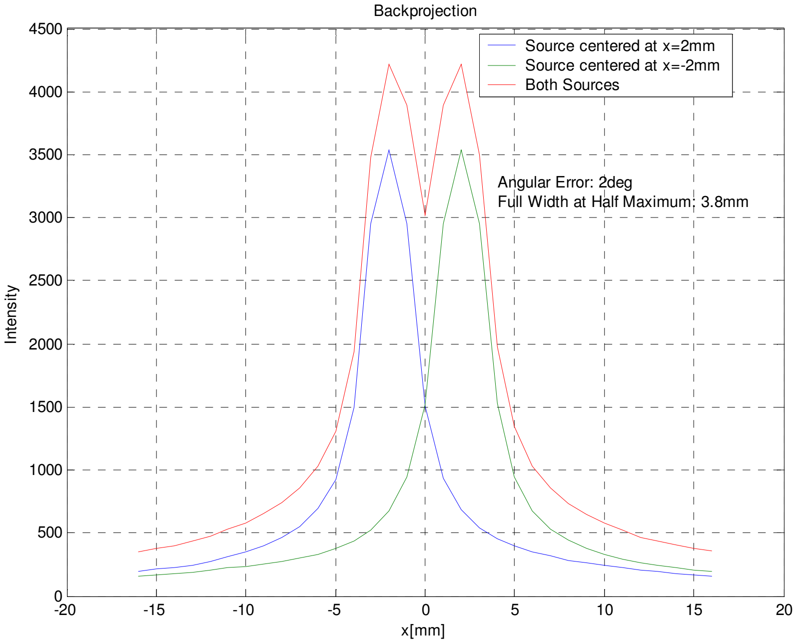

b)

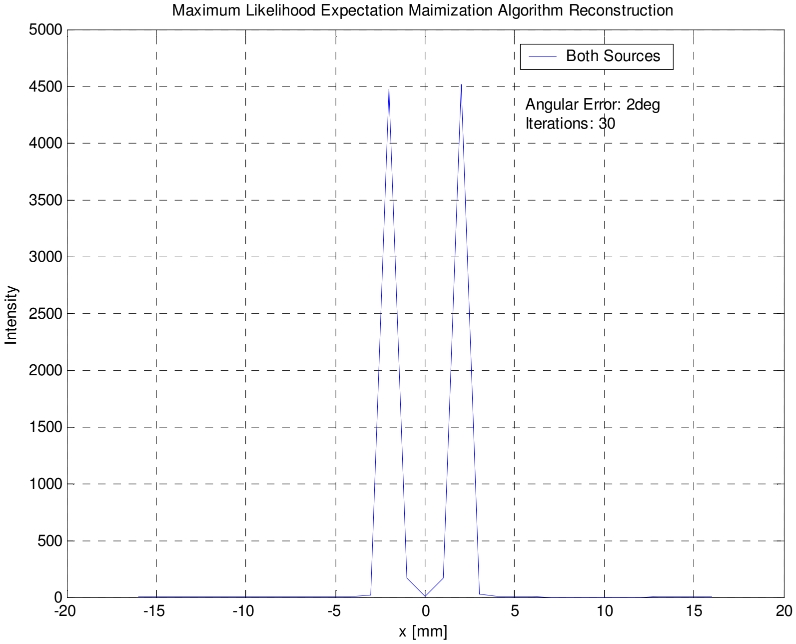

Fig. 15. Image reconstruction of simulated data of a point-like source at 40 mm from the detector and at a distance x=2 and x=-2 mm from detector center, along the direction parallel to the detector face. Error associated to scattering angle: 2 deg for all cones. a) Backprojection; b) Maximum likelihood expectation maximization algorithm reconstruction.

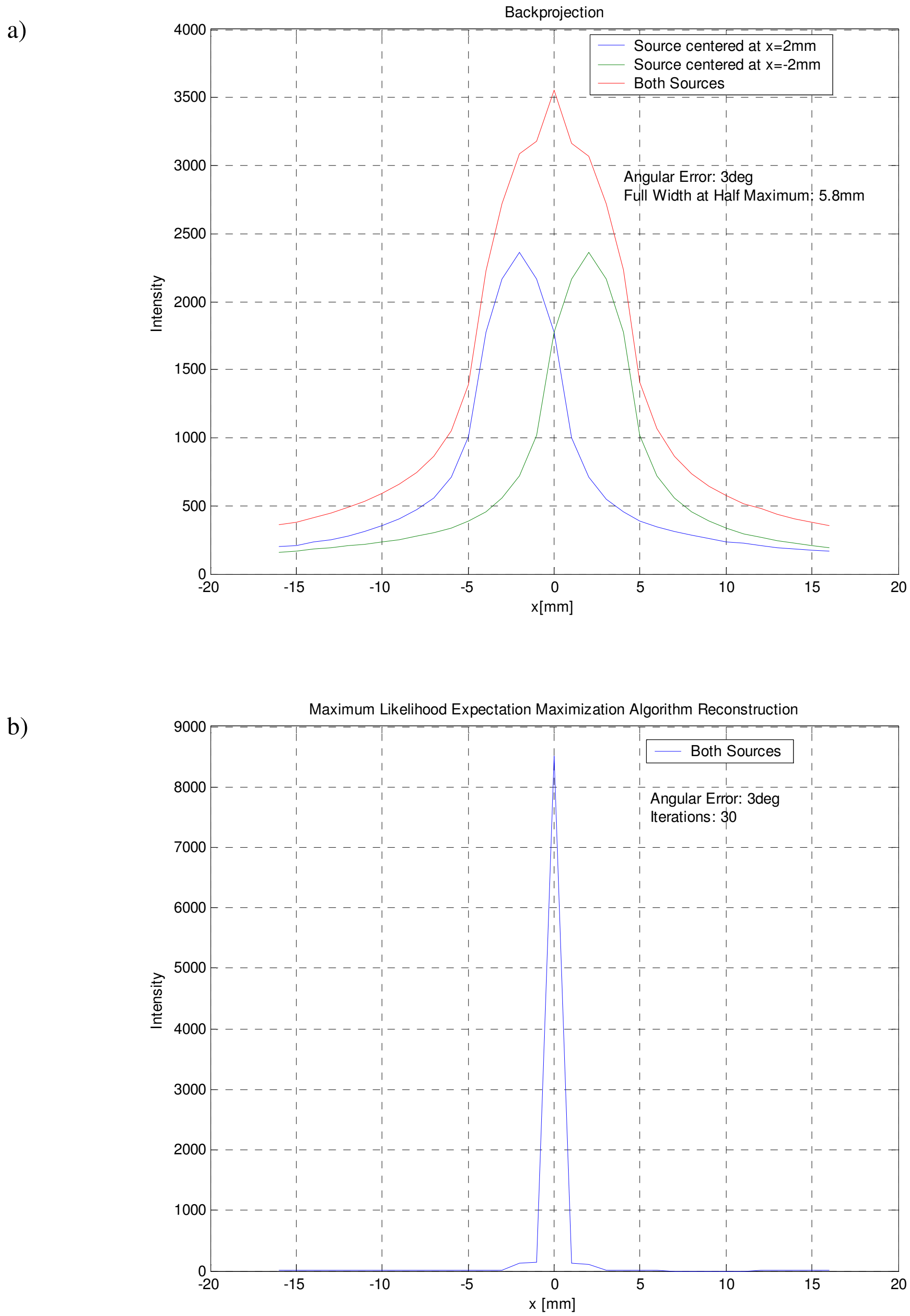

Fig. 16. Image reconstruction of simulated data of a point-like source at 40 mm from the detector and at 2 and -2 mm from detector center, along the direction parallel to the detector face. Error associated to scattering angle: 3 deg for all cones. a) Backprojection; b) Maximum likelihood expectation maximization algorithm reconstruction.

a)

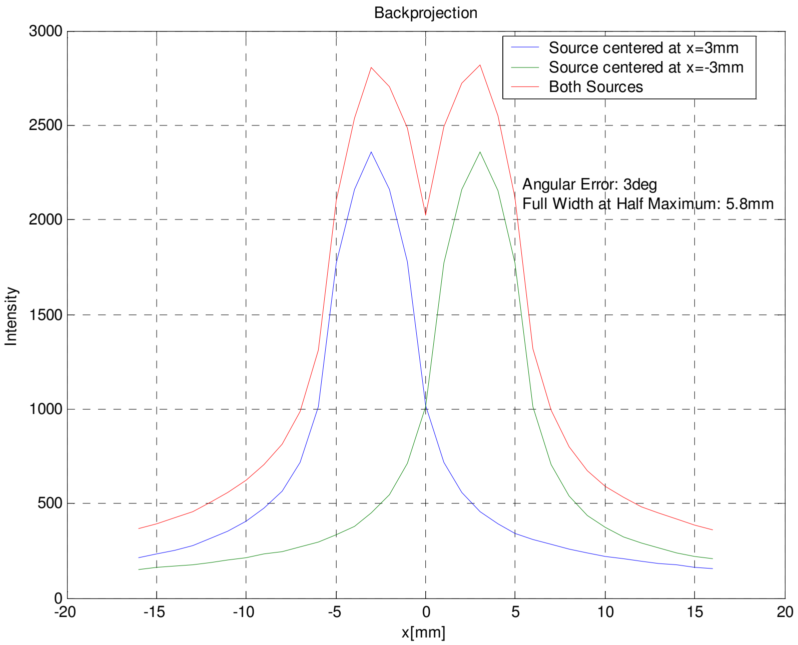

b)

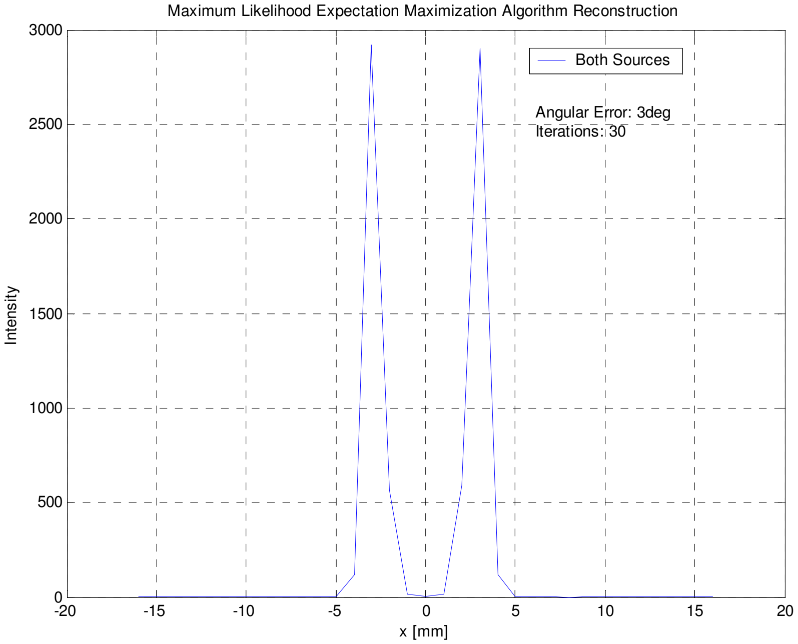

Fig. 17. Image reconstruction of simulated data of a point-like source at 40 mm from the detector and at 3 and -3 mm from detector center, along the direction parallel to the detector face. Error associated with the scattering angle: 3deg. a) Backprojection; b) Maximum likelihood expectation maximization algorithm reconstruction.

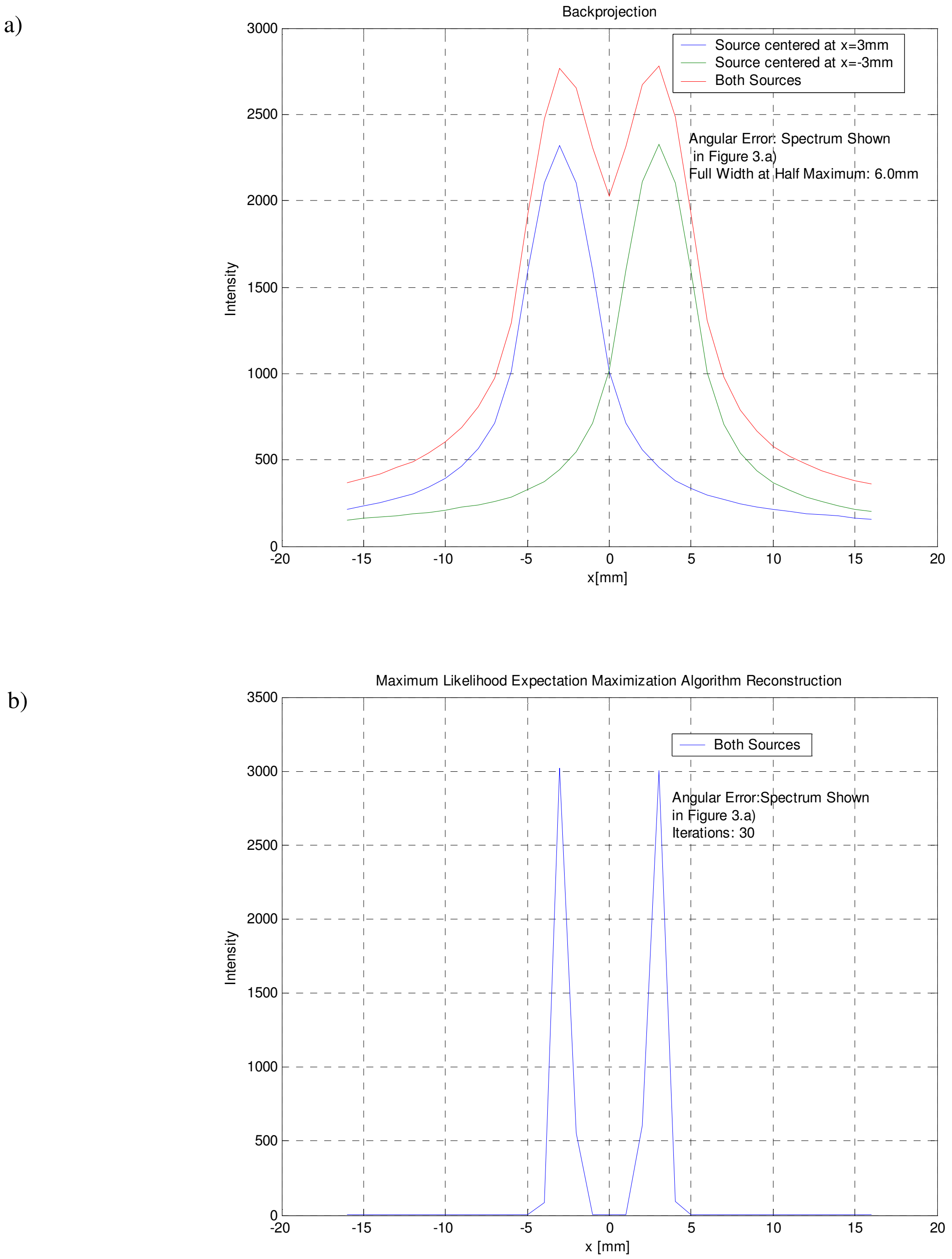

Fig. 18. Image reconstruction of simulated data of a point-like source at 40 mm from the detector and at 3 and -3 mm from detector center, along the direction parallel to the detector face. Error associated to Scattering Angle: Average for all cone apertures and distance between first and second interaction of the gamma-ray. a) Backprojection; b) Maximum likelihood expectation maximization algorithm reconstruction.

4.5 IMAGE RECONSTRUCTION OF EXPERIMENTAL AND SIMULATED SPHERES

An experiment was carried on by using a gamma-ray emitting source and the block type detection system described in paragraph 1.3. The source is Sn^{113} in a solution contained into a hollow sphere made of an unspecified polymer less than a millimeter in thickness. This radioisotope emits predominantly two gamma rays, one of which at 24 keV, the other at 392 keV, the latter being the most probable decay mode of the radioisotope [4]. The level of the energy deposition above which signal acquisition is initiated is set to avoid recording spurious electrical signals. The threshold allowed acquisition of gamma-ray interaction sequences associated to cone apertures larger than 20 degrees. Measured gamma-ray interactions are processed to identify the parameters of the Compton cone using the code SPEIR, according to the criteria discussed in paragraph 1.3 and 1.4. A detailed description of the principles and functions of the SPEIR code are documented in [5]. Only interaction sequences leading to total measured energy deposition of 392 keV are used for image reconstruction. This selection principle excludes using gamma-rays that undergo scattering outside of the detector. The source was placed at two different positions with respect to the detector. Although the location of the two sources with respect to the detector was not measured with large accuracy, the longitudinal distance between them, along the x axis, was measured to be 10mm with a precision at the level of microns. Image reconstruction of the two empirical spheres was performed and their centroid identified. Simulated spherical objects with centroid corresponding to the empirical objects were produced using the procedures discussed in paragraph 4.2. The centroid coordinates of the two spherical sources in the simulations are: -39 mm, 6 mm, 4 mm, along y, x, z; and -39 mm, 16 mm, 4 mm, along y, x, z. The same number of events, 20000, for each sphere is used for reconstruction. The imaging system configuration is shown in Figure 19. For image reconstruction a probability density function associated to gamma-ray emission location that depends on linear distance between a point in field of view and the cone surface is used. The field of view is restricted to two dimensions and image reconstruction is performed along a slice 1 mm thick across the sphere center.

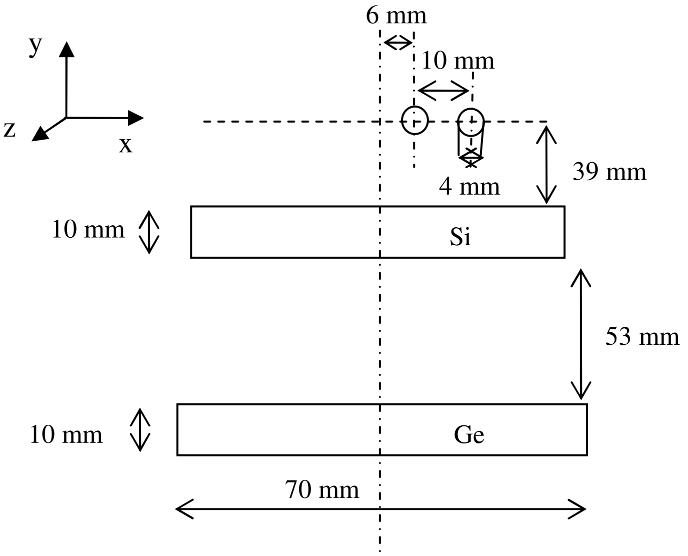

Fig. 19 Experimental and simulation imaging system used for spherical source image reconstruction.

Image reconstruction is performed by means of backprojection and list-mode maximum likelihood expectation maximization algorithm up to 10 iterations. As shown, around 10 iterations, the simulated object size tends to be identified with one voxel. Images of the simulated and experimental spheres are presented in Figure 20 to Figure 35.

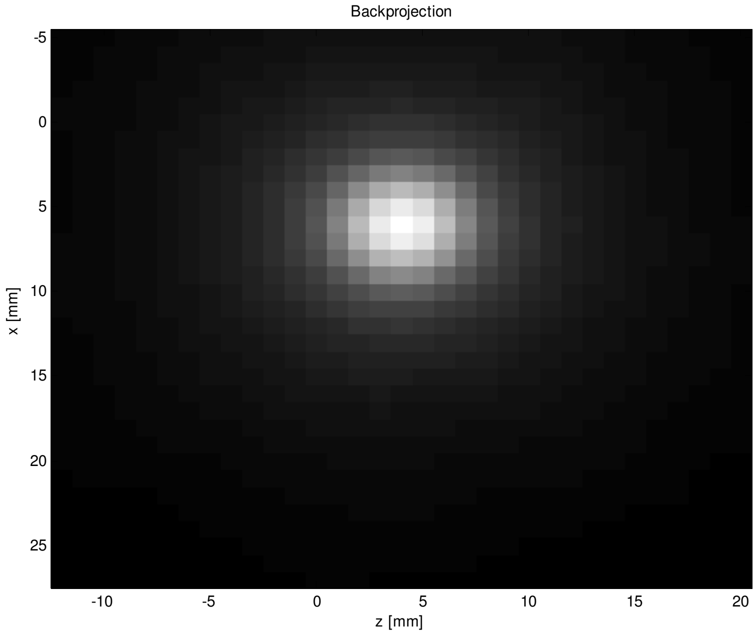

Fig. 20. Backprojection of simulated spherical source 4 mm in diameter; Two-dimensional slice one millimeter thick along x-z plane and across object centroid. Object centroid coordinates: x=6 mm; z=4 mm; y=-39 mm.

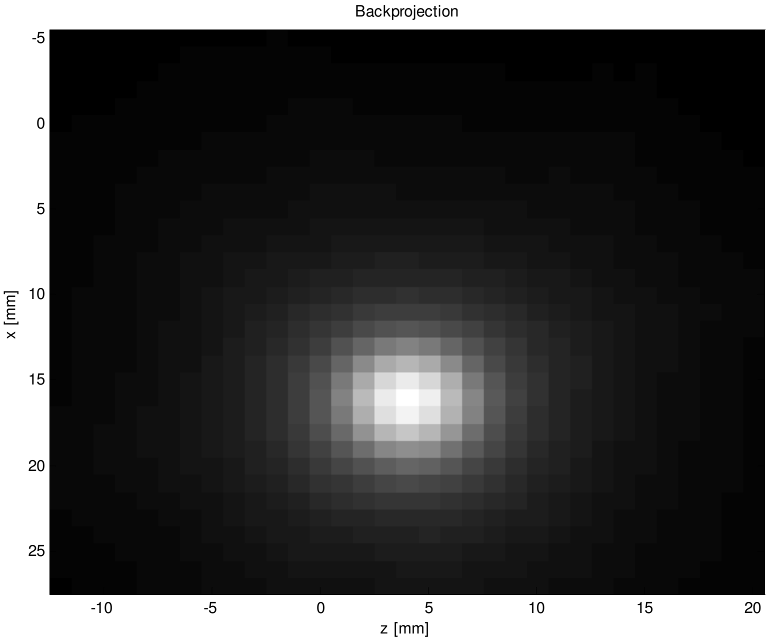

Fig. 21 Backprojection of simulated spherical source 4 mm in diameter; Two-dimensional slice one millimeter thick along x-z plane and across object centroid. Object centroid coordinates: x=16 mm; z=4 mm; y=-39 mm.

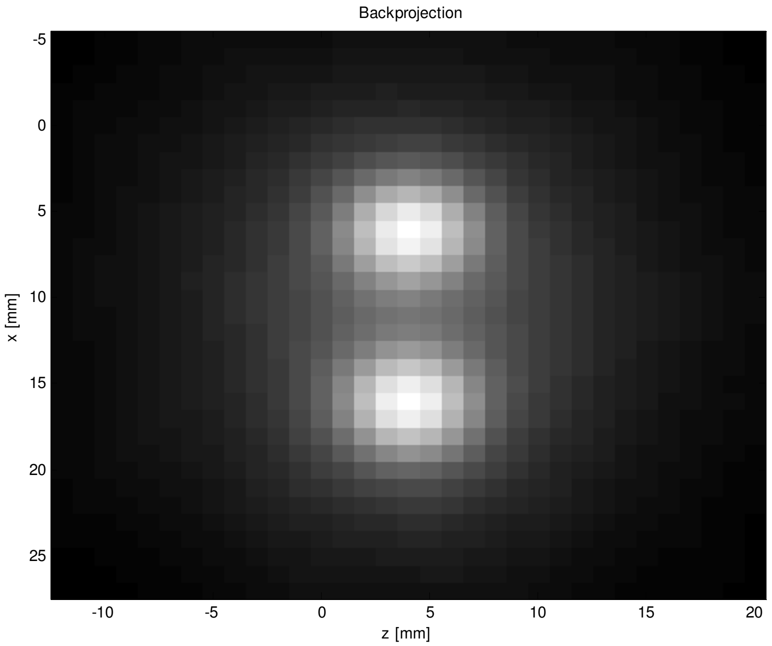

Fig. 22. Backprojection of two simulated spherical sources, each 4 mm in diameter; 2-dimensional slice one millimeter thick along x-z plane and across object centroid. Objects centroid coordinates: x=6 mm; z=4 mm; y=-39 mm and x=16 mm; z=4 mm; y=-39 mm.

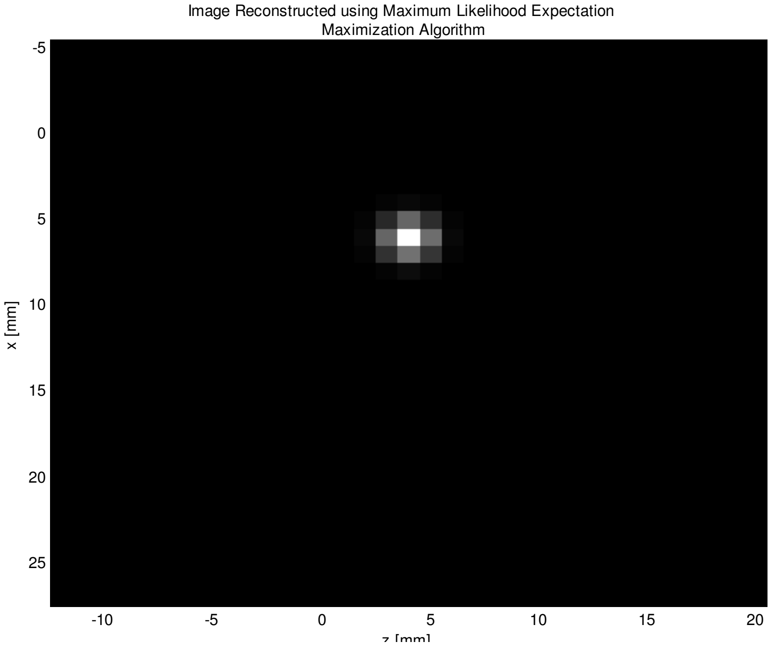

Fig. 23. Image of simulated spherical source 4 mm in diameter reconstructed using list-mode maximum likelihood expectation maximization algorithm; Two-dimensional slice one millimeter thick along x-z plane and across object centroid. Object centroid coordinates: x=6 mm; z=4 mm; y=-39 mm. Iterations: 10.

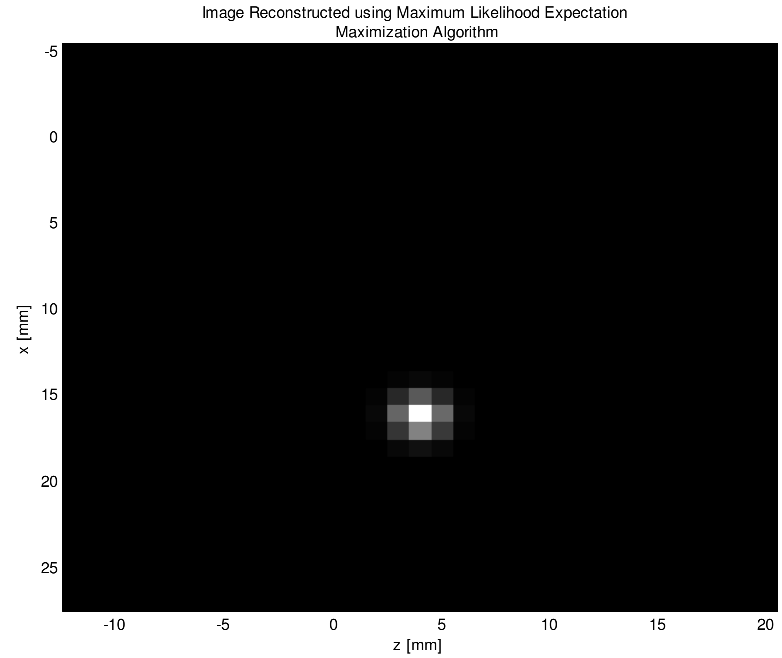

Fig. 24. Image of simulated spherical source 4 mm in diameter reconstructed using list-mode maximum likelihood expectation maximization algorithm; Two-dimensional slice one millimeter thick along x-z plane and across object centroid. Object centroid coordinates: x=16 mm; z=4 mm; y=-39 mm. Iterations: 10.

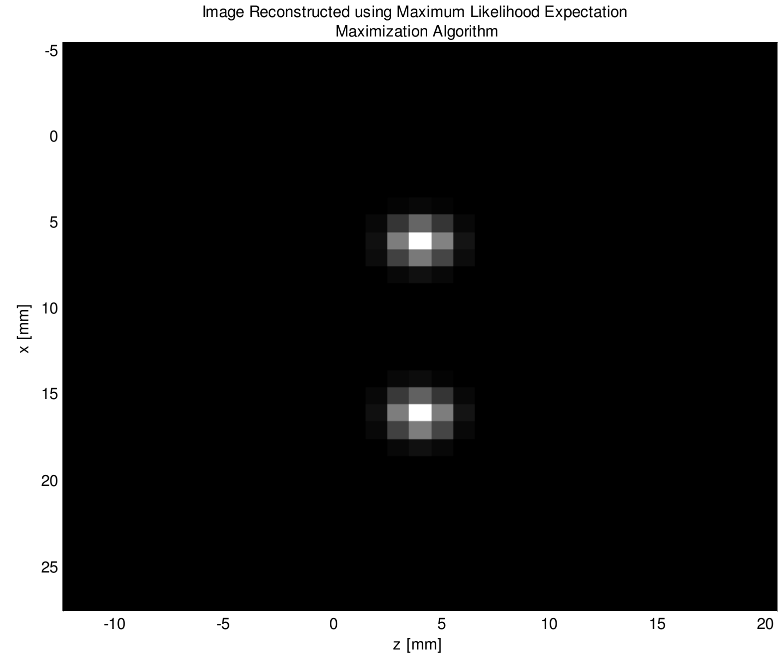

Fig.25 Image of two simulated spherical sources, each of them 4 mm in diameter, reconstructed using list-mode maximum likelihood expectation maximization algorithm; 2-dimensional slice one millimeter thick along x-z plane and across object centroid. Objects centroid coordinates: x=6 mm; z=4 mm; y=-39 mm and x=16 mm and z=4 mm; y=-39 mm. Iterations: 10.

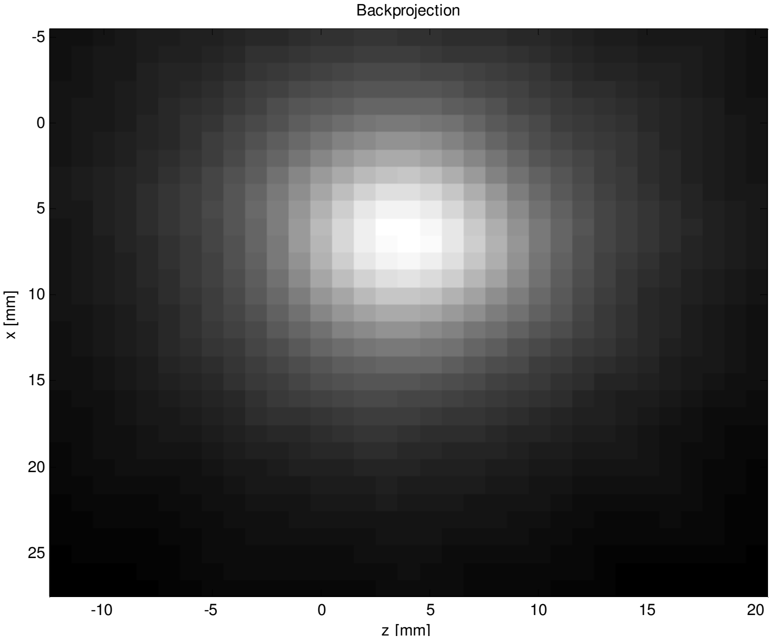

Fig.26 Backprojection of experimental spherical source 4 mm in diameter; Two-dimensional slice one millimeter thick along x-z plane and across object centroid. Object centroid coordinates: x=6 mm; z=4 mm; y=-39 mm.

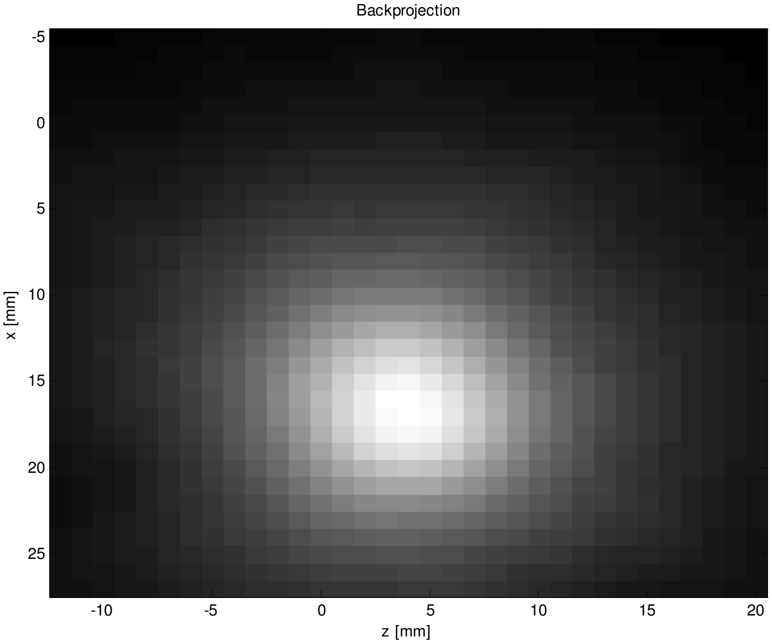

Fig. 27. Backprojection of experimental spherical source 4 mm in diameter; Two-dimensional slice one millimeter thick along x-z plane and across object centroid. Object centroid coordinates: x=6 mm; z=4 mm; y=-39 mm.

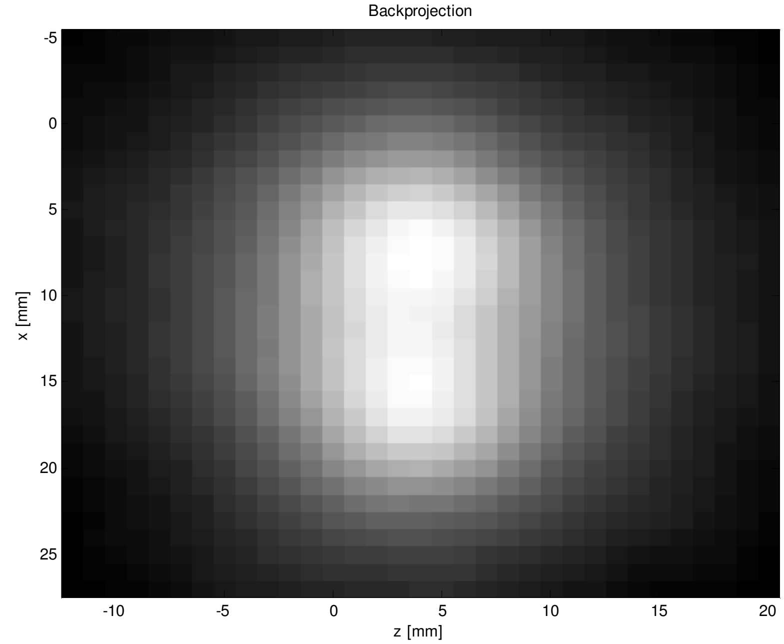

Fig. 28. Backprojection of two experimental spherical sources, each of them 4 mm in diameter; Two-dimensional slice one millimeter thick along x-z plane and across object centroid. Objects centroid coordinates: x=6 mm; z=4 mm; y=-39 mm and x=16 mm; z=4 mm; y=-39 mm.

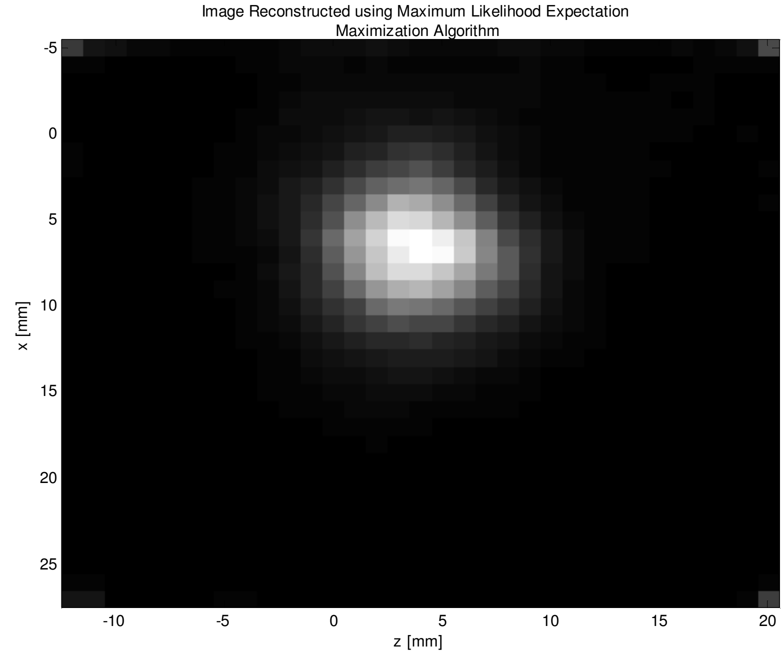

Fig. 29. Image of experimental spherical source 4 mm in diameter reconstructed using list-mode maximum likelihood expectation maximization algorithm; Two-dimensional slice one millimeter thick along x-z plane and across object centroid. Object centroid coordinates: x=6 mm; z=4 mm; y=-39 mm. Iterations: 10.

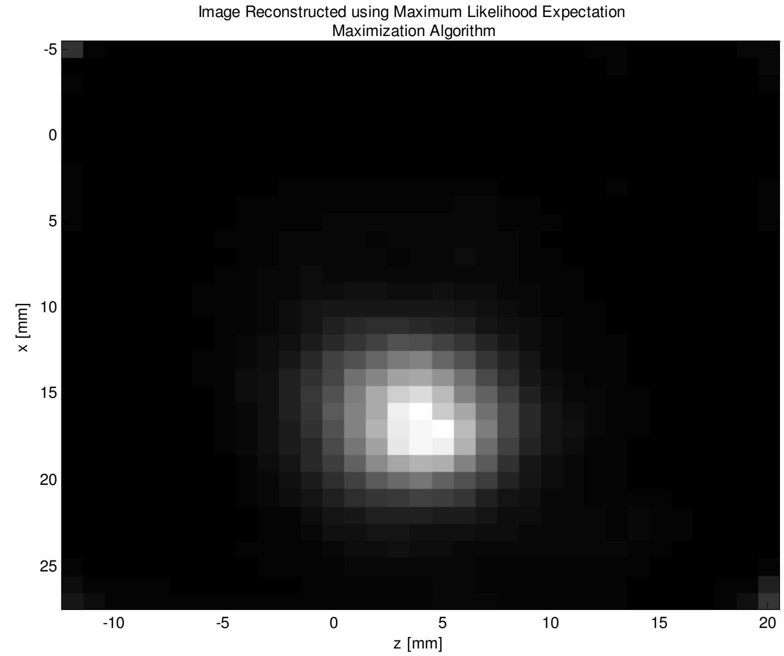

Fig. 30. Image of experimental spherical source 4 mm in diameter reconstructed using list-mode maximum likelihood expectation maximization algorithm; 2-dimensional slice one millimeter thick along x-z plane and across object centroid. Object centroid coordinates: x=16 mm; z=4 mm; y=-39 mm. Iterations: 10.

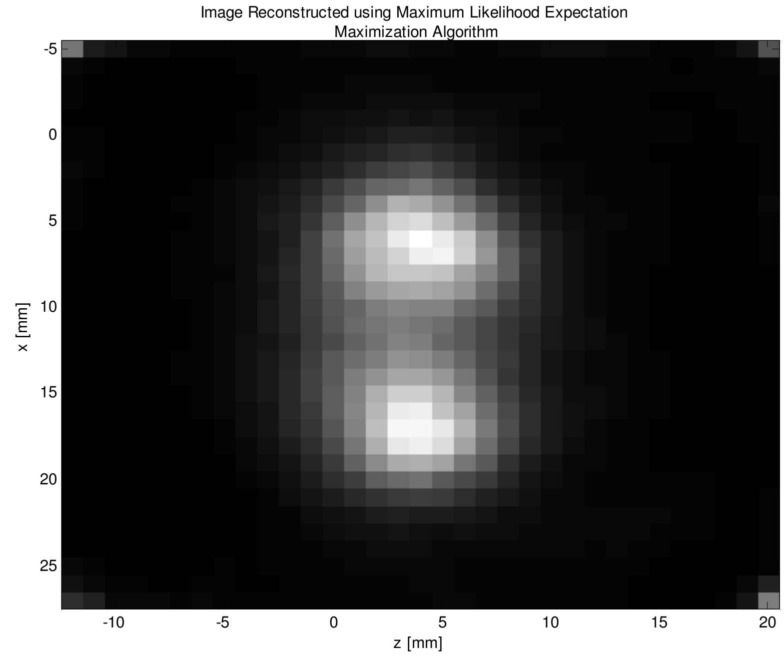

Fig. 31. Image of two experimental spherical sources, each of them 4 mm in diameter, reconstructed using list-mode maximum likelihood expectation maximization algorithm; Two-dimensional slice one millimeter thick along x-z plane and across object centroid. Objects centroid coordinates: x=16 mm; z=4 mm; y=-39 mm and x=6 mm; z=4 mm; y=-39 mm. Iterations: 10.

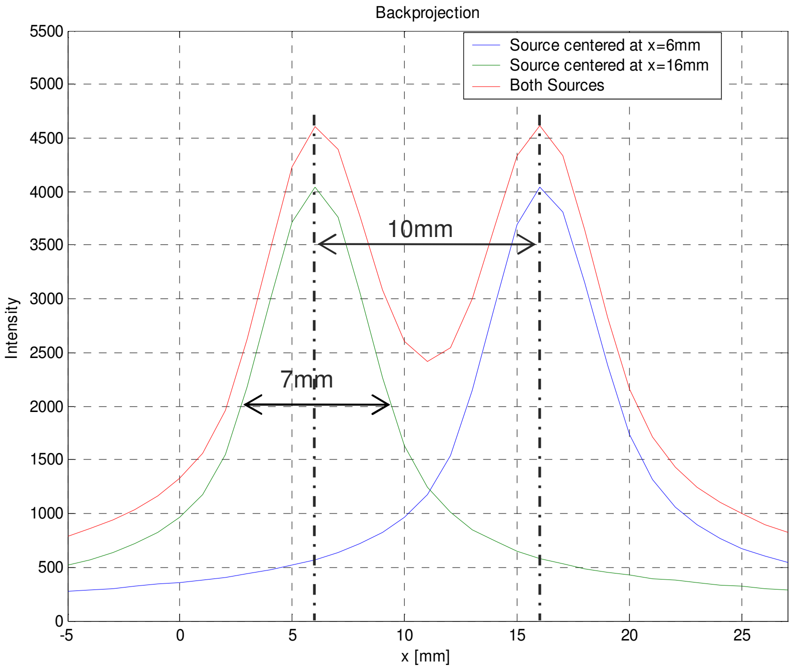

Fig. 32. Backprojection of simulated spherical sources; One-dimensional slice one millimeter thick along x direction and across object controid. Object centroid coordinates: x=6 mm; z=4 mm; y=-39 mm; x=16 mm; z=4 mm; y=-39 mm. Intensity reconstruction of each single spherical object, and both objects simultaneously are shown.

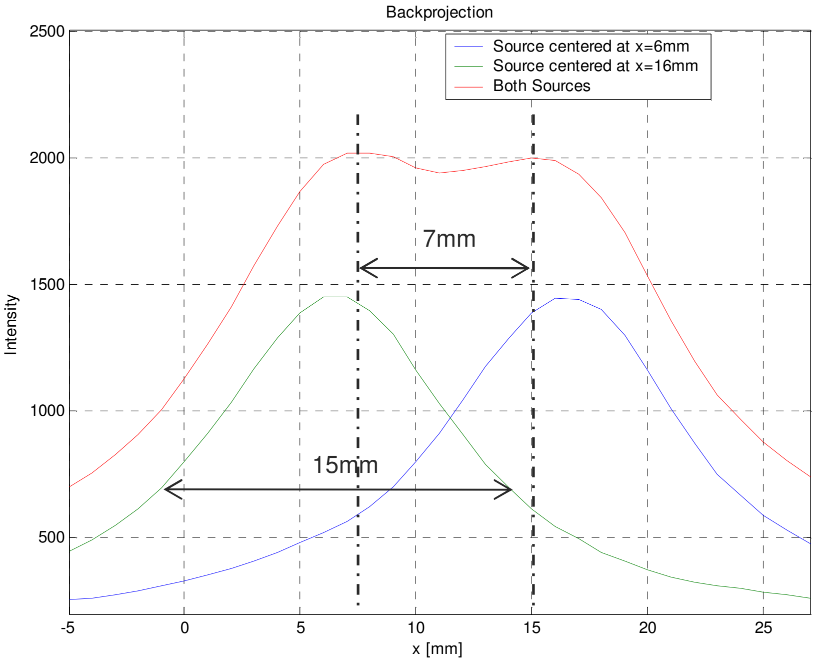

Fig. 33. Backprojection of experimental spherical sources; One-dimensional slice one millimeter thick along x direction and across object controid. Object centroid coordinates: x=6 mm; z=4 mm; y=-39 mm; x=16 mm; z=4 mm; y=-39 mm. Intensity reconstruction of each single spherical object, and reconstruction of both objects is shown.

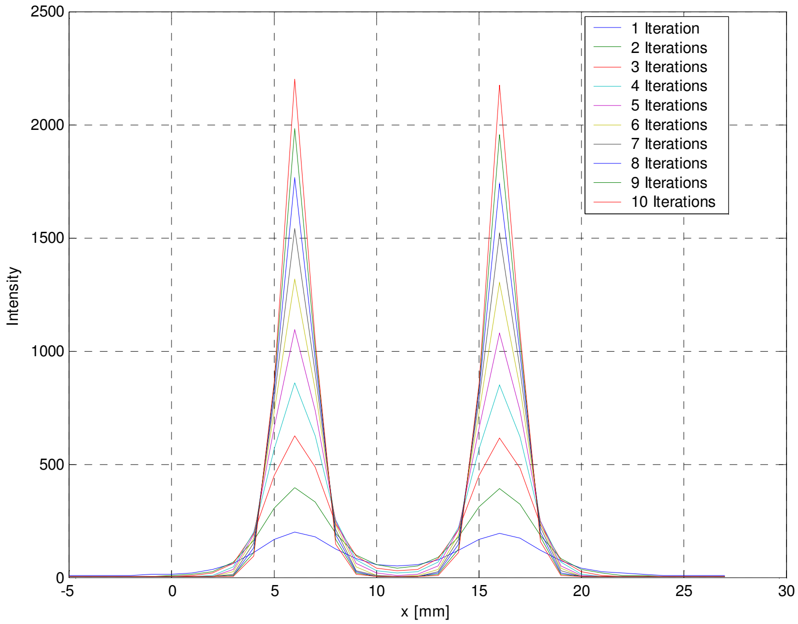

Fig. 34. Image reconstruction of two simulated spherical sources using maximum likelihood expectation maximization algorithm; One-dimensional slice one millimeter thick along x direction and across object controid. Objects centroid coordinates: x=6 mm; z=4 mm; y=-39 mm and x=16 mm; z=4 mm; y=-39 mm. The intensity is shown as a function of iteration number.

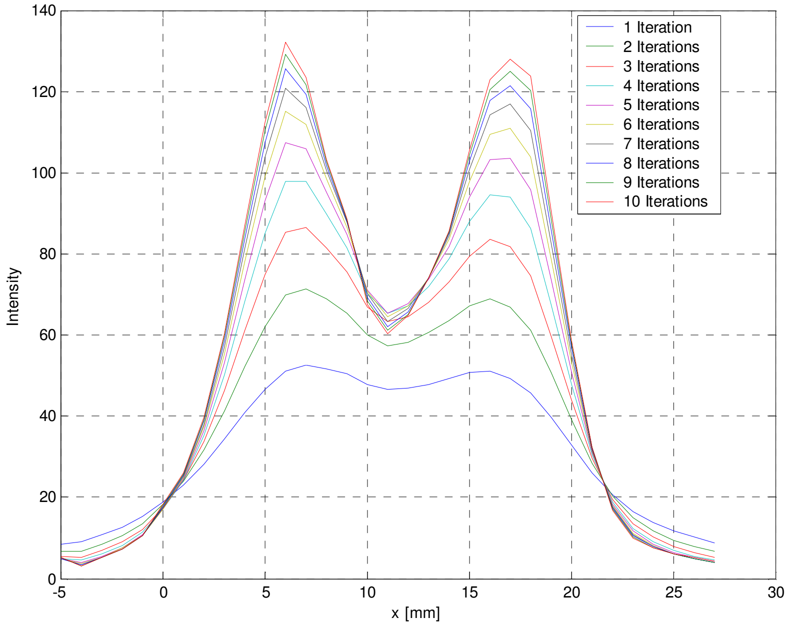

Fig. 35. Image reconstruction of two experimental spherical sources using maximum likelihood expectation maximization algorithm; 1-dimensional slice one millimeter thick along x direction and across object controid. Objects centroid coordinates: x=6 mm; z=4 mm; y=-39 mm and x=16 mm; z=4 mm; y=-39 mm. The intensity is shown as a function of iteration number.

Two dimensional images of experimental and simulated spherical sources are shown on the plane parallel to the detector face. As shown, the shape of all images, both of the simulated and experimental spheres, resembles a round object. Images of the simulated spheres are presented in Figure 20 to Figure 25, where Figure 20, Figure 21, and Figure 22 are backprojection reconstruction, Figure 23, Figure 24, and Figure 25 are maximum likelihood expectation maximization algorithm reconstructions. Figure 20 and Figure 21 illustrate the image of each single sphere in two different positions and Figure 22 illustrates both spheres, reconstructed using backprojection. By observing all images, it is noticed that the centroid of the spheres is correctly identified. The size of the sphere in back-projection, shown in Figure 34, is larger than the actual size of the object, and the object of 4 mm appears as 7 mm in size. Thus, as shown in Figure 22 and Figure 34 the two 4 mm in diameter object spheres separated by a distance of 10 mm are well distinguishable. When performing image reconstruction using maximum likelihood expectation maximization algorithm, the size of the sphere appears smaller, and decreases at each iteration cycle, as shown in the one dimensional profile of Figure 34.

Similar results, in terms of shape identification are obtained for the experimental spheres, as shown from Figure 26 to Figure 31. Figure 26 and Figure 27 show that the centroid of each single sphere appears to be well identified, when imaging each single sphere separately. Figure 29, Figure 30, and Figure 35 show that the size of each sphere decreases when using maximum likelihood expectation maximization algorithm for image reconstruction, however it is larger than the simulated spheres at comparable iteration cycle. The fact that the size of the experimental spheres is larger than the simulated spherical sources, about 15 mm full width at half maximum intensity when using backprojection, makes the two spheres to appear closer than they are. As shown in Figure 35 and Figure 33, it is still possible to distinguish the two spheres separated by 10 mm, but they appear closer.

The broadening of the image of the experimental object with respect to the image of the simulated object is believed to be due to larger errors involved in the reconstruction of the cones from experimental observable parameters. As mentioned, the simulated interactions are representative of observables obtained with a detection system that has perfect accuracy and no uncertainty for energy deposition, position of interaction and time. To the simulated parameters errors are applied: a finite precision error for energy deposition and location of interaction, and a systematic error due to the fact that the orbital electron that undergoes scattering with the photon is unknown. These errors are an estimate intended to represent the precision errors associated to a real imaging detector and due to the fact that the orbital electron which undergoes scattering is unknown. No accuracy errors on position of interaction and energy deposition, nor errors due to time resolution are applied to the simulated data. Differences between simulated and experimental images are thus believed to be due to accuracy errors on energy deposition and position of interaction, time resolution, and any spurious detector and data acquisition process or background signal resulting in apparent interaction sequences. In order to obtain an indication of the deviation between cones reconstructed from simulated observable and cones reconstructed from experimental observables, the histogram of the minimum angular distance between each cone to the sphere centroid has been generated for: the simulated sphere with centroid at x=6 mm, z=4 mm, y=-39 mm; the experimental sphere whit same centroid at x=6 mm, z=4 mm, y=-39 mm. The histogram related to the simulated cones is shown in Figure 36, the histogram related to the experimental cones is shown in Figure 37, and enlargements of the two histograms are shown in Figure 38 and Figure 39.

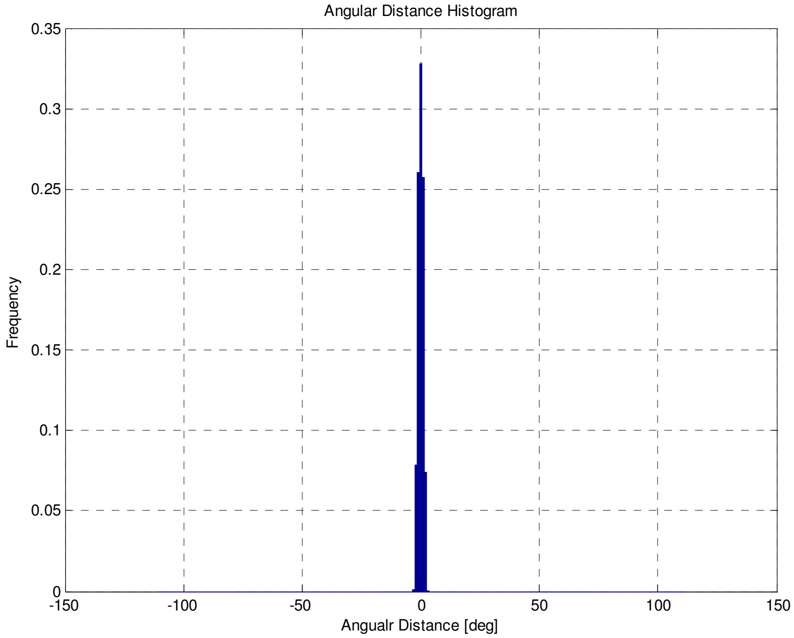

Fig. 36. Histogram of minimum angular distance between each cone generated from simulated data and the simulated spherical object centroid.

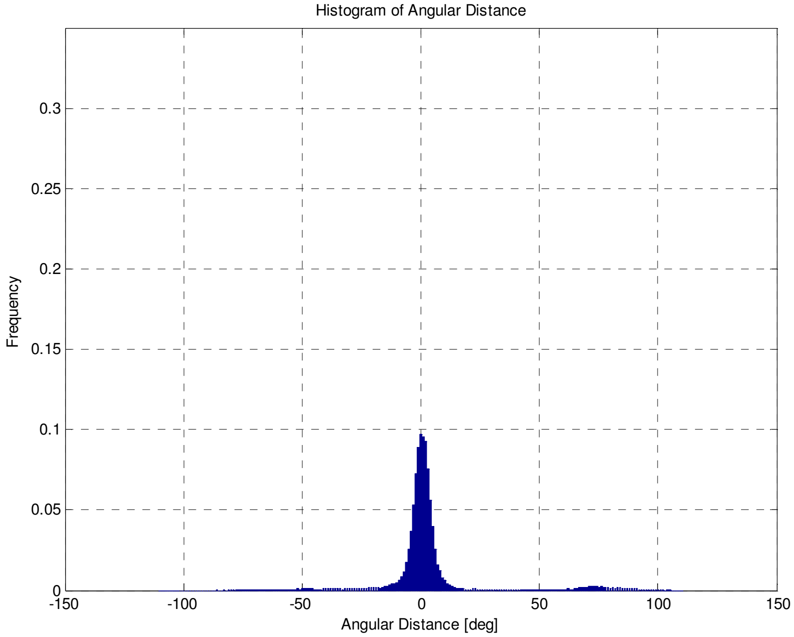

Fig. 37. Histogram of minimum angular distance between each cone generated from experimental data and the experimental spherical object centroid.

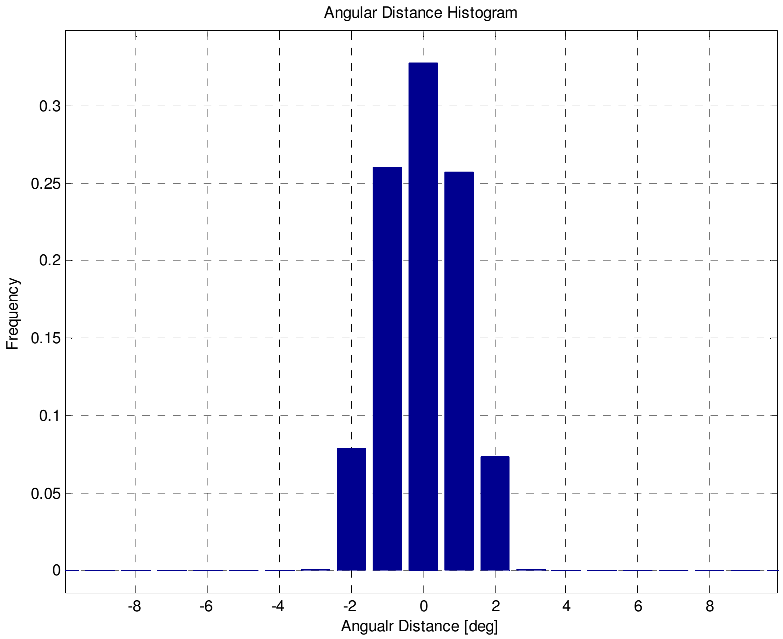

Fig. 38. Enlargement of histogram of minimum angular distance between each cone generated from simulated data and the simulated spherical object centroid.

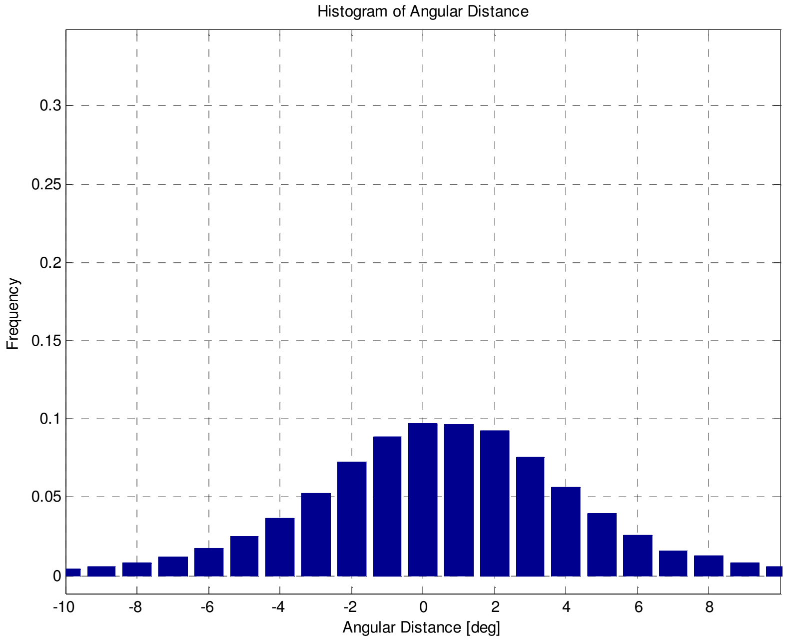

Fig. 39. Enlargement of histogram of minimum angular distance between each cone generated from experimental data and the experimental spherical object centroid.

As the figures show, the histogram pertaining to the experimentally determined cones is different from what obtained when using simulated cones. About 50% of cones that are reconstructed outside of the region of space occupied by the experimental sphere. This fraction contributes to the broadening of the image and it is believed to be the major cause of the deviation in size between the image of the simulated sphere and the experimental sphere.

It should be noted that the size of the spheres tends to decrease at each iteration step when performing image reconstruction using the maximum likelihood expectation maximization algorithm. Although not shown in the figures, the size of the 4 mm in diameter simulated sphere, which is comparable to the resolution of the imaging system, is identified with one voxel 1 mm in side after 30 iterations. This does not seems to happen for the experimental sphere whose image already in backprojection is broader due to the cones that are reconstructed outside of the spherical object. Although not shown in the figures, iteration has been performed on the experimental data up to several hundreds cycles; the image never assumed the size of only one voxel, but the size kept decreasing at each iteration.

4.6 IMAGE RECONSTRUCTION OF SIMULATED LINE SOURCES

Images of simulated line sources have been produced using both the block-type imaging detector and the spherical imaging detector, using backprojection and maximum likelihood expectation maximization algorithm.

The source is a rod of 4 mm x 4 mm square cross section and 52 mm long. The rod centroid is placed at the center of the spherical imaging system and at the center of the block type detection system, at a distance of 40 mm from the detector. The average gamma-ray emissions have a uniform distribution over the rod volume. The simulated gamma-ray interactions in the detector and associated cones describing gamma-ray emission region are obtained as described in paragraph 4.2. The errors applied to the cones are evaluated as discussed in paragraph 4.2 and are shown in Figure 3 a), for the block-type imaging system, and in Figure 3 b), for the spherical imaging system. The probability density function used to describe gamma-ray emission probability as a function of distance from cone surface depends on linear distance from a location in field of view to cone surface. Two dimensional image reconstruction is used for the block type imaging system, and three dimensional image reconstruction is used for the spherical imaging system. No correction for detection efficiency dependence on location within field of view is made. The field of view is discretized into cubical voxels, 4 mm in side.

Images obtained with the block type detection system are presented from Figure 40 to Figure 43, and images obtained with the spherical detection system are shown in Figure 44 to Figure 49.

4.6.1 RESULTS FOR THE BLOCK TYPE IMAGING SYSTEM

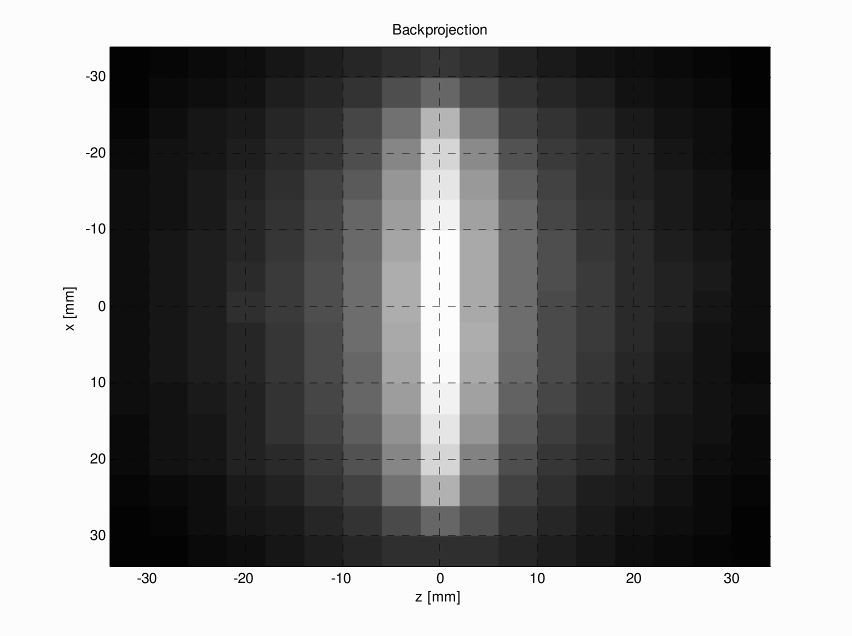

Fig. 40. Image of a simulated distribute source of uniform intensity. The source is a rod placed at 40 mm form the block type detector imaging system. The rod is 52 mm long and has a square cross section 4mm in side. Image reconstruction is performed via backprojection along the plane parallel to the detector face.

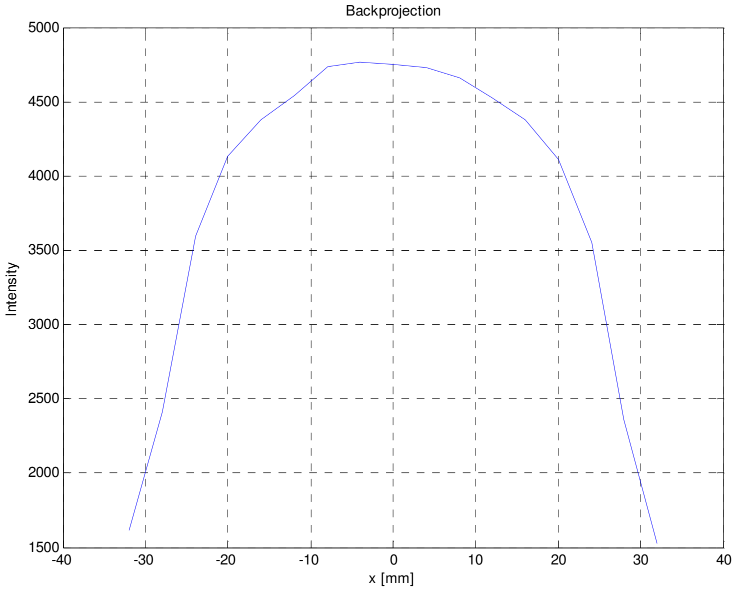

Fig. 41. Image of a simulated distributed source of uniform intensity. The source is a rod placed at 40 mm from the block type detector imaging system. The rod is 52 mm long and has a square cross section 4 mm in side. Image reconstruction is performed via backprojection along the plane parallel to the detector face. The one dimensional image is a slice 4 mm thick across source axis.

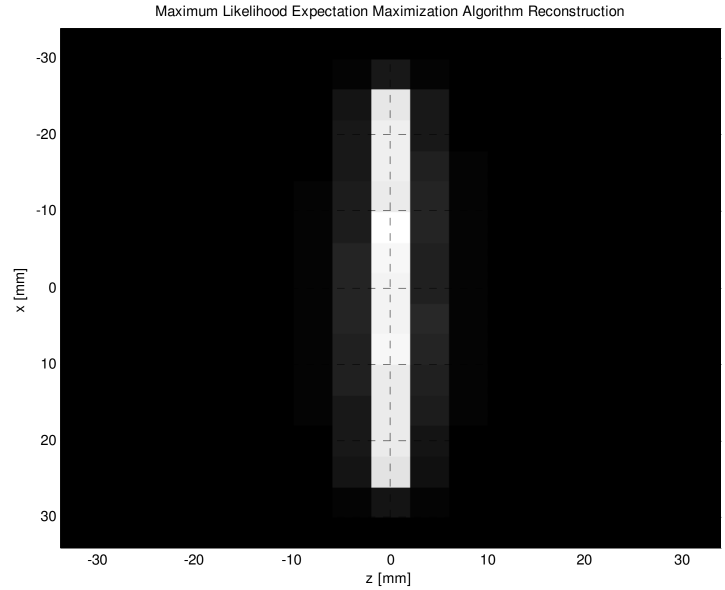

Fig. 42. Image of a simulated source of uniform intensity. The source is a rod placed at 40 mm from the block type detector imaging system. The rod is 52 mm long and has a square cross section 4 mm in side. Image reconstruction is performed via maximum likelihood expectation maximization algorithm, up to 10 iterations, along the plane parallel to the detector face. No correction for detection efficiency variation is applied.

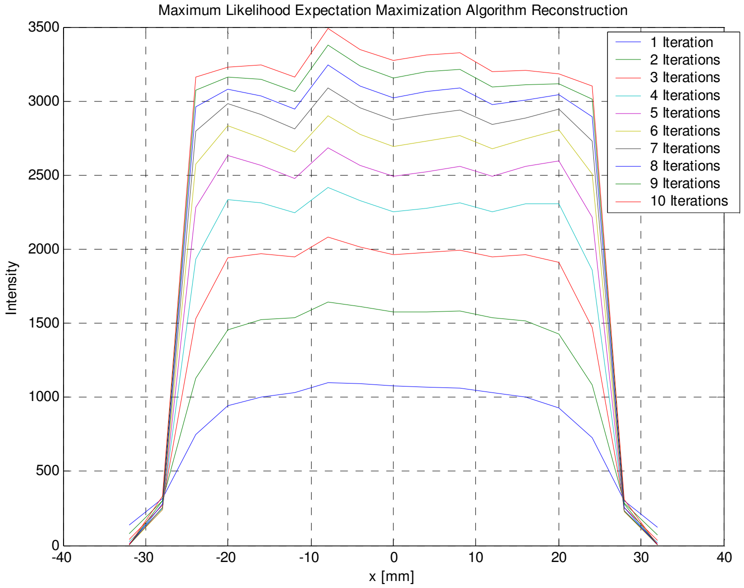

Fig. 43. Image of a simulated source of uniform intensity. The source is a rod placed at 40 mm from the block type detector imaging system. The rod is 52 mm long and has a square cross section 4 mm in side. Image reconstruction is performed via maximum likelihood expectation maximization algorithm, up to 10 iterations, along the plane parallel to the detector face. The one-dimensional image is a slice 4 mm thick across rod axis. No correction for detection efficiency variation is applied.

4.6.2 RESULTS FOR THE SPHERICAL IMAGING SYSTEM

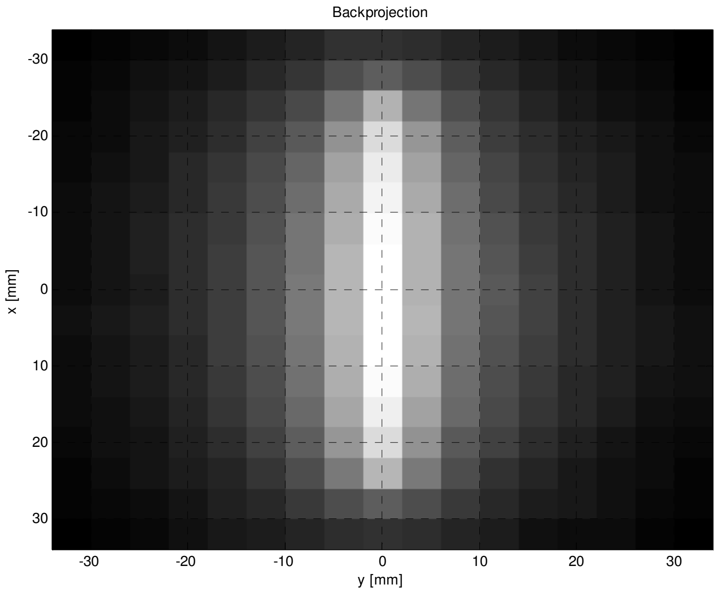

Fig. 44. Image of a simulated distribute source of uniform intensity. The source is a rod with baricenter placed at the center of the spherical imaging system. The rod is 52 mm long and has a square cross section 4 mm in side. Image reconstruction is performed via backprojection in the three dimensional space. The two-dimensional image is a slice 4 mm thick across rod axis and along the x-y plane.

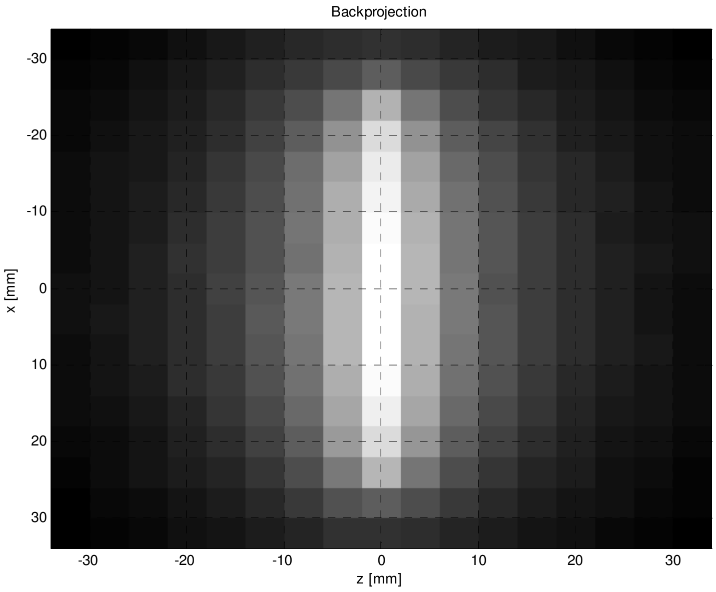

Fig. 45. Image of a simulated distribute source of uniform intensity. The source is a rod with baricenter placed at the center of the spherical imaging system. The rod is 52 mm long and has a square cross section 4 mm in side. Image reconstruction is performed via backprojection in the three dimensional space. The two-dimensional image is a slice 4 mm thick across rod axis and along the x-z plane.

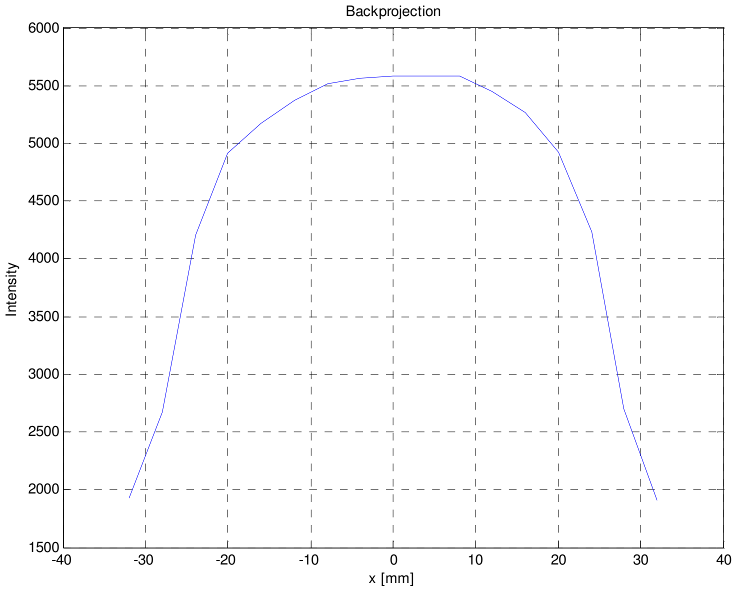

Fig. 46. Image of a simulated distribute source of uniform intensity. The source is a rod with baricenter placed at the center of the spherical imaging system. The rod is 52 mm long and has a square cross section 4 mm in side. Image reconstruction is performed via backprojection in the three dimensional space. The one-dimensional image is a slice 4mm thick across rod axis and along the x direction.

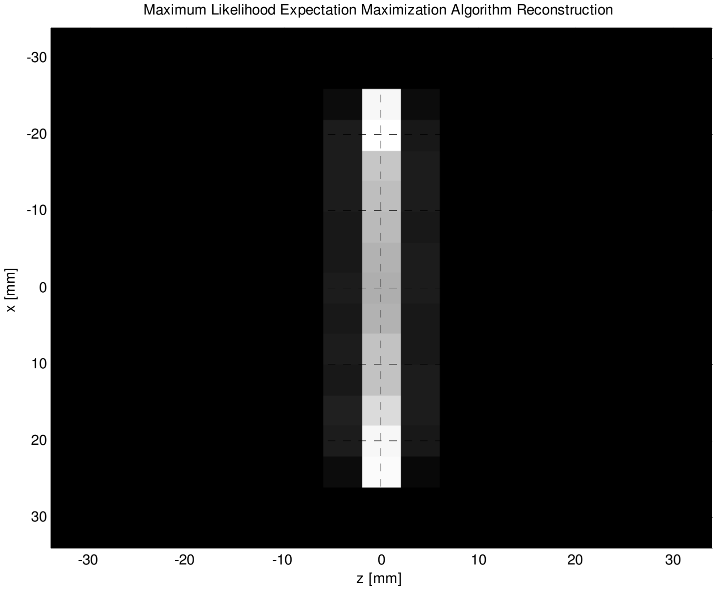

Fig. 47. Image of a simulated distribute source of uniform intensity. The source is a rod with baricenter placed at the center of the spherical imaging system. The rod is 52 mm long and has a square cross section 4 mm in side. Image reconstruction is performed via maximum likelihood expectation maximization algorithm, up to 10 iterations, in the three dimensional space. The two-dimensional image is a slice 4mm thick across rod axis and along the x-z plane. No correction for detection efficiency variation is applied.

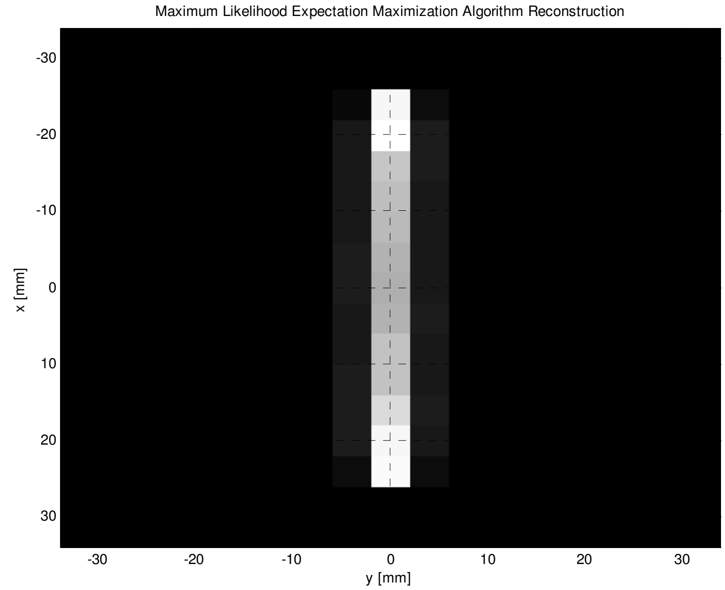

Fig. 48. Image of a simulated source of uniform intensity. The source is a rod with baricenter placed at the center of the spherical imaging system. The rod is 52 mm long and has a square cross section 4 mm in side. Image reconstruction is performed via maximum likelihood expectation maximization algorithm, up to 10 iterations, in the three dimensional space. The two-dimensional image is a slice 4 mm thick across rod axis and along the x-y plane. No correction for detection efficiency variation is applied.

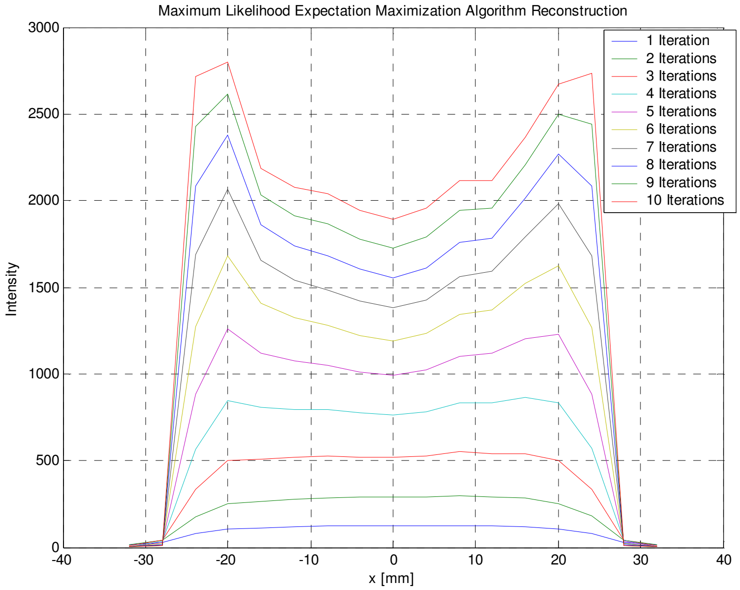

Fig. 49. Image of a simulated source of uniform intensity. The source is a rod with baricenter placed at the center of the spherical imaging system. The rod is 52 mm long and has a square cross section 4 mm in side. Image reconstruction is performed via maximum likelihood expectation maximization algorithm, up to 10 iterations, in the three dimensional space. The one-dimensional image is a slice 4 mm thick across rod axis and along the x direction. No correction for detection efficiency variation is applied.

4.6.3 DISCUSSION

As a general comment, the shape and position of the object rod are identified in the image, although there are intensity variations across field of view in the image that are not characteristic of the object itself. Images obtained with maximum likelihood expectation maximization algorithm seem to provide a better estimate of the region of space which confines the source intensity, both for the rod cross section and length. The rod cross section has a size comparable to the resolution of the imaging system and the voxel size. Under these conditions, the object rod cross section is identified with a voxel when maximum likelihood expectation maximization image reconstruction is performed. The length of the rod also seem to be well reproduced in the image. As mentioned, the images presented are obtained without corrections for detection efficiency dependence on position within field of view. Thus the images are affected by artifacts that shall be corrected in future developments. As shown in Figure 6 in Chapter 1, the detection efficiency variation for the block type detector along the region that corresponds to the rod axis is less than 10%, with maximum efficiency at the center of the rod. Detection efficiency variation for the spherical imaging system follows a different trend, with efficiency being the lowest at the center of the rod. Detection efficiency variation might cause the image obtained with the spherical detector, via maximum likelihood expectation maximization algorithm, to have intensity that increases going from the center to the edge of the rod. Smaller intensity variation are observed for the image obtained with the block type detector.

4.7 IMAGE RECONSTRUCTION OF SIMULATED LINE SOURCE IN A BACKGROUND

Image reconstruction of a rod in a planar background is performed using the block-type detector of Figure 1. The source is a rod 1mmx1mm in cross section, 46mm long in a planar background radioactivity distribution, 46mmx46mm in side and 1mm thick. The rod is placed at the center of the imaging system along the x axis. The planar radioactivity distribution and the rod are placed at 50mm from the detector. The rod has a uniform radioactivity distribution four times larger than the planar background radioactivity distribution. The source emits gamma-ray at 392 keV. The observables in the detector are produced using the transport and Monte Carlo code Geant 4. Backprojection cones describing gamma-ray emission region are obtained as described in paragraph 4.2. The error applied to all of the cones is one degree and the voxels are cubical, 1mm in side. The probability density function used to describe gamma-ray emission probability as a function of distance from cone surface depends on linear distance from a location in field of view to cone surface. Two dimensional image reconstruction is performed on a planar slice 1mm thick encompassing the whole source thickness. The number of cones used for reconstruction is 330000. No correction for detection efficiency dependence on location within field of view is made. Images obtained are presented from Figure 50 to Figure 53. As shown in Figure 50 and 51, the rod can be distinguished from the background even in simple backprojection. Iterating via maximum likelihood expectation maximization algorithm makes the rod more distinguishable, as shown in Figure 52 and 53. The standard deviation between voxels is similar in the rod and in the background and it is observed to decrease with number of cones used to produce the image.

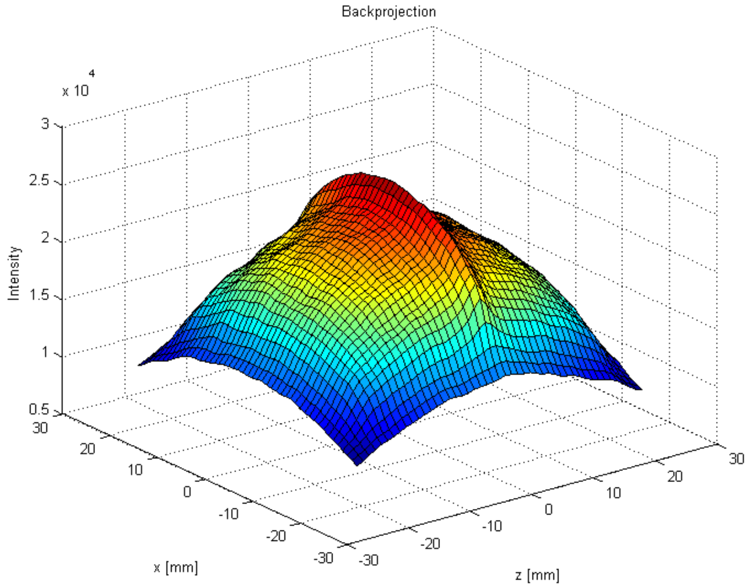

Fig. 50. Image of a simulated distributed source. The source is a rod with baricenter placed at the center of the block-type imaging system immersed in a planar background with uniform radioactivity distribution; the radioactivity ratio is 5 to 1. The rod is 46 mm long and has a square cross section 1 mm in side, the planar background is 46mm x 46mm in sides and 1mm thick. Image reconstruction is performed via backprojection in two-dimensional space. The two-dimensional image is a slice 1mm thick across rod axis and along the x-z plane.

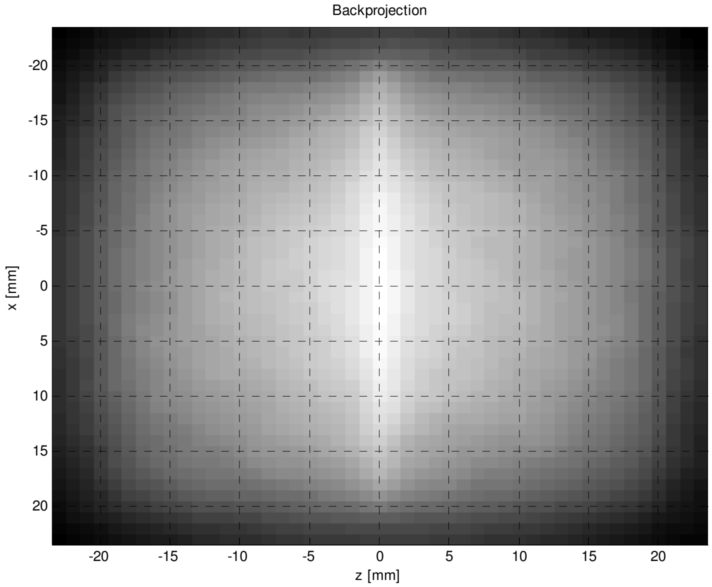

Fig. 51. Image of a simulated distributed source. The source is a rod with baricenter placed at the center of the block-type imaging system immersed in a planar background with uniform radioactivity distribution; the radioactivity ratio is 5 to 1. The rod is 46 mm long and has a square cross section 1 mm in side, the planar background is 46mm x 46mm in sides and 1mm thick. Image reconstruction is performed via backprojection in two-dimensional space. The two-dimensional image is a slice 1mm thick across rod axis and along the x-z plane.

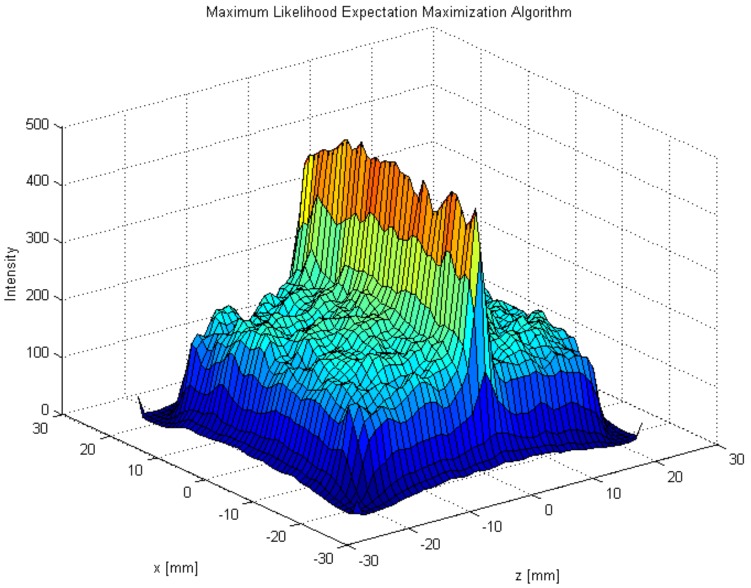

Fig. 52. Image of a simulated distributed source. The source is a rod with baricenter placed at the center of the block-type imaging system immersed in a planar background with uniform radioactivity distribution; the radioactivity ratio is 5 to 1. The rod is 46 mm long and has a square cross section 1 mm in side, the planar background is 46mm x 46mm in sides and 1mm thick. Image reconstruction is performed via maximum likelihood expectation maximization algorithm, up to ten iterations, in two-dimensional space. The two-dimensional image is a slice 1mm thick across rod axis and along the x-z plane.

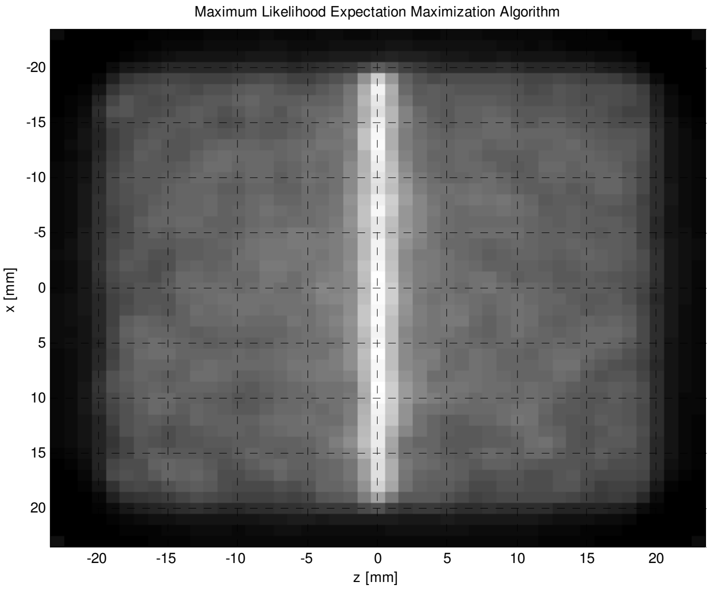

Fig. 53. Image of a simulated distributed source. The source is a rod with baricenter placed at the center of the block-type imaging system immersed in a planar background with uniform radioactivity distribution; the radioactivity ratio is 5 to 1. The rod is 46 mm long and has a square cross section 1 mm in side, the planar background is 46mm x 46mm in sides and 1mm thick. Image reconstruction is performed via maximum likelihood expectation maximization algorithm, up to ten iterations, in two-dimensional space. The two-dimensional image is a slice 1mm thick across rod axis and along the x-z plane.

4.8 DISCUSSION

Image reconstruction via backprojection and maximum likelihood expectation maximization algorithm have been used to produce images using a spherical imaging system enclosing the field of view and a block-type imaging system which provides only one view of the object. An approach that minimizes impulse response dependence on position within field of view has been developed to correct artifacts otherwise present in the image. This approach restricts imaging with the block-type detector to two dimensions, along the plane parallel to the detector face, while allows three dimensional imaging when using a spherical detector. The approach also involves the use of a linear error approximation. The equivalent linear error does not depend on distance of a point in field of view from gamma-ray first interaction in the detector, but does depend on a constant average distance from the detector and on the angular error.

It has been shown that the value of the angular error depends on the interaction sequence of the gamma-ray within the detection system, particularly on the distance between first and second interaction, on the gamma-ray energy, and on precision and accuracy of the detection system. Resolution estimates have been given as a function of the error. At energy above 662 keV, errors as small as 1deg could be achieved with current detectors by selecting interactions sequences that have first and second interactions separated by a distance greater than a few centimeters. Under these conditions distinguishing two point like sources separated by 2 mm is possible at a distance of 40 mm from the detector. Resolution gets poorer at smaller gamma-ray energies; at 392 keV an error of 3 degrees is obtained which allows distinguishing two sources separated by 6 mm. The resolution also gets poorer when using interactions that are separated by a smaller distance. If no selection of events that have first interaction in the first detector and second interaction in second detector is made, relatively large maximum errors and large variations among errors are obtained. Although about 50% out of the total multiple interaction sequences are shown to have error below 10 degrees and although not shown, the impulse response produced with such cones appears to be noisy, does not appear symmetric and it is not monotonic moving away from the maximum intensity peak. Further systematic investigation needs to be done to properly assess results on the image when using all interaction sequences, however results on preliminary images appear noisy.

Image reconstruction of experimental and simulated spherical sources has shown that the image of experimental objects is broader. This has been shown to be due to erroneous reconstruction of cones associated to interaction sequences. About 50% of the cones are shown to be outside of the source object volume, using current reconstruction methodologies. The major source of error is believed to be due to lack of time resolution of current detectors, which does not allow distinguishing the chronology of the interactions produced by the same gamma-ray within the detector, accuracy errors, and any spurious process resulting in erroneous signal identification. However, it is possible to distinguish two experimental spheres 4 mm in diameter separated by 10 mm distance center-to-center.

Images of distributed line sources have been produced in two dimensions for the block type imaging system, and in three dimensions for the spherical system. Volume size and location seem to be correctly identified, although within the image volume there are intensity variations that are not proper of the object. This is believed to be due to detection efficiency variation across field of view. Hence, the image intensity deviation with respect to the object seems to be consistent with the effects of detection efficiency variation. Correction for detection efficiency variation should been performed in a future stage.

4.9 FUTURE WORK

Corrections due to efficiency variation across field of view should be implemented in the image reconstruction algorithm when using maximum likelihood expectation maximization algorithm. Then image reconstruction of practical imaging cases should be carried out as proof of principle that the developed image reconstruction methodology can satisfy requirements of practical imaging cases on a case by case basis, and the proper detector configuration should be investigated in terms of configuration of block arrays or trajectory of a rotating block.

Bibliography

[1] *Geant4 Code Manual*, CERN and KEK, 1993, http://geant4.web.cern.ch/geant4/.
[2] *The Geant Low Energy Compton Scattering (GLECS) Package for Use in Simulating Advanced Compton Telescopes*, R. M. Kippen, New Astronomy Reviews 48 (2004) 221-225.
[3] G. Gullberg, Lawrence Berkeley National Laboratory, Berkeley, CA, USA, and A. Del Guerra, University of Pisa, Pisa, Italy, private communications.
[4] *Table of Radioactive Isotopes*, E Browne, R. Firestone, Virginia Shirley Editor.
[5] *SPEIR: A Ge Compton camera*, L. Mihailescu et al., Nuclear Instruments and Methods in Physics Research A 570, pp. 89-100, 2007.

SUMMARY

Methodologies for image reconstruction, image resolution, and detection efficiency evaluation, using a Compton imaging system have been developed. Results have been presented for practical block type detection elements which uses only one view of the object and for a spherical system that encloses the entire field of view.

An approach to image reconstruction based on simple backprojection and list-mode maximum likelihood expectation maximization algorithm has been developed. The approach minimizes the dependence of the impulse response on position within field of view. This approach allows imaging with a block-type detector of two-dimensional sources, while it makes possible to image a three-dimensional source when using an imaging system which provides full 4π view of the object.

Upper estimates of detection efficiency have been provided via simulations, for the block type detector, when using multiple gamma-ray interaction sequences that allow image reconstruction through backprojection. An efficiency of few percent is obtained at few centimeters from the detector. Some of the multiple interaction sequences carry however relatively large errors, which might result in a poor image quality. Selecting sequences that carry smaller errors in the effort of obtaining satisfactory image quality lowers the efficiency of about a factor of ten. Selecting gamma-rays that deposit the total energy in the detector, to allow imaging more than one isotope at the same time, lowers the efficiency of about a factor of two.

In order to estimate imaging system resolution, error evaluation methodologies have been developed. These take into account the uncertainty due to the fact that the energy and momentum of the orbital electron that collides with the photon is not known, and errors due to the precision of the detection system. Errors and image resolution improves at increasing gamma-ray energy. Also, selected interaction sequences have been shown to have smaller errors than others. By selecting appropriate interaction sequences, an error of about 1 degree is obtained for what concern instrument precision effects. An error of about 1 degree is estimated for energies around 662 keV, due to fact that it is not possible to establish the momentum of the orbital electron that undergoes scattering. This error should become negligible at higher energies. Resolution roughly decreases linearly with distance from detector. A total error of about 2 degrees, and a resolution of 2 mm is obtained at 662 keV at 40 mm distance from the detector; while an error of 3degrees, and a resolution of 3 mm is obtained at 392 keV at 40 mm from the detector. The corresponding detection efficiency is on the order of 10^{-3} for typical semiconducting block-type detectors few centimeters in size. Higher detection efficiency comes at the expenses of resolution and image quality. If all sequences are used, an efficiency of few percent could be obtained; preliminary image reconstruction results show however that a relatively noisy impulse response is obtained, however further studies should be systematically carried out to evaluate image quality on an case by case basis. Larger efficiency can be achieved with proper detector configurations.

Comparison of empirical and simulated sources shows that use of empirical observables introduces additional errors which result in a broadening of the object size. These errors are believed to be due to the time resolution of the detector, which does not allow disguising chronology of interactions originated by the same gamma-ray, instrument accuracy errors, and any other spurious process leading to erroneous signal identification in the detector. It is shown that it is possible to distinguish two experimental spherical sources emitting gamma-rays at 392 keV, 4 mm in diameter separated by 10 mm center-to-center distance, at a distance of 40 mm from the detector in absence of background.

Image reconstruction of practical imaging cases should be carried out in future developments as proof of principle that the developed image reconstruction methodology can satisfy image quality requirements and provide sufficient detection efficiency. A detailed analysis on the detection system configuration should be carried out to establish practical configurations of block type detectors or the trajectory of a block type detector needed to provide satisfactory images on a case by case basis.

APPENDIX A: *Image Reconstruction Code*

```
//////////////////////////////////////////////////////////////////////////////
//                         The code evaluates:
1)Image reconstruction via backprojection;
2)Minimum angualr distance between each cone and a selected direction
connecting cone vertex to a point in field of view;
3)Image reconstruction via maximum likelihood expectation maximization
algorithm;
The code can have as input two data files. Input data files contain the list
of parameters used for image reconstruiction. The parameters are related to
each gamma-ray interecation sequence in the detector. Parameter list, for
each sequence, is made of: Cone angular aperture; Cone vertex coordinates;
Cone axis direction coordinates; Total energy deposited by the gamma-ray in
the detection system; Estimate of the error affecting scattering angle;
Number of interaction of the gamma-ray in the detection system.
//////////////////////////////////////////////////////////////////////////////
#include "stdafx.h"
#include "cstdlib"
#include <cmath>
#include <math.h>
#include <stdio.h>
#include <stdlib.h>
#include <stdlib.h>
#include <vector>
#include <iostream>
#include <fstream>
#include <cctype>
#include <cstdio>
#include <strstream>
#include <stdio.h>
#include <stdio.h>
#include <time.h>
#include <list>
#define pi 3.1416
//******************************    USER INPUTS   ***************************
Cone Error is computed for a detection system which has Silicon as first
scatterer detector
***********************************************************************define
#define E0 392.0                         Energy of primary gamma ray [keV]
#define cone_ape_limit_inf 0.001         Select cones with aperture larger
than a certain treshold[rad]
#define cone_ape_limit_sup 3.14          Select cones with aperture smaller
than a certain treshold [rad]
#define cone_error_max     0.2           Select cones with error smaller than
a certain treshold [rad]
#define FOV_x 10.0                       Amplitude of FOV along x [mm]
#define FOV_y 32.0                       Amplitude of FOV along x [mm]
#define FOV_z 10.0                       Amplitude of FOV along x [mm]
#define XFOV_center 0.0                  Position of center of FOV along x
axis [mm]
#define ZFOV_center 0.0                  Position of center of FOV along y
axis [mm]
```

```
#define YFOV_center 15.0                 Position of center of FOV along z
axis [mm]
#define gx 5.0                           Grid size(number of voxels along x
axis)
#define gy 16.0                          Grid size(number of pixels along y
axis)
#define gz 5.0                           Grid size(number of pixels along z
axis)
#define G 612                            Total Number of Voxels (gx+1 * gy+1
* gz+1)
#define Event_num_max1 12000             Number of interaction sequences to
be used for the image reconstruction from first data file
#define Event_num_max2 0                 Number of interaction sequences to
be used for the image reconstruction from first data file
#define Event_num_max 12000              Sum of Event_num_max1+Event_num_max2
#define mag1 0.10                        Multiplication factor to be applied
to Event_num_max1 (reads more events from file 1 than requested  in order to
deliver requested events; hence some events, depending on cone error and
aperture, are discarded)
#define mag2 0.10                        Multiplication factor to be applied
to Event_num_max2 (reads more events from file 1 than requested  in order to
deliver requested events; hence some events, depending on cone error and
aperture, are discharged)
#define Iterations 10                    Number of maximum likelihood
expectation maximization algorithm iterations
#define limit_factor 1                   Multiple of the error on cone
aperture up to which integration of probability density function is performed
to estimate voxel intensity due to each cone;
#define treshold 0                       Cut off for intensity treshold below
which the voxel is assigned a zero intensity (Not used; leave it as zero)
#define ARM_Peak_Angle 0.17              This option is normally turned off;
The parameter is the minimum angular distance between the cone surface to the
direction described by the cone vertex position and the maximum intensity
voxel of the backprojected image[rad]; It could be used to selct only cones
having minimum distance below a certain value for image reconstruction of a
point source of known location;
using namespace std;
using std::list;
// Please, set the input file names at line 78 and 135
int main(void)    //int _tmain(int argc, _TCHAR* argv[]) //void
init_DATA(void);
{
//*******  Iterations To Be Recorded     ********
int Iter1, Iter2, Iter3, Iter4, Iter5, Iter6, Iter7, Iter8, Iter9, Iter10;
Iter1=0; Iter2=1; Iter3=2; Iter4=3; Iter5=4; Iter6=5; Iter7=6; Iter8=7;
Iter9=8; Iter10=9;
//*******  Binding Enrgy Of Silicon For Cone Error Computation
vector<double> B_en;   // [keV]
B_en.push_back(1.8389);
B_en.push_back(0.1487);
B_en.push_back(0.995);
B_en.push_back(0.0989);
B_en.push_back(0.0076);
B_en.push_back(0.003);
B_en.push_back(0.003);
int size_B_en;
size_B_en=B_en.size();
```

```
*********************************************************************
//////////////////////////////////////////////////////////////////////
//                           READ DATA FILE
//////////////////////////////////////////////////////////////////////
FILE *fp100;
if ((fp100=fopen("Data_Matrix1","rb+"))==NULL) {
      printf("Cannot open file.\n");
      exit(1);}
int s, a, Event_num_max1a;
double r;
vector<double> theta_va,x1_va,y1_va,z1_va,xd_va,yd_va,zd_va,Dtheta_va,
num_interacta,FOMa,Energya ;
Event_num_max1a=Event_num_max1+Event_num_max1*mag1;//read more events than
requested because there will be a selection
for (s=0;s<Event_num_max1a; s++) {// read number of requested events from
first data file
            fread(&r, sizeof(double), 1, fp100);
            theta_va.push_back(r);
            fread(&r, sizeof(double), 1, fp100);
            x1_va.push_back(r);
            fread(&r, sizeof(double), 1, fp100);
            y1_va.push_back(r);
            fread(&r, sizeof(double), 1, fp100);
            z1_va.push_back(r);
            fread(&r, sizeof(double), 1, fp100);
            xd_va.push_back(r);
            fread(&r, sizeof(double), 1, fp100);
            yd_va.push_back(r);
            fread(&r, sizeof(double), 1, fp100);
            zd_va.push_back(r);
            fread(&r, sizeof(double), 1, fp100);
            Energya.push_back(r);
            fread(&r, sizeof(double), 1, fp100);
            Dtheta_va.push_back(r);
            fread(&r, sizeof(double), 1, fp100);
            FOMa.push_back(r);
            fread(&r, sizeof(double), 1, fp100);
            num_interacta.push_back(r);
}
// Events Selection
vector<double> theta_v,x1_v,y1_v,z1_v,xd_v,yd_v,zd_v,Dtheta_v,
num_interact,FOM,Energy;
int pev, counta;
counta=0;
for (pev=0; pev<Event_num_max1a; pev++){//event index
      if (counta<Event_num_max1+1 ){
            if (Dtheta_va[pev]<cone_error_max & Dtheta_va[pev]<theta_va[pev]
            & theta_va[pev]<cone_ape_limit_sup &
            theta_va[pev]>cone_ape_limit_inf){
            counta=counta+1;
            theta_v.push_back(theta_va[pev]);
            x1_v.push_back(x1_va[pev]);
            y1_v.push_back(y1_va[pev]);
            z1_v.push_back(z1_va[pev]);
            xd_v.push_back(xd_va[pev]);
            yd_v.push_back(yd_va[pev]);
            zd_v.push_back(zd_va[pev]);
```

```
            Dtheta_v.push_back(Dtheta_va[pev]);
            Energy.push_back( Energya[pev]);
            FOM.push_back(FOMa[pev]);
            num_interact.push_back(num_interacta[pev]);
            }
      }
}
FILE *fp200;
if ((fp200=fopen("Data_Matrix2","rb+"))==NULL) {
      printf("Cannot open file.\n");
      exit(1);}
int s10, a10, Event_num_max2b;
double r10;
vector<double> theta_vb,x1_vb,y1_vb,z1_vb,xd_vb,yd_vb,zd_vb,Dtheta_vb,
num_interactb,FOMb,Energyb ;
Event_num_max2b=Event_num_max2+Event_num_max2*mag2;
for (s10=0;s10<Event_num_max2b; s10++) {
            fread(&r10, sizeof(double), 1, fp200);
            theta_vb.push_back(r10);
            fread(&r10, sizeof(double), 1, fp200);
            x1_vb.push_back(r10);
            fread(&r10, sizeof(double), 1, fp200);
            y1_vb.push_back(r10);
            fread(&r10, sizeof(double), 1, fp200);
            z1_vb.push_back(r10);
            fread(&r10, sizeof(double), 1, fp200);
            xd_vb.push_back(r10);
            fread(&r10, sizeof(double), 1, fp200);
            yd_vb.push_back(r10);
            fread(&r10, sizeof(double), 1, fp200);
            zd_vb.push_back(r10);
            fread(&r10, sizeof(double), 1, fp200);
            Energyb.push_back(r10); //
            fread(&r10, sizeof(double), 1, fp200);
            Dtheta_vb.push_back(r10);
            fread(&r10, sizeof(double), 1, fp200);
            FOMb.push_back(r10);
            fread(&r10, sizeof(double), 1, fp200);
            num_interactb.push_back(r10);
}
int pevb, countb;
countb=0;
for (pevb=0; pevb<Event_num_max2b; pevb++){//event index
    if (countb<Event_num_max2+1 ){
      if (Dtheta_vb[pevb]<cone_error_max & Dtheta_vb[pevb]<theta_vb[pevb] &
      theta_vb[pevb]<cone_ape_limit_sup & theta_vb[pevb]>cone_ape_limit_inf){
            countb=countb+1;
            theta_v.push_back(theta_vb[pevb]);
            x1_v.push_back(x1_vb[pevb]);
            y1_v.push_back(y1_vb[pevb]);
            z1_v.push_back(z1_vb[pevb]);
            xd_v.push_back(xd_vb[pevb]);
            yd_v.push_back(yd_vb[pevb]);
            zd_v.push_back(zd_vb[pevb]);
            Dtheta_v.push_back(Dtheta_vb[pevb]);
            Energy.push_back( Energyb[pevb]);
            FOM.push_back(FOMb[pevb]);
```

```
            num_interact.push_back(num_interactb[pevb]);
            }
      }
}
//////////////////////////////////////////////////////////////////////
//                 GEOMETRY AND COORDINATE SYSTEM
/////////////////////////////////////////////////////////////////////
//                         Voxel Size
double incrementx, incrementy, incrementz;
incrementx=FOV_x/gx;
incrementy=FOV_y/gy;
incrementz=FOV_z/gz;
//                 Redefine Number Of Divisions
int g, g_x, g_y, g_z; //FOV grid (number of voxels along each axis)
g_x=gx+1;
g_y=gy+1;
g_z=gz+1;
g=g_x*g_y*g_z;
//                       FOV Boundaries
double Xmax, Xmin, Ymax, Ymin, Zmax, Zmin; //voxel centroid
Xmax=XFOV_center+FOV_x/2;
Xmin=XFOV_center-FOV_x/2;
Ymax=YFOV_center+FOV_y/2;
Ymin=YFOV_center-FOV_y/2;
Zmax=ZFOV_center+FOV_z/2;
Zmin=ZFOV_center-FOV_z/2;
//        Equivalent Voxel Radius Used For 3D Integration
double v_radius;
v_radius=pow(((incrementx*incrementy*incrementz)*3.0/(4.0*pi)), 1.0/3.0);
//                     Coordinate  Vectors
vector<double> x_v1(G), y_v1(G), z_v1(G);
int m5;
for (m5=0; m5<g_x; m5++){
      x_v1[m5]=Xmin+(incrementx)*m5;}//progressive coordinate
for (m5=0; m5<g_y; m5++){
      y_v1[m5]=Ymin+(incrementy)*m5;}
for (m5=0; m5<g_z; m5++){
      z_v1[m5]=Zmin+(incrementz)*m5;}
//                    Coordinate System Vectors
vector<double> x_v(G), y_v(G), z_v(G);
int i5, j5, k5, ind;
ind=0;
for (i5=0; i5<g_z; i5++){
      for (j5=0; j5<g_x; j5++){
                  for (k5=0; k5<g_y; k5++){
                  y_v[ind]=y_v1[k5];
                  x_v[ind]=x_v1[j5];
                  z_v[ind]=z_v1[i5];
                  ind=ind+1;
                  }
      }
}
//////////////////////////////////////////////////////////////////////
//                           BACKPROJECTION
//////////////////////////////////////////////////////////////////////
time_t start,end;
double dif;
```

```
time (&start);
//*********************  Error Settings  ************************
double E_inf, E_sup, E_error, E_dep_meas, Em0, Em180, d_x, Dtheta_0,
Dtheta_180;
int yy;
E_inf=1.4; //keV   detector energy precision error at 60kev
E_sup=2.5;//keV    detector energy precision error at 1332kev
d_x=0.5;// mm      detector position precision error [mm]
//*************************************************************
//FILE *fp101;
//if ((fp101=fopen("angular_error.txt","wb+"))==NULL) {
//    printf("Cannot open file.\n");
//    exit(1);
//}
int p, k1, k2, k, event_number, i, j, dt, gg, tt, rr, ss;//hh
double x1, y1, z1, xd, yd, zd, x, y, z, Dtheta, theta, limit, W,
DistanceTheta_pixelTOEvent, Dtheta_e, Dtheta_g;
vector<double> index_k(G), B1(G), hh_l(Event_num_max);
double D_v_aper, L_v, Theta1, Theta2;
vector<double> KK;
vector<double> TT;
vector<double> B;
vector<double> event_index;
for (dt=0; dt<G; dt++){
B1[dt]=0;
index_k[dt]=0;}
for (ss=0; ss<Event_num_max; ss++){
hh_l[ss]=0;}
event_number=0;

for (p=0; p<Event_num_max; p++){//event index
      if (Dtheta_v[p]<cone_error_max & Dtheta_v[p]<theta_v[p] &
      theta_v[p]<cone_ape_limit_sup & theta_v[p]>cone_ape_limit_inf){
      event_index.push_back(p);// index of events that have been analized
          event_number=event_number+1;
         //Event Direction in event frame; position coordinates are
         continuous (not discretized)
         xd=xd_v[p]; //position of second gamma-ray interaction
         yd=yd_v[p];
         zd=zd_v[p];
         theta=theta_v[p]; //cone aperture
         // Dtheta=Dtheta_v[p];//cone aperture angular error read from input
         data file
         ////////     Compute Cone Angular Aperture Error      ////////
         E_dep_meas=(1-cos(theta))*E0*E0/(511.+E0*(1-cos(theta))); //[keV]
         energy deposition during gamma-ray first interaction from Compton
         Formula
         E_error=E_inf+(E_sup-E_inf)*(E_dep_meas-60)/(1332.-60.);//error on
         energy deposition
         Em0=E_dep_meas-E_error; //inferior energy deposition, used for
         electron moving away from photon
         Em180=E_dep_meas+E_error; //superior energy deposition, used for
         electron moving towards photon;
         Dtheta_0=0.; //initiate variable; error for electron moving away
         from photon
         Dtheta_180=0.; //initiate variable; error for electron moving toward
         photon
```

```
       for (yy=0; yy<size_B_en; yy++){//sum over all binding energy levels to
       calculate average error due to momentum of orbital electron and
       detector energy resolution from model describing scattering of a
       photon against a bound electron
       Dtheta_0=Dtheta_0+abs(acos((E0*E0-Em0*E0-Em0*511.+Em0*B_en[yy]-
       B_en[yy]*E0+511.*B_en[yy]+B_en[yy]*B_en[yy]+E0*sqrt(B_en[yy]*B_en[yy]+
       2*511.*B_en[yy]))/(E0*E0-E0*Em0-
       B_en[yy]*E0+sqrt(B_en[yy]*B_en[yy]+2*511.*B_en[yy])*(E0-B_en[yy]-
       Em0)))-theta);
       Dtheta_180=Dtheta_180+abs(acos((E0*E0-Em180*E0-
       Em180*511.+Em180*B_en[yy]-B_en[yy]*E0+511.*B_en[yy]+B_en[yy]*B_en[yy]-
       E0*sqrt(B_en[yy]*B_en[yy]+2*511.*B_en[yy]))/(E0*E0-E0*Em180-
       B_en[yy]*E0-sqrt(B_en[yy]*B_en[yy]+2*511.*B_en[yy])*(E0-B_en[yy]-
       Em180)))-theta);
       }
Dtheta_e=(Dtheta_0+Dtheta_180)/(2*size_B_en); // error due to energy
precision of detector and momentum of orbital electron
Dtheta_g=abs(atan(2*d_x/sqrt(xd*xd+yd*yd+zd*zd)));//error due to position
precision of detector
Dtheta=Dtheta_e+Dtheta_g;//total error
//fwrite(&E_dep_meas,sizeof(double),1,fp101);
//fwrite(&Dtheta_e,sizeof(double),1,fp101);
//fwrite(&Dtheta_g,sizeof(double),1,fp101);
//fwrite(&Dtheta,sizeof(double),1,fp101);
limit=limit_factor*Dtheta;// integration is carried on up to a certain
multiple of the error
            for (k=0; k<G; k++){ //computes angular distance between cone
            surface and each voxel in FOV
            //voxel coordinate relative to cone vertex
             x=x_v[k]-x1_v[p];//not a voxel centroid (not a problem)
             y=y_v[k]-y1_v[p];
             z=z_v[k]-z1_v[p];
             // if voxel distance from cone surface is larger than
             limit_factor * sigma/2, intensity of voxel is zero.
             DistanceTheta_pixelTOEvent=pi-
             acos((x*xd+y*yd+z*zd)/(sqrt(x*x+y*y+z*z)*sqrt(xd*xd+yd*yd+zd*zd)
             ))-theta;//radians (1rad=180deg=pi)
             L_v=sqrt(x*x+y*y+z*z);//spatial distance between voxel centroid
             and cone vertex
             D_v_aper=asin(v_radius/L_v);//always positive//approximately
             equal to angle between voxel centroid and voxel boundary when
             cubic voxel is modeled as equivalent spherical voxel
             Theta1=(abs(DistanceTheta_pixelTOEvent)-D_v_aper);//Inferior
             limit of integration
             Theta2=(abs(DistanceTheta_pixelTOEvent)+D_v_aper);   //superior
             limit of integration
//////////////////////////////////////////////////////////////////////Two
distinguished approaches can be used to evaluate the intensity of each voxel
due to each cone:1)One is based on a probability density function that
depends on angular distance of the voxel form the cone surface;  2) The other
is based on a probability density function that depends on linear distance of
the voxel form the cone surface. The first option carries with it the
physical description of the phenomena (the error associated to each cone is
an agular error affecting cone angular aperture); the second is an
approximation made to minimiza impulse res[onse dependence on position within
field of view.
Both approaches are listed below.
```

```
///////////////////////////////////////////////////////////////////////
/////// Option 1: Use of PDF that depends on angular distance /////////
      if ((abs(abs(DistanceTheta_pixelTOEvent)-D_v_aper))<limit){
         if((abs(DistanceTheta_pixelTOEvent)+D_v_aper)<limit){
         //W=(1/pi)*(atan((abs(DistanceTheta_pixelTOEvent)+D_v_aper)
         /Dtheta)-atan((abs(DistanceTheta_pixelTOEvent)-
         D_v_aper)/Dtheta));// Lorentz distribution value at voxel
         centroid
         //INTEGRATION of Lorentz function over voxel volume
         W=Dtheta*(L_v*L_v*(Theta1-
         Theta2)+(abs(DistanceTheta_pixelTOEvent))*log((Dtheta*Dthet
         a+Theta2*Theta2)/(Dtheta*Dtheta+Theta1*Theta1))*L_v*L_v)+(D
         theta*Dtheta*L_v*L_v-
         (DistanceTheta_pixelTOEvent)*(DistanceTheta_pixelTOEvent)*L
         _v*L_v+v_radius*v_radius)*(atan(Theta2/Dtheta)-
         atan(Theta1/Dtheta));
         }
         else{
         Theta2=limit;
         //W=(1/pi)*(atan((limit)/Dtheta)-
         atan((abs(DistanceTheta_pixelTOEvent)-D_v_aper)/Dtheta));//
         Lorentz distribution value at voxel centroid
         //INTEGRATION of Lorentz function over voxel volume
         W=Dtheta*(L_v*L_v*(Theta1-
         Theta2)+(abs(DistanceTheta_pixelTOEvent))*log((Dtheta*Dthet
         a+Theta2*Theta2)/(Dtheta*Dtheta+Theta1*Theta1))*L_v*L_v)+(D
         theta*Dtheta*L_v*L_v-
         (DistanceTheta_pixelTOEvent)*(DistanceTheta_pixelTOEvent)*L
         _v*L_v+v_radius*v_radius)*(atan(Theta2/Dtheta)-
         atan(Theta1/Dtheta));
         }
///////////////////////////// End Option 1 ////////////////////////////
/////////Option 2: Use of a PDF that depends on linear distance ///////
v_diag=40.0*tan(Dtheta);
D_linear=abs(L_v*sin(DistanceTheta_pixelTOEvent));//new
    if (D_linear<v_diag){
      W=v_diag/( D_linear*D_linear+v_diag*v_diag);
///////////////////////////// End Option 2 ////////////////////////////
   //K[p][hh]=k;//index of voxels intersected by event p
         //hh=hh+1;//index for number of voxels intersected by event
         p; total length is function of k
         hh_l[event_number-1]=hh_l[event_number-1]+1;//number of
         voxels intersected by event p;
         KK.push_back(k);//insert voxel index k into vector KK
         index_k[k]=index_k[k]+1;//number of events intersecting
         voxel k
         //gg=index_k[k];
         B.push_back(W);// voxel weight is stored for each event,
         starting with event 1
         B1[k]=W+B1[k];// weight for each voxel
       }
      }
   }
}
//fclose (fp101);
cout << "Event Analyzed ";
printf("%i ", event_number);
```

```
int size_B;
size_B=B.size();
cout << "Size B [Elements] ";
printf("%i ", size_B);
//**********************      Output Files    ***********************
FILE *fp2;//write backprojection results
if ((fp2=fopen("Backprojection.txt","wb+"))==NULL) {
      printf("Cannot open file.\n");
      exit(1);
}
int n;
for (n=0; n<G; n++){
      fwrite(&B1[n],sizeof(double),1,fp2);}
fclose (fp2);
/*
FILE *fp3;
if ((fp3=fopen("B_Vector.txt","wb+"))==NULL) {
      printf("Cannot open file.\n");
      exit(1);
}
int nnn;
for (nnn=0; nnn<size_B; nnn++){
         fwrite(&B[nnn],sizeof(double),1,fp3);}
fclose (fp3);
FILE *fp4;
if ((fp4=fopen("B_Index_Vector.txt","wb+"))==NULL) {
      printf("Cannot open file.\n");
      exit(1);
}
int nnnn;
for (nnnn=0; nnnn<size_B; nnnn++){
         fwrite(&KK[nnnn],sizeof(double),1,fp4);}
fclose (fp4);//*/
/*
FILE *fp9;
if ((fp9=fopen("hh_l_numofpixintersbyfictievent.txt","wb+"))==NULL) {
      printf("Cannot open file.\n");
      exit(1);
}
int nnnnn;
for (nnnnn=0; nnnnn<Event_num_max; nnnnn++){
         fwrite(&hh_l[nnnnn],sizeof(double),1,fp9);}
fclose (fp9);//*/
////////////////////////////////////////////////////////////////////////
//                 Finds Maximum of Backprojection
////////////////////////////////////////////////////////////////////////
int ds;
double Max_B, Max_ind, counter10;
Max_B=0.00;
counter10=0.0;
for (ds=0; ds<G; ds++){
        if (Max_B<B1[ds]){
            Max_B=B1[ds];//Value of maximum
            Max_ind=counter10;//progressive voxel index of maximum intensity
            of backprojection
         }
            counter10=counter10+1.0;
```

```
}
cout << "Max_value of Backprojection ";
printf("%f ", Max_B);
cout << "Progressive Voxel Index of Maximum of Backprojection ";
printf("%f ", Max_ind);
double z_max_index, y_max_index, x_max_index,go;
double reminder_z, x_max, y_max, z_max, container, container2;
go=(Max_ind)/(g_x*g_y);
z_max_index=floor(go);
reminder_z=Max_ind-z_max_index*(g_x*g_y);
if (reminder_z==0){
      x_max_index=0;
      y_max_index=0;}
else{
      container=reminder_z/g_y;
      x_max_index=floor(container);
      y_max_index=(reminder_z)-(g_y*x_max_index);}
      x_max=Xmin+x_max_index*incrementx;
      y_max=Ymin+y_max_index*incrementy;
      z_max=Zmin+z_max_index*incrementz;
cout << "x_max ";
printf("%f ", x_max);
cout << "y_max ";
printf("%f ", y_max);
cout << "z_max ";
printf("%f ", z_max);
cout << "x_max_index ";
printf("%f ", x_max_index);
cout << "y_max_index ";
printf("%f ", y_max_index);
cout << "z_max_index ";
printf("%f ", z_max_index);

///////////////////////////////////////////////////////////////
//                           ARM  PLOT
//////////////////////////////////////////////////////////////
/*    FILE *fp5;
if ((fp5=fopen("Events_not_intersecting_max.txt","wb+"))==NULL) {
      printf("Cannot open file.\n");
      exit(1);
}
FILE *fp6;
if ((fp6=fopen("Events_intersecting_max.txt","wb+"))==NULL) {
      printf("Cannot open file.\n");
      exit(1);
}
int ppp2, hhh2;// counter_events;
double  DistanceEvent_to_maximum2, x_maxd2,y_maxd2, z_maxd2 ;
vector<double> ARM2;
         for (ppp2=0; ppp2<event_number; ppp2++){//event index
         hhh2=event_index[ppp2]; //real index of event
         xd=-xd_v[hhh2]; //event direction
         yd=-yd_v[hhh2];// 180 degree rotation
         zd=-zd_v[hhh2];
         theta=theta_v[hhh2]; //radians, cone aperture
         Dtheta=Dtheta_v[hhh2];//angular uncertanty on cone aperture
         x_maxd2=x_max-x1_v[hhh2];
```

```
            y_maxd2=y_max-y1_v[hhh2];
         z_maxd2=z_max-z1_v[hhh2];
         DistanceEvent_to_maximum2=(acos((x_maxd2*xd+y_maxd2*yd+z_maxd2*zd)/(sqr
         t(x_maxd2*x_maxd2+y_maxd2*y_maxd2+z_maxd2*z_maxd2)*sqrt(xd*xd+yd*yd+zd*
         zd))))-theta_v[hhh2];
         ARM2.push_back(DistanceEvent_to_maximum2); //contains the angular
         distance of each event that has been analized form maximum value of
         backprojection
         //if((abs(DistanceEvent_to_maximum2))>(limit_factor*Dtheta)){//cones
         that do not contribute to maximum
                if ((abs(DistanceEvent_to_maximum2))>(ARM_Peak_Angle)){
                fwrite(&theta_v[hhh2],sizeof(double),1,fp5);
                fwrite(&x1_v[hhh2],sizeof(double),1,fp5);
                fwrite(&y1_v[hhh2],sizeof(double),1,fp5);
                fwrite(&z1_v[hhh2],sizeof(double),1,fp5);
                fwrite(&xd_v[hhh2],sizeof(double),1,fp5);
                fwrite(&yd_v[hhh2],sizeof(double),1,fp5);
                fwrite(&zd_v[hhh2],sizeof(double),1,fp5);
                fwrite(&Energy[hhh2],sizeof(double),1,fp5);
                fwrite(&Dtheta_v[hhh2],sizeof(double),1,fp5);
                fwrite(&FOM[hhh2],sizeof(double),1,fp5);
                fwrite(&num_interact[hhh2],sizeof(double),1,fp5);
                fwrite(&DistanceEvent_to_maximum2,sizeof(double),1,fp5);}
                else{//events that contribute to maximum
               fwrite(&theta_v[hhh2],sizeof(double),1,fp6);
                fwrite(&x1_v[hhh2],sizeof(double),1,fp6);
                fwrite(&y1_v[hhh2],sizeof(double),1,fp6);
                fwrite(&z1_v[hhh2],sizeof(double),1,fp6);
                fwrite(&xd_v[hhh2],sizeof(double),1,fp6);
                fwrite(&yd_v[hhh2],sizeof(double),1,fp6);
                fwrite(&zd_v[hhh2],sizeof(double),1,fp6);
                fwrite(&Energy[hhh2],sizeof(double),1,fp6);
                fwrite(&Dtheta_v[hhh2],sizeof(double),1,fp6);
                fwrite(&FOM[hhh2],sizeof(double),1,fp6);
                fwrite(&num_interact[hhh2],sizeof(double),1,fp6);
                fwrite(&DistanceEvent_to_maximum2,sizeof(double),1,fp6);}
}
FILE *fp7;
if ((fp7=fopen("ARM.txt","wb+"))==NULL) {
      printf("Cannot open file.\n");
      exit(1);
}
int m100;
      for (m100=0; m100<event_number; m100++){
         fwrite(&ARM2[m100],sizeof(double),1,fp7);}
fclose (fp5);
fclose (fp6);
fclose (fp7);//*/
///////////////////////////////////////////////////////////////////////
//                   MAXIMUM LIKELIHOOD ALGORITHM
///////////////////////////////////////////////////////////////////////////
FILE *fp8;
if ((fp8=fopen("ML_Intensity_over_Iterations.txt","wb+"))==NULL) {
      printf("Cannot open file.\n");
      exit(1);
}
/*
```

```
FILE *fp12;
if ((fp12=fopen("NormalizedDenominatorSum_vs_Iter.txt","wb+"))==NULL) {
      printf("Cannot open file.\n");
      exit(1);
}
FILE *fp13;
if ((fp13=fopen("Convergence_vs_Iter.txt","wb+"))==NULL) {
      printf("Cannot open file.\n");
      exit(1);
}
FILE *fp15;
if ((fp15=fopen("Absolute_Convergence_vs_Iter.txt","wb+"))==NULL) {
      printf("Cannot open file.\n");
      exit(1);
}
FILE *fp16;
if ((fp16=fopen("Zvector_vs_iterations.txt","wb+"))==NULL) {
      printf("Cannot open file.\n");
      exit(1);
}//*/
//****************  FIRST GUESS FOR ML INTENSITY *****************
//ML_iter_num=ones([1 g_x*g_y*g_z]); //first guess is uniform
int o, d, nm;
vector<double> ML_iter_num(G);
for (nm=0; nm<G; nm++){// first guess for ML Intensity
ML_iter_num[nm]=(B1[nm]/event_number);} //first guess is back-projection
vector<double> kkk(Event_num_max);
int ev;
kkk[0]=0;// index where each event starts in vector KK and B
      for (ev=1; ev<event_number; ev++){
             kkk[ev]=hh_l[ev-1]+kkk[ev-1];}
vector<double> Kj(Event_num_max);
int ev_num10, cc10, i_i10;
for (ev_num10=0; ev_num10<event_number; ev_num10++){///
         cc10=kkk[ev_num10];//index where each event starts in vector KK and
B
for (i_i10=0; i_i10<hh_l[ev_num10]; i_i10++){// scan only pixels intersected
by event ev_num   (done for each event)
         Kj[ev_num10]=B[cc10]+Kj[ev_num10];//sum of weights of all pixels
         intersecting event j
         cc10=cc10+1;}
}
********************************************************************
int iter_num, ev_num, i_i, v, e, t1, u1, q3, cc, l, f, ff, i_ii, jj, mmm;
vector<double> Den_iter_num(Event_num_max), Num_iter_num(Event_num_max);//
event index
vector<double> ML_factor(G), S(G), fraction(G),abs_convergence(G);
vector<double> Z_Sum_Pixel(Event_num_max);
for (iter_num=0; iter_num<Iterations; iter_num++){//iteration index
          for (mmm=0; mmm<event_number; mmm++){// at each iteration reset Den
          for each event
                  Den_iter_num[mmm]=0;
                  Z_Sum_Pixel[mmm]=0;
          }
          for (l=0; l<G; l++){ //at each iteration reset ML multiplier
                  ML_factor[l]=0;
                  S[l]=0;
```

```
          }
          for (ev_num=0; ev_num<event_number; ev_num++){
                  cc=kkk[ev_num];
                  for (i_i=0; i_i<hh_l[ev_num]; i_i++){// scan only voxels
                  intersected by event ev_num
                  f=KK[cc];//index of voxel intersected by event j_i
                  Den_iter_num[ev_num]=B[cc]*ML_iter_num[f]+Den_iter_num[ev_n
                  um];
                  cc=cc+1;}
                  Num_iter_num[ev_num]=1/Den_iter_num[ev_num];
            }
   for (jj=0; jj<event_number; jj++){
            cc=kkk[jj];// for each event it gives the index where to start in
            vector B and KK
            for (i_ii=0; i_ii<hh_l[jj]; i_ii++){ // hh_l is the number of
            voxels intersected by event j
            l=KK[cc];// real index of voxel intersected by event j
            ML_factor[l]=ML_factor[l]+B[cc]*Num_iter_num[jj];// B[cc] is the
            intensity of voxel l for event j
                      if (iter_num==Iter1 | iter_num==Iter2 | iter_num==Iter3
                      | iter_num==Iter4 | iter_num==Iter5 | iter_num==Iter6 |
                      iter_num==Iter7 | iter_num==Iter8 | iter_num==Iter9 |
                      iter_num==Iter10){
                      Z_Sum_Pixel[jj]=Z_Sum_Pixel[jj]+Num_iter_num[jj]*ML_ite
                      r_num[l]*B[cc];}
            S[l]=S[l]+B[cc];// intensity summed over event jj
            cc=cc+1;
            }
      /*   if (iter_num==Iter1 | iter_num==Iter2 | iter_num==Iter3 |
      iter_num==Iter4 | iter_num==Iter5 | iter_num==Iter6 | iter_num==Iter7 |
      iter_num==Iter8 | iter_num==Iter9 | iter_num==Iter10){
      fwrite(&Z_Sum_Pixel[jj],sizeof(double),1,fp16);}
    }
      for (t1=0; t1<G; t1++){
      //compute relative difference for convergence
      fraction[t1]=(ML_iter_num[t1]-
      ML_iter_num[t1]*ML_factor[t1])/((ML_iter_num[t1]+ML_iter_num[t1]*ML_fac
      tor[t1])/2);//use smallest value at denominator
      abs_convergence[t1]=(ML_iter_num[t1]-ML_iter_num[t1]*ML_factor[t1]);
      /*if (iter_num==Iter1 | iter_num==Iter2 | iter_num==Iter3 |
      iter_num==Iter4 | iter_num==Iter5 | iter_num==Iter6 | iter_num==Iter7 |
      iter_num==Iter8 | iter_num==Iter9 | iter_num==Iter10){
      fwrite(&fraction[t1],sizeof(double),1,fp13);
      fwrite(&abs_convergence[t1],sizeof(double),1,fp15);}
      //////      Update Intensity
      ML_iter_num[t1]=ML_iter_num[t1]*ML_factor[t1] ;
      if (iter_num==Iter1 | iter_num==Iter2 | iter_num==Iter3 |
      iter_num==Iter4 | iter_num==Iter5 | iter_num==Iter6 | iter_num==Iter7 |
      iter_num==Iter8 | iter_num==Iter9 | iter_num==Iter10){
      fwrite(&ML_iter_num[t1],sizeof(double),1,fp8);}
      }
}
time (&end);
dif = difftime (end,start);
printf ("It took you %.6lf seconds for Backprojection and ML iteration.\n",
dif );
FILE *fp10;
```

```
if ((fp10=fopen("ML_Intensity.txt","wb+"))==NULL) {
      printf("Cannot open file.\n");
      exit(1);
}
int m2;
      for (m2=0; m2<G; m2++){
         fwrite(&ML_iter_num[m2],sizeof(double),1,fp10);}
fclose (fp10);
fclose (fp8);
//*fclose (fp12);
//*fclose (fp13);
//*fclose (fp15);
//*fclose (fp16);
//////////////////////////////////////////////////////////////////////
//                         WRITE HEADER FILE
//////////////////////////////////////////////////////////////////////
FILE *fp11;
if ((fp11=fopen("Header.txt","wb+"))==NULL) {
      printf("Cannot open file.\n");
      exit(1);
}
double FOVx, FOVy, FOVz, XFOV_c, YFOV_c, ZFOV_c, gX, gY, gZ;
int Iter, limit_fac, scanned_Ev;
FOVx=FOV_x;
FOVy=FOV_y;
FOVz=FOV_z;
XFOV_c=XFOV_center;
YFOV_c=YFOV_center;
ZFOV_c=ZFOV_center;
gX=gx;
gY=gy;
gZ=gz;
Iter=Iterations;
limit_fac=limit_factor;
scanned_Ev=Event_num_max;
         fwrite(&FOVx,sizeof(double),1,fp11);
         fwrite(&FOVy,sizeof(double),1,fp11);
         fwrite(&FOVz,sizeof(double),1,fp11);
         fwrite(&XFOV_c,sizeof(double),1,fp11);
         fwrite(&YFOV_c,sizeof(double),1,fp11);
         fwrite(&ZFOV_c,sizeof(double),1,fp11);
         fwrite(&gX,sizeof(double),1,fp11);
         fwrite(&gY,sizeof(double),1,fp11);
         fwrite(&gZ,sizeof(double),1,fp11);
         fwrite(&Iter,sizeof(int),1,fp11);
         fwrite(&limit_fac,sizeof(int),1,fp11);
         fwrite(&event_number,sizeof(int),1,fp11);
         fwrite(&size_B,sizeof(int),1,fp11);
         fwrite(&dif,sizeof(double),1,fp11);
         fwrite(&scanned_Ev,sizeof(int),1,fp11);
         fwrite(&Iter1,sizeof(int),1,fp11);
         fwrite(&Iter2,sizeof(int),1,fp11);
         fwrite(&Iter3,sizeof(int),1,fp11);
         fwrite(&Iter4,sizeof(int),1,fp11);
         fwrite(&Iter5,sizeof(int),1,fp11);
         fwrite(&Iter6,sizeof(int),1,fp11);
         fwrite(&Iter7,sizeof(int),1,fp11);
```

```
         fwrite(&Iter8,sizeof(int),1,fp11);
         fwrite(&Iter9,sizeof(int),1,fp11);
         fwrite(&Iter10,sizeof(int),1,fp11);
         fclose (fp11);

fclose (fp100);// Data File
      //return 0;
}
////////////////////////////////////////////////////////////////////////////////
```